12-2015

On subgrid-scale physics in the convective atmospheric surface layer

Khuong Nguyen
Clemson University, knguyen@g.clemson.edu

On Subgrid-Scale Physics in the Convective Atmospheric Surface Layer

---

A Dissertation
Presented to
the Graduate School of
Clemson University

In Partial Fulfillment
of the Requirements for the Degree
Doctor of Philosophy
Mechanical Engineering

---

by
Khuong Xuan Nguyen
December 2015

Accepted by:
Dr. Chenning Tong, Committee Chair
Dr. Nigel B. Kaye
Dr. Richard S. Miller
Dr. Xiangchun Xuan

Abstract

The dynamics of the subgrid-scale (SGS) stress and scalar flux in the convective atmospheric surface layer are studied using field measurements from the Advection Horizontal Array Turbulence Study (AHATS). We extend the array technique previously used to evaluate the SGS velocity and temperature to include measurements of the fluctuating pressure, enabling separation of the resolvable- and subgrid-scale pressure and allowing for the first-ever observations of the pressure covariance terms and the full SGS budgets. Non-dimensional forms of the budget terms are analysed as functions of the surface-layer stability parameter, z/L, and the ratio of the wavelength of the spectral peak of the vertical velocity to the filter width, Λ_w/Δ_f, a measure of the large-eddy simulation (LES) fidelity. Analyses of the mean SGS turbulence kinetic energy budget show a balance among the production, transport, and dissipation. The mean SGS shear stress and SGS temperature flux budgets, meanwhile, are dominated by the production and pressure destruction, with the latter causing return to isotropy. The budgets of the normal components of the SGS stress are more complex. Most notably the pressure–rate-of-strain includes two competing processes, return to isotropy and generation of anisotropy, the latter due to ground blockage of the large-scale convective eddies. For neutral surface layers, return to isotropy dominates. For unstable surface layers return to isotropy dominates for small filter widths, whereas for large filter widths the ground blockage effect dominates, resulting in strong anisotropy.

Analyses of the terms in the budgets of the conditional mean SGS stress and SGS scalar flux, which must be correctly predicted by the SGS model in order for LES to reproduce the resolvable-scale velocity and temperature probability density functions, further reveal the complex dependence of the SGS pressure–rate-of-strain on the updrafts generated by buoyancy, downdrafts associated with the returning flow, and wall blocking effects. Under conditions of strong convective instability, the results most notably show conditional pressure redistribution from the (smaller) vertical to the

(larger) horizontal velocity components during downdrafts, resulting in generation of anisotropy. The conditional mean pressure transport, meanwhile, is a significant source of energy during updrafts as a result of the near-wall pressure minima. The vertical advection also plays an important role in the transfer of SGS energy. The results in the present study, particularly for the pressure–rate-of-strain, provide important insights into the near-wall SGS dynamics. We demonstrate with a scaling-based similarity model that it is possible to predict *a priori* both return-to-isotropy and generation-of-anisotropy behaviours observed for the normal (redistributive) components of the SGS pressure–rate-of-strain. The work has important implications for modelling the SGS stress using its transport equation in the convective atmospheric boundary layer.

Dedication

To my mom and dad.

Acknowledgments

My deepest thanks to Professor Chenning Tong, my thesis advisor, whose guidance and encouragement has allowed me to develop an understanding of the subject. I also thank my committee members, Professors Nigel Kaye, Richard Miller, and Xiangchun Xuan, for their constructive insights and critical review of the work.

I was fortunate to participate in the field campaign upon which this thesis is based, and am grateful to Professor John Wyngaard at Penn State University and to Drs. William Brown, Thomas Horst, Steven Oncley, and Peter Sullivan at the National Center for Atmospheric Research for their guidance in the field work. I also thank Dr. Martin Otte at the US Environmental Protection Agency for his help in the numerical approach.

This work was supported by the National Science Foundation through grants ATM–0638392 and ATM–1335995. Computational resources were provided by Clemson University through generous allotment of compute time on the Palmetto cluster.

Table of Contents

List of Tables

List of Figures

Chapter 1

Introduction

The daytime atmospheric boundary layer (ABL) plays a central role in the exchange of heat, momentum, and trace constituents between the earth's surface and the free atmosphere. Turbulence generated by geostrophic wind shear and large-scale thermals is the principle driver for these processes. Much of what we know of atmospheric turbulence stems from scaling arguments (Monin and Obukhov 1954; Willis and Deardorff 1974), field observations (Wyngaard and Coté 1971; Wyngaard et al. 1971; Kaimal et al. 1972; McBean and Elliott 1975; Kaimal et al. 1976) and, increasingly, numerical simulations (Nieuwstadt et al. 1991; Andrén et al. 1994; Beare et al. 2006). Indeed, what is now called large-eddy simulation (LES) has its origins in numerical weather prediction (Smagorinsky 1963; Lilly 1967; Deardorff 1970).

In LES, the large (or resolvable) scales of the turbulent flow field are explicitly computed while the effects of the smaller (subgrid) scales are modelled. The premise of LES is that if the energy-containing scales are well-resolved, then their statistics will be insensitive to the subgrid-scale (SGS) model, given that it extracts energy from the resolvable-scales at the correct rate (Lilly 1967; Nieuwstadt and de Valk 1987; Domaradzki et al. 1993; Mason 1994; Borue and Orszag 1998; Wyngaard 2004). This level of resolution requires the smallest resolvable scales to be in the inertial range. In LES of high-Reynolds-number turbulent boundary layers, such as the ABL, however, the smallest resolvable scales in the near-wall region are inevitably in the energy-containing range (Kaimal et al. 1972; Mason 1994; Peltier et al. 1996; Tong et al. 1998, 1999), leading to inherent under-resolution of the LES field. As a result, significant portions of the turbulent stress and scalar flux are carried by the subgrid scales, resulting in strong dependence of the near-wall LES results

on the SGS model (e.g. Mason and Thomson 1992; Tong et al. 1999). Consequently, deficiencies in the SGS model are likely to have an adverse impact on the near-wall LES statistics. For convective atmospheric boundary layers, errors in the surface layer can also propagate into the mixed layer and alter the flow structure there (e.g. Khanna and Brasseur 1998; Ludwig et al. 2009), likely due to the upward turbulent transport.

In conditions of under-resolved turbulence, first-order SGS models can fare poorly in their prediction of low-order flow statistics. The Smagorinsky-Lilly model (Smagorinsky 1963; Lilly 1967), for example, over-predicts the mean shear and streamwise velocity variance in the convective surface layer (Nieuwstadt and de Valk 1987; Mason 1994; Sullivan et al. 1994; Khanna and Brasseur 1997). The standard dynamic Smagorinsky model (Germano et al. 1991), which generally performs better than its constant eddy-viscosity counterpart, on the other hand under-predicts the mean shear (Porté-Agel et al. 2000a). These deficiencies have been attributed to the overly-dissipative nature of the Smagorinsky model and the underly-dissipative nature of the dynamic model (Sullivan et al. 1994; Mason 1994). Numerous SGS closures for the ABL have been constructed to overcome the shortcomings of the Smagorinsky model; we briefly mention a few such attempts. Mason and Thomson (1992) incorporate a stochastic forcing term in the LES equations to represent energy backscatter, a feature absent in the Smagorinsky model, which leads to improvements in the predicted mean velocity and streamwise velocity variance profiles. Similar improvements were achieved by Sullivan et al. (1994) using a modified version of Schumann's split model (Schumann 1975), which explicitly includes a mean-flow contribution and a reduction of the contributions from the near-wall turbulent fluctuations. Kosović (1997) proposed a nonlinear SGS model based on the nonlinear constitutive relationship suggested by Speziale (1991), consisting of both strain-rate and rotation tensors, which leads to improved predictions of the mean velocity profile. Porté-Agel et al. (2000a) argue that the coefficients in the dynamic Smagorinsky model are not equal at the LES and test filters, and use a second test filter to account for this scale dependence; their results for the mean velocity profile, second-order moments, and velocity spectra show improvements over the standard Smagorinsky model.

The improvements achieved by these models demonstrate the importance of incorporating surface-layer SGS physics, including history and non-local effects, into the SGS closure. The transport-equation-based SGS modelling approach (Deardorff 1972, 1973; Wyngaard 2004), which involves solving the full conservation equations for the SGS stress, is well-suited for this purpose

and has the potential to predict LES statistics with more accuracy (Hatlee and Wyngaard 2007; Ramachandran 2010; Ramachandran and Wyngaard 2011). Within this approach, parameterizations for the SGS production, turbulent and pressure transport, pressure–strain-rate interaction, and viscous dissipation are largely based on Reynolds-stress second-moment closure models (e.g. Lumley 1983). Along with production and dissipation, the SGS pressure–strain-rate correlation, responsible for the redistribution of SGS energy, is expected to be an important term in the SGS balance and therefore its modelling is crucial (Pope 2000). Wyngaard (2004) in fact shows that the eddy-diffusivity closure is merely an approximation of the SGS transport equations, derived by retaining only the isotropic production and pressure–rate-of-strain. Despite its importance, however, little is known of the latter aside from inference (Wyngaard 2010).

In the daytime ABL, the SGS dynamics are dependent on both the stability of the surface layer and the filter scale, and can have characteristics significantly different from those of a neutrally stratified flow. To develop improved SGS parameterizations, we seek to elucidate the physics of all the terms which evolve the SGS stress and SGS scalar flux transport equations. The chapters which follow comprise of separate manuscripts on this effort. In chapter 2, the dynamics of the SGS stress and scalar flux in the convective ABL are studied through the transport equations of the mean SGS turbulence kinetic energy, mean SGS stress, and mean SGS potential temperature flux. We use field measurements from the Advection Horizontal Array Turbulence Study (AHATS), which notably includes measurements of the fluctuating SGS pressure, allowing for the first-time-ever observations of the SGS pressure–rate-of-strain and pressure transport. In chapter 3, we derive the transport equations for the conditional mean SGS stress and SGS temperature flux and show that, for transport-equation-based SGS models, the budget terms must be correctly predicted by the SGS model in order for LES to reproduce the resolvable-scale velocity and temperature probability density functions. Field measurements from the AHATS campaign are then used to analyse the budget terms. Based on these analyses, in chapter 4 we construct a generalised model for the normal (redistributive) components of the SGS pressure–rate-of-strain which accounts for both shear and buoyancy effects. The model is tested *a priori* using high-resolution LES data. Concluding remarks are given in chapter 5.

Chapter 2

Measurements of the budgets of the subgrid-scale stress and temperature flux in a convective atmospheric surface layer

2.1 Introduction

Most SGS parameterizations involve direct modelling of the SGS stress using the resolvable-scale strain-rate tensor or the resolvable-scale velocity-gradient tensor. These first-order closures include the Smagorinsky model (Smagorinsky 1963; Lilly 1967; Deardorff 1970) and its variants (e.g. Schumann 1975; Deardorff 1980; Métais and Lesieur 1992), similarity models (Bardina et al. 1980), nonlinear models (Leonard 1974; Clark et al. 1979; Vreman et al. 1994), and the dynamic model (Germano et al. 1991) and its variants (Meneveau et al. 1996; Porté-Agel et al. 2000b). The advantages of these models are their relative functional simplicity and low computational cost compared to more complex closures (e.g. transport-equation-based models). The physics that can be incorporated into first-order models, however, is very limited (Wyngaard 2004; Hatlee and Wyngaard 2007).

At the next level, transport equations can be used to model the SGS stress and flux. In this class of models, the transport equations for the full SGS stress tensor are solved, allowing for more physics (including history and non-local effects) to be incorporated into the model (Deardorff 1972, 1973; Wyngaard 2004; Hatlee and Wyngaard 2007). Previous transport equation models are

largely based on Reynolds stress models. A review of the models for the terms in the Reynolds stress transport equation is given by Lumley (1983). Here, the production term is in closed form and dissipation is assumed to be isotropic. Turbulent transport is modelled using gradient diffusion or a transport equation, particularly for unstable surface layers. The pressure term is decomposed into a transport term and a pressure–strain-rate correlation. The former is often modelled along with turbulent transport. The latter is further decomposed into a "slow" and a "rapid" part. The slow part is modelled as a return-to-isotropy term (Rotta 1951), similar to that for neutral atmospheric boundary layers and other flows without buoyancy effects. A number of models exist for the rapid term (e.g. Launder et al. 1975; Shih and Lumley 1985; Fu et al. 1987). An important aspect of these models is that they take into account the effects of the transport properties of the surface layer turbulence on the Reynolds stress.

While the dynamics of the Reynolds stress and scalar flux depend on the stability condition of the atmospheric boundary layer (ABL), the dynamics of the SGS stress and flux also depend on the filter scale, and can have characteristics significantly different from those of the Reynolds stress and flux. Developing transport-equation-based SGS models, therefore, requires knowledge of the dynamics of the SGS stress and scalar flux. In the present study we investigate the SGS dynamics in near-neutral and unstable atmospheric surface layers. The budgets of the SGS turbulence kinetic energy (TKE), the SGS stress, and the SGS temperature flux are obtained from field measurements and examined to gain insights into the SGS dynamics.

The transport equation for the SGS stress deduced from the Navier-Stokes equations is (e.g. Lilly 1967)

$$\frac{\partial \tau_{ij}}{\partial t} + u_k^r \frac{\partial \tau_{ij}}{\partial x_k} = \frac{\partial}{\partial x_k} T_{ijk}^{(t)} + P_{ij} + P_{Bij} + \Pi_{ij} - \epsilon_{sij} - \nu \frac{\partial \tau_{ij}}{\partial x_k \partial x_k}, \tag{2.1}$$

where $\tau_{ij} = (u_i u_j)^r - u_i^r u_j^r$ is the (kinematic) SGS stress. A superscript r denotes a resolvable-scale variable. The terms on the left-hand side of equation (2.1) represent the time rate of change and advection of τ_{ij}, respectively. The terms on the right-hand side are the turbulent transport of τ_{ij}

$$\frac{\partial}{\partial x_k} T_{ijk}^{(t)} = \frac{\partial}{\partial x_k} \left[u_k^r \left(u_i u_j \right)^r - \left(u_i u_j u_k \right)^r + \left(\tau_{ik} u_j^r + \tau_{jk} u_i^r \right) \right], \tag{2.2}$$

the rate of mechanical production

$$P_{ij} = -\left(\tau_{ik}\frac{\partial u_j^r}{\partial x_k} + \tau_{jk}\frac{\partial u_i^r}{\partial x_k}\right), \tag{2.3}$$

the rate of buoyant production

$$P_{Bij} = \frac{g}{\Theta}\{\delta_{i3}\left[(\theta u_j)^r - \theta^r u_j^r\right] + \delta_{j3}\left[(\theta u_i)^r - \theta^r u_i^r\right]\}, \tag{2.4}$$

the velocity–pressure-gradient correlation

$$\Pi_{ij} = -\left[\left(u_i\frac{\partial p}{\partial x_j} + u_j\frac{\partial p}{\partial x_i}\right)^r - \left(u_i^r\frac{\partial p^r}{\partial x_j} + u_j^r\frac{\partial p^r}{\partial x_i}\right)\right], \tag{2.5}$$

the rate of viscous dissipation

$$\epsilon_{sij} = 2\nu\left[\left(\frac{\partial u_i}{\partial x_k}\frac{\partial u_j}{\partial x_k}\right)^r - \frac{\partial u_i^r}{\partial x_k}\frac{\partial u_j^r}{\partial x_k}\right], \tag{2.6}$$

and the rate of viscous transport, respectively. Here, u_i, p, Θ, θ, g, and ν are the velocity, kinematic pressure, mean and fluctuating potential temperatures, gravitational acceleration, and kinematic viscosity, respectively. The SGS velocity–pressure-gradient correlation can be decomposed into a pressure–strain-rate correlation and a pressure transport term,

$$\Pi_{ij} = \mathcal{R}_{ij} - \frac{\partial}{\partial x_k}T_{ijk}^{(p)}, \tag{2.7}$$

respectively, where

$$\mathcal{R}_{ij} = \left(p\frac{\partial u_i}{\partial x_j} + p\frac{\partial u_j}{\partial x_i}\right)^r - \left(p^r\frac{\partial u_i^r}{\partial x_j} + p^r\frac{\partial u_j^r}{\partial x_i}\right) \tag{2.8}$$

is the SGS pressure–strain-rate correlation tensor, and

$$T_{ijk}^{(p)} = \delta_{jk}\left[(pu_i)^r - p^r u_i^r\right] + \delta_{ik}\left[(pu_j)^r - p^r u_j^r\right]. \tag{2.9}$$

Contracting equation (2.1) yields the transport equation for the SGS TKE,

$$\frac{\partial k}{\partial t} + u_k^r\frac{\partial k}{\partial x_k} = \frac{1}{2}\frac{\partial}{\partial x_k}T_{iik}^{(t)} + \mathcal{P} + \mathcal{P}_B + \frac{1}{2}\frac{\partial}{\partial x_k}T_{iik}^{(p)} - \epsilon_{ks} - \nu\frac{\partial k}{\partial x_k\partial x_k}, \tag{2.10}$$

where $k = \left[(u_i u_i)^r - u_i^r u_i^r \right] / 2$ is the SGS turbulence kinetic energy. The terms on the left-hand side of equation (2.10) are the time rate of change and advection of k, respectively. The terms on the right-hand side are the turbulent transport of k

$$\frac{1}{2}\frac{\partial}{\partial x_k} T_{iik}^{(t)} = \frac{1}{2}\frac{\partial}{\partial x_k} \left[u_k^r (u_i u_i)^r - (u_i u_i u_k)^r + 2u_i^r (u_i u_k)^r - 2u_i^r u_i^r u_k^r \right], \tag{2.11}$$

the rate of mechanical production

$$\mathcal{P} = -\frac{1}{2}\tau_{ij} \left(\frac{\partial u_i^r}{\partial x_j} + \frac{\partial u_j^r}{\partial x_i} \right), \tag{2.12}$$

the rate of buoyant production

$$\mathcal{P}_B = \frac{g}{\Theta} \left[(\theta u_3)^r - \theta^r u_3^r \right], \tag{2.13}$$

the rate of pressure transport

$$\frac{1}{2}\frac{\partial}{\partial x_k} T_{iik}^{(p)} = -\frac{1}{2}\frac{\partial}{\partial x_k} \left[(2pu_k)^r - 2p^r u_k^r \right], \tag{2.14}$$

the rate of viscous dissipation

$$\epsilon_{ks} = \nu \left[\left(\frac{\partial u_i}{\partial x_k} \frac{\partial u_i}{\partial x_k} \right)^r - \frac{\partial u_i^r}{\partial x_k} \frac{\partial u_i^r}{\partial x_k} \right], \tag{2.15}$$

and the rate of viscous transport, respectively. Because the filter scale is much larger than the Kolmogorov scale in the surface layer (typically less than 1 mm), the viscous dissipation rate is almost entirely in the subgrid scales. Also note that the pressure–strain-rate correlation acts to redistribute energy among the three normal SGS stress components, and therefore sums to zero in equation (2.10).

The transport equation for the SGS temperature flux is

$$\frac{\partial F_i}{\partial t} + u_k^r \frac{\partial F_i}{\partial x_k} = \frac{\partial}{\partial x_k} T_{Fik}^{(t)} + P_{Fi} + P_{BFi} + \Pi_{Fi}, \tag{2.16}$$

where $F_i = (\theta u_i)^r - \theta^r u_i^r$ is the SGS temperature flux in the ith direction. The terms on the left-hand side of equation (2.16) are the time rate of change and advection of F_i, respectively. The terms

on the right-hand side are, in order, the turbulent transport of F_i

$$\frac{\partial}{\partial x_k} T_{Fik}^{(t)} = -\frac{\partial}{\partial x_k} \left[(\theta u_i u_k)^r - \theta^r \left(u_i u_k \right)^r - u_i^r \left(\theta u_k \right)^r - u_k^r \left(\theta u_i \right)^r + 2\theta^r u_i^r u_k^r \right], \tag{2.17}$$

the rate of gradient (stratification) production and tilting production

$$P_{Fi} = -\tau_{ik} \frac{\partial \theta^r}{\partial x_k} - F_k \frac{\partial u_i^r}{\partial x_k}, \tag{2.18}$$

respectively, the rate of buoyant production

$$P_{BFi} = \delta_{i3} \frac{g}{\Theta} \left[\left(\theta^2 \right)^r - \left(\theta^r \right)^2 \right], \tag{2.19}$$

and the temperature–pressure-gradient correlation

$$\Pi_{Fi} = -\left[\left(\theta \frac{\partial p}{\partial x_i} \right)^r - \theta^r \frac{\partial p^r}{\partial x_i} \right]. \tag{2.20}$$

The SGS temperature–pressure-gradient correlation can be decomposed into a correlation between the fluctuating pressure and temperature-gradient and a transport term representing heat flux divergences due to the fluctuating pressure,

$$\Pi_{Fi} = \mathcal{R}_{Fi} - \frac{\partial}{\partial x_k} T_{Fik}^{(p)}, \tag{2.21}$$

respectively, where

$$\mathcal{R}_{Fi} = \left(p \frac{\partial \theta}{\partial x_i} \right)^r - p^r \frac{\partial \theta^r}{\partial x_i} \tag{2.22}$$

and

$$T_{Fik}^{(p)} = \delta_{ik} \left[(p\theta)^r - p^r \theta^r \right]. \tag{2.23}$$

The terms in the SGS transport equations contain important SGS mechanisms, thereby allowing for more physics to be incorporated into the models. Such SGS models have the potential to provide improved performance under a wide variety of flows and conditions, especially when first-order models might fail, in a way similar to the Reynolds stress models (Lumley 1983).

Our previous studies have shown that the dynamics of the SGS stress and temperature

flux have a strong influence on the joint probability density function (j.p.d.f.) of the resolvable-scale velocity and temperature (Chen and Tong 2006; Chen et al. 2010). Analyses of the SGS stress, the SGS stress production rate, the SGS temperature flux, and the SGS temperature flux production rate conditional on the resolvable-scale velocity and temperature show that their statistics are closely related to the dynamics of the surface layer, particularly the strong buoyancy and vertical shear associated with updrafts and the conditional energy backscatter and isotropy of the SGS stress associated with downdrafts. Hence, buoyancy, shear, and the ground blockage effect play an important role in the physics of the SGS stress and flux, suggesting that an ideal SGS model should incorporate surface-layer effects in order to correctly predict LES statistics. In the present study, we investigate the budgets of the SGS stress and scalar flux by examining the dependence of the unclosed SGS terms on the stability parameter and the filter width.

2.2 Field campaign

The field measurements for this study, named the Advection Horizontal Array Turbulence Study (AHATS), were conducted in the San Joaquin Valley, California, during the summer of 2008 as a collaboration between Clemson University, Penn State University, and the National Center for Atmospheric Research (NCAR). The field site is identical to that of the previous HATS field study (described by Horst et al. 2004) and is located 5.6 km east-northeast of Kettleman City, California, within an area of flat, fallow farmland. Sky conditions were predominantly clear, generally with persistent, predictable wind directions from the north to northwest. The field surface consisted of crop stubble and weeds, for which the displacement height and surface roughness (determined using near-neutral wind profiles from HATS) were approximately 32 cm and 2 cm, respectively. Homogeneous surface roughness continues at least 2 km in the upwind (northwest) direction and 1 km downwind. Field measurements for AHATS were obtained using the Integrated Surface Flux System (ISFS) and Integrated Sounding System (ISS), both deployed by NCAR, from 25 June to 16 August 2008. The ISFS consists of multiple sensors, deployed in an array, for detailed examination of the turbulence structure of the atmospheric surface layer through measurements of near-surface wind, temperature, and pressure (discussed in detail below). The ISS was used to examine the heights beyond the surface layer using a wind profiler radar, sodar, and radiosondes.

The field measurement design is based on the transverse array technique, proposed, studied,

Array Spacing	Start PDT	End PDT	d_y (m)	d_x (m)	z_p (m)	z_s (m)	z_u (m)
Wide 1	1200 25 June	1200 01 July	4.00	16.00	3.24	4.24	3.74
Wide 2	1300 01 July	0600 18 July	4.00	16.00	3.24	4.24	3.24
Medium 1	1600 20 July	0600 29 July	1.29	5.12	3.64	4.64	3.64
Medium 2	1230 29 July	0600 08 Aug	1.29	5.12	4.83	5.83	4.83
Narrow	1800 09 Aug	0900 16 Aug	0.43	3.12	6.98	7.98	6.98

Table 2.1: AHATS array configurations. The streamwise array separation distance, d_x, was chosen to minimize flow distortion at the downwind array. However, as a precaution, the upwind arrays of the Medium 2 and Narrow configurations were also staggered by +17.23 and +5.74 m in the y direction, respectively. Supplementary photographs of the arrays are available at journals.cambridge.org/flm.

and first implemented successfully by Tong et al. (1997, 1998, 1999) for surface-layer measurements in the atmospheric boundary layer. In the context of LES, the technique uses horizontal sensor arrays to perform two-dimensional filtering to obtain resolvable- and subgrid-scale variables. It has subsequently been implemented in the ABL over land and ocean (Porté-Agel et al. 2001; Kleissl et al. 2003; Horst et al. 2004; Sullivan et al. 2006), within vegetation (Patton et al. 2011), over a glacier (Bou-Zeid et al. 2010), and in engineering flows (Cerutti et al. 2000; Tong 2001; Wang and Tong 2002; Rajagopalan and Tong 2003; Chen et al. 2003; Wang et al. 2004). Similar to these field studies, AHATS uses two vertically-spaced arrays of sensors, shown in figure 2.1(b), to obtain filtered variables and their derivatives. The primary (lower) array consists of 13 equally spaced three-component sonic anemometer-thermometers (Campbell Scientific CSAT3), while the secondary (upper) array has nine. The arrays are centered in the lateral direction and aligned perpendicular to the prevailing wind direction.

In AHATS, a third line of nine sonic anemometers was added upwind to measure spatial differences in the streamwise direction (see figure 2.1a and table 2.1; the data are not used in the present study but will be examined in future analyses of the budgets of the conditional SGS stress). In addition, two lines of turbulent pressure probes were added to measure, for the first time, the resolvable- and subgrid-scale pressure. The primary pressure array contains nine probes and is embedded at the center of the lower (downwind) sonic anemometer array; the secondary pressure array contains five pressure probes embedded within the upper sonic anemometer array. The pressure probes are mounted level with the sonic anemometers, and are offset by approximately +29 cm and +15 cm in the x and y directions (as defined in figure 2.1c), respectively, relative to the sonic anemometers to avoid interference with velocity measurements (e.g. flow-induced distortion

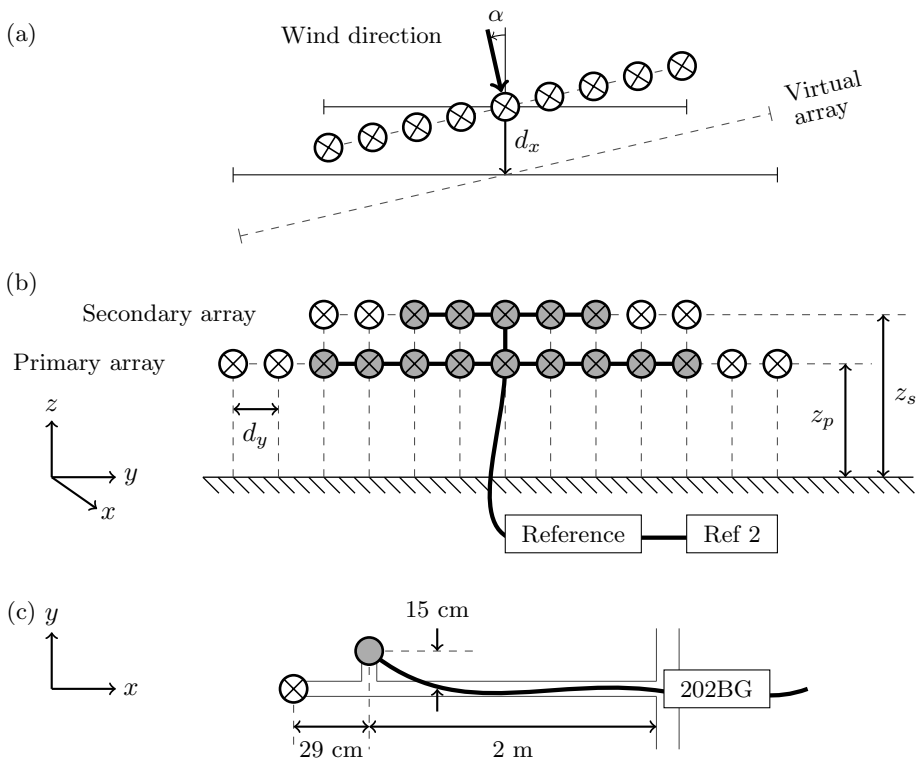

Figure 2.1: (a) Top view of arrays. The upwind and downwind arrays are centered laterally; z_u is the height of the upwind array, and d_x the streamwise separation distance. Dashed lines denote virtual arrays aligned perpendicular to the mean wind direction. (b) Front view of downwind array. Sonic anemometers ⊗ in the primary and secondary arrays are located at heights z_p and z_s, respectively; the horizontal spacing is d_y. Pressure ports ● are embedded at the center of the sonic arrays. (c) Top view of an individual mast. The reference side of the pressure transducers are connected to a common reference reservoir through thin tubing —. An additional transducer measures the reference pressure using a second reference reservoir. Supplementary photographs of the arrays are available at journals.cambridge.org/flm.

(Wyngaard 1981; Miller et al. 1999)). While it may be possible for the probes to be in the wakes of the anemometers when there is strong cross-wind, the pressure fluctuations due to the wake would be at frequencies much higher than the frequency range of the transducers, thus having negligible effect on the pressure measurements.

The pressure probes are modified commercial versions of the quad-disc design by Nishiyama and Bedard (1991), which are insensitive to velocity fluctuations and are capable of measuring pressure covariances with reasonable accuracy (Wyngaard et al. 1994). Each probe is connected through approximately 2 m of 1/4 inch (inner diameter) flexible tubing to a differential pressure transducer (Paroscientific Model 202BG). Attenuation of pressure fluctuations in the tubing is expected to be

negligible (Lenschow and Raupach 1991). The 202BG is a bidirectional (dual-bellows) gauge pressure transducer with high resolution and accuracy, well-suited for turbulent pressure measurements in the surface layer. Movement of the bellows is on the order of 10^{-5} mm so that the induced pressure on the reference side of the transducer is negligible. The reference side of the transducers is connected to a common reference reservoir through thin 1/16 inch flexible tubing. Following Wilczak and Bedard (2004), the reference reservoir is filled with loosely packed steel wool and buried (approximately 0.3 m deep) to prevent generation of dynamic pressure from convection and to maintain a uniform temperature (and hence pressure) through conduction. However, due to persistent low-frequency pressure fluctuations within the reference system induced by radiative heating and advective cooling of the reference tubing, an additional transducer was added to measure the reference pressure using a second reference reservoir buried at the same depth as the first. The absolute pressure is obtained by adding the reference pressure back to the measured (probe) pressure. This pressure signal still contains some residual low-frequency fluctuations (less than 0.05 Hz). Because the lengths of the reference tubes (10 to 15 m) do not support acoustic waves of such low frequencies, these fluctuations have the same phase and affect the signals of all of the pressure transducers the same way. The fluctuations were found to affect the pressure terms in the Reynolds stress budget as well as those in the SGS stress budgets for very large filter widths ($\Lambda_w/\Delta_f < 1$). Thus, we only obtain the SGS pressure terms for $\Lambda_w/\Delta_f > 1$.

The sonic anemometer data are sampled at 60 Hz, and were rotated to correct for sonic anemometer tilt using the planar fit technique (Wilczak et al. 2001). The pressure data are sampled at 10 Hz and then up-sampled to 60 Hz using spectral interpolation (Oppenheim and Schafer 1989) to match the sampling rate of the sonic anemometers. Upsampling of the pressure signal avoids downsampling of the velocity and temperature signals and potential underestimation of the related statistics. It does not affect the pressure-related SGS statistics; a comparison of the results obtained using the two sampling rates shows negligible differences. Following Horst et al. (2004), we rotate the coordinate system and interpolate the velocity, temperature, and pressure in the Cartesian coordinate system defined by the mean along-wind and cross-wind directions to obtain the virtual arrays (figure 2.1*a*). The interpolation is performed in spectral space to avoid attenuating the high-frequency (wavenumber) fluctuations. The coordinate rotation results in a decrease in the cross-wind spacing of the sensors, and therefore the effective filter width, by a factor of $\cos\alpha$, where α is the mean wind direction relative to the array normal. Following Wilczak and Bedard (2004), we also

time-lag the pressure data using Taylor's hypothesis to account for the 29 cm separation between the pressure probe and sonic anemometer in the along-wind direction. This reduces the loss of scalar flux covariance (Kristensen et al. 1997). No correction was applied for the cross-wind separation.

In the present study, we use the arrays to approximate top-hat filters. In the streamwise direction, assumption of Taylor's hypothesis (Lumley 1965) allows using the time-filtered signal as a surrogate for streamwise spatial filtering. Filtering in the transverse direction is performed by weight-averaging the output of the sensor array (Tong et al. 1998). For example, the transversely filtered resolvable-scale velocity (denoted by a superscript t) is obtained as

$$u_i^t(\mathbf{x}, t) = \sum_{j=-N}^{N} C_j u_i(x_1, x_2 + j \times d, x_3, t), \tag{2.24}$$

where $2N + 1$, C_j, and d are the number of sensors on the array, the weighting coefficient for the jth sensor, and the spacing between adjacent sensors, respectively. Owing to the limited number of sensors in the horizontal arrays, the weighting coefficients are chosen such that the response function of the low-resolution spanwise filter best matches that of the high-resolution streamwise filter (Horst et al. 2004). Streamwise and spanwise derivatives are approximated using fourth-order central finite-difference schemes, with a uniform spacing of $12\delta x = 12\delta y = 12 d_y \cos\alpha$. Vertical derivatives are approximated using a first-order one-sided finite difference, with a spacing of $\delta z = z_s - z_p$.

Several previous works have investigated the array filtering technique, including the accuracy of two-dimensional filtering and use of Taylor's hypothesis. Using a spectral cutoff array filter, Tong et al. (1998) showed that the r.m.s. values of the filtered variables differed from that of a true spectral cutoff filter by less than 10%. The accuracy of the top-hat array filter is expected to be higher (Chen and Tong 2006). They also showed two-dimensional filtering to be a good approximation of three-dimensional filtering with a 10% to 14% higher variance. Field measurements by Higgins et al. (2007) confirmed this result and showed that the difference can be interpreted as a 16% reduction in the filter size. Tong et al. (1998) showed that among the mechanisms that could affect the accuracy of Taylor's hypothesis, including the effects of different convecting velocities for different wavenumber components, temporal changes in the reference moving with the mean velocity, and the fluctuating convecting velocity, only the last was significant. Higgins et al. (2012) showed that Taylor's hypothesis is more applicable to large-scale motions than small-scale motions in the surface layer. The errors associated with approximating gradients by finite differences were studied by Kleissl

et al. (2003). They evaluated the divergence-free condition for the filtered velocity field using fourth- and first-order finite difference schemes for the horizontal and vertical derivatives, respectively, and concluded that the errors were acceptable for studying the SGS dynamics. Horst et al. (2004) further examined various issues of using the array technique, including the aliasing errors associated with evaluating derivatives using finite differences, and furthermore demonstrated reasonable accuracy of the technique.

Five different array configurations, shown in table 2.1, are employed in AHATS in order to vary the filter (grid) aspect ratio, z/Δ_f, and the stability parameter, z/L, where z, Δ_f, and $L = -u_*^3\Theta/\left(\kappa g\langle u_3'\theta'\rangle\right)$ are the height above the ground, the filter width, and the Monin-Obukhov length, respectively, with primes denoting fluctuations and angle brackets denoting ensemble averaging. We refer to z as the height of the primary array z_p here and hereinafter. Note, $\kappa = 0.41$, $u_* = (-\langle u_1'u_3'\rangle)^{1/2}$ (with u_1' in the mean wind direction), and $\langle u_3'\theta'\rangle = Q_0$ are the von Kármán constant (Pope 2000), the friction velocity, and the vertical temperature flux, respectively. We also define the surface-layer temperature scale as $T_* = -Q_0/u_*$. In the present work, we study the unstable surface layer (i.e. for which $z/L < 0$) using data from the medium and wide array configurations. We use 26 data segments, with each segment generally $30 - 90$ min in length (most over 60 min), collected during the daytime and spanning a wide range of $-z/L$ (figure 2.2). Each data segment has a steady mean velocity and approximately stationary fluctuating velocities. The temperature data were detrended to remove any linear trend. The lengths for most datasets correspond to approximately 2000 advection time scales of the vertical-velocity energy-containing eddies. The Reynolds-averaged statistics involve both time and spatial (across the array) averaging while the SGS statistics involve only time averaging. Although the precise level of statistical uncertainty is difficult to determine for some of the statistics obtained, it is sufficiently low for determining the dependence of the statistics on the important parameters (§3). Figure 2.3 gives the measured normal Reynolds stress components, friction velocity, and vertical temperature flux for the 26 datasets used in the analyses. The resolved fields are obtained using four different filter widths. In the y direction, top-hat filters of width $\Delta_y = 2d_y$, $4d_y$, $6d_y$, and $8d_y$ are created from a weighted sum of three-, five-, seven-, and nine-point cross-wind measurements, respectively. In the x direction, we use the mean wind velocity and sample rate to determine the streamwise filter width Δ_x (i.e. the number of data points in the averaging window) such that $\Delta_x = \Delta_y$. Shown in table 2.2, the filter aspect ratio z/Δ_f ranges from 0.10 to 1.87, allowing for the effects of grid anisotropy to be examined.

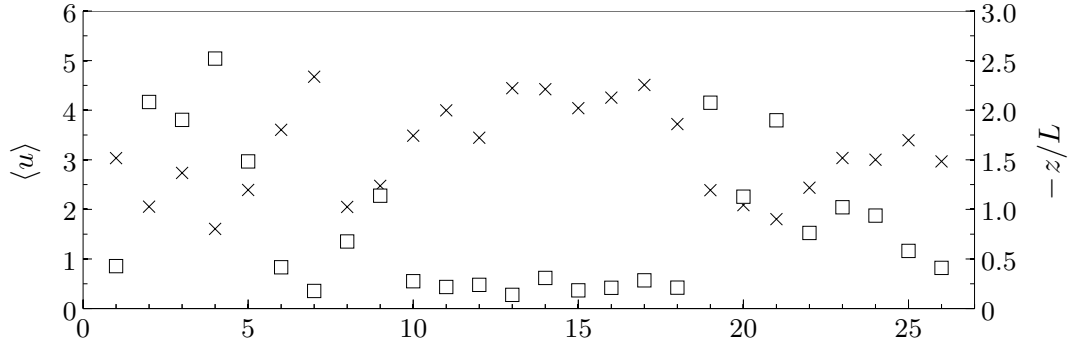

Figure 2.2: Measured mean wind velocity (×) and surface layer stability (□) for the 26 datasets used in the analyses.

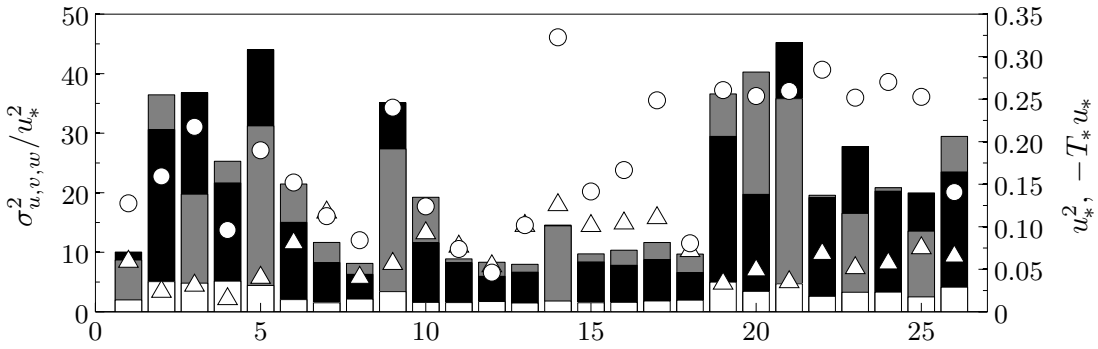

Figure 2.3: Measured Reynolds stress components (σ_u^2: top of black bars, σ_v^2: top of gray bars, σ_w^2: white bars), u_*^2 (△) and $-T_* u_*$ (○) for the 26 datasets used in the analyses.

Array	$(\Delta_f = 2d_y)$	$(\Delta_f = 4d_y)$	$(\Delta_f = 6d_y)$	$(\Delta_f = 8d_y)$
Wide 2	0.41	0.20	0.14	0.10
Medium 1	1.41	0.71	0.47	0.35
Medium 2	1.87	0.94	0.62	0.47

Table 2.2: The filter (grid) aspect ratio, z/Δ_f, for three-, five-, seven-, and nine-point cross-wind filter widths; z refers to the height of the primary array z_p.

2.3 Results

In the present study, we examine the dynamics of the SGS stress and scalar flux and their dependence on the stability condition of the surface layer and the filter width through the budgets of the SGS TKE, the SGS stress, and the SGS potential temperature flux. We investigate the dependence of the various terms in the SGS budgets on two non-dimensional parameters, z/L and Λ_w/Δ_f, where Λ_w is the wavelength corresponding to the peak of the vertical velocity spectrum. The dimensionless height, z/L, is a measure of the relative importance of heat convection to mechanical turbulence at height z. The wavelength–filter-width ratio, Λ_w/Δ_f, is a measure of the resolution of the filter relative to the turbulence field (i.e. a large value of Λ_w/Δ_f corresponds to a filter width much smaller than the energy-containing scales, and therefore a well-resolved LES field). Following Sullivan et al. (2003), we assume $\Lambda_w = 2\pi U t_f$ (where U and t_f are the mean velocity in the along-wind direction and the Eulerian integral time scale, respectively) using Taylor's hypothesis, and determine t_f by fitting an exponential of the form $\rho(t) = \exp(-t/t_f)$ to the autocorrelation function of the vertical velocity (Lenschow et al. 1993; Kaimal and Finnigan 1994).

In our analysis, the budget terms are non-dimensionalized using surface-layer scales u_*, Q_0, and z. Note that this differs from the study of Ramachandran and Wyngaard (2011), in which the terms in the budget of the deviatoric SGS stress are scaled by the energy dissipation rate (which is a function of the surface-layer stability, and therefore collapse the budget for all $z/L \leq 0$ when used as the scaling parameter).

In the following we plot the budget terms against Λ_w/Δ_f for three ranges of z/L. Because the data span a range of z/L, one-dimensional curve fits do not accurately represent the results. To obtain curves for different values of z/L, we least-squares fit a surface (as a function of Λ_w/Δ_f and z/L) to all available data. We then obtain one-dimensional slices of the surface for chosen values of z/L. This method ensures that the overall dependence of the data on both parameters is well-determined. For very large filter widths, the magnitudes of the SGS stress and flux should approach those of the Reynolds stress and flux. Therefore, the values of the curves for $\Lambda_w/\Delta_f = 0$ are obtained from previous results in the literature (e.g. the budgets of the total TKE from Wyngaard (1971) and those of the Reynolds shear stress and temperature flux from Wyngaard et al. (1971)).

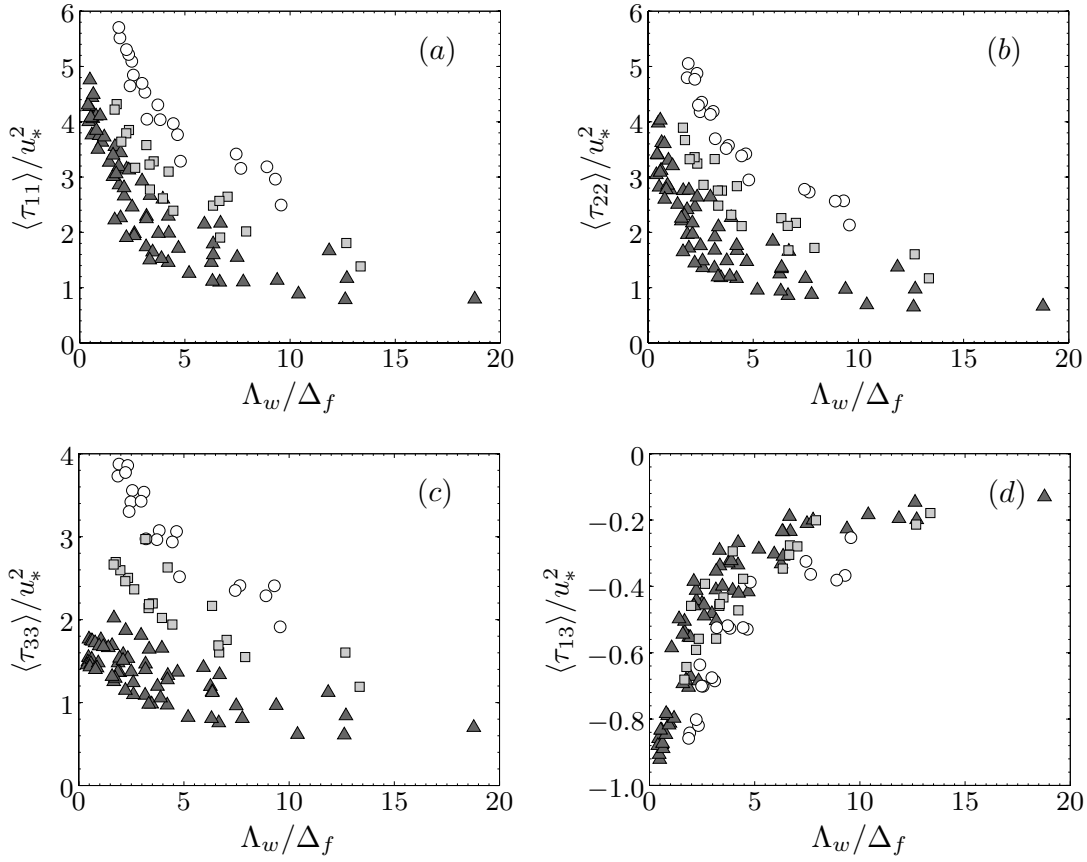

Figure 2.4: Measured mean SGS stress components for the weakly (▲: $0 < -z/L \leq 0.8$), moderately (□: $0.8 < -z/L \leq 1.5$), and strongly convective (○: $-z/L > 1.5$) surface layers.

2.3.1 SGS stress and flux

Before analysing their budgets, we first present the results for the mean SGS stress and temperature flux. The mean SGS stress is shown in figure 2.4 as a function of Λ_w/Δ_f for the weakly, moderately, and strongly convective surface layers. The SGS stress components have the largest magnitude near $\Lambda_w/\Delta_f = 0$ and decrease with increasing Λ_w/Δ_f (decreasing filter width). The normal components of $\langle\tau_{ij}\rangle$ show a clear dependence on the stability condition of the surface layer and increase with $-z/L$. The shear stress also generally increases with surface layer instability, however its dependence on z/L is weak. For very large filter widths, $\langle\tau_{11}\rangle > \langle\tau_{22}\rangle > \langle\tau_{33}\rangle$. The ratio of the mean horizontal SGS stress components to that of the vertical component (not shown) decreases with increasing $-z/L$. It also appears to decrease with increasing Λ_w/Δ_f (decreasing filter width).

The level of anisotropy of the SGS stress can be characterized using the Lumley triangle (Lumley 1978). Here, the two invariants, ξ and η, of the normalized anisotropy tensor

$$b_{ij} = \frac{\langle \tau_{ij} \rangle}{\langle \tau_{kk} \rangle} - \frac{1}{3}\delta_{ij} \tag{2.25}$$

are defined by (Pope 2000)

$$6\xi^3 \equiv 3\mathrm{III}_b = b_{ii}^3 = b_{ij}b_{jk}b_{ki}, \tag{2.26}$$

$$6\eta^2 \equiv -2\mathrm{II}_b = b_{ii}^2 = b_{ij}b_{ji}. \tag{2.27}$$

The invariants computed from the eigenvalues of the measured Reynolds and SGS stresses are shown in figure 2.5 as functions of Λ_w/Δ_f and z/L. In the left half of the Lumley triangle, the shape of the stress ellipsoid is a prolate spheroid (one small eigenvalue). In the right half, the stress ellipsoid is an oblate spheroid (one large eigenvalue). Sullivan et al. (2003) found the mean SGS stress in the weakly convective, neutral, and weakly stable surface layers (most of their data lying within $-0.5 \leq z/L \leq 0.5$) to be generally axisymmetric with one large eigenvalue. Our results for the near-neutral and convective surface layers show that the Reynolds stress is generally axisymmetric with one small eigenvalue because, for the convective surface layer, the variances of the u and v velocity components are much larger than that of the w component. The data points also appear to move closer to $\eta = -\xi$ as $-z/L$ increases since the Reynolds stress becomes more horizontally isotropic. The results for the SGS stress at large filter widths also follow this trend, with a stronger bias towards axisymmetric turbulence ($\xi < 0$) for increasing $-z/L$. For these filter widths, the level of anisotropy is stronger in the weakly convective surface layer. Since the peak of the u and v spectra occur at lower wavenumbers than that of the w spectrum (Kaimal et al. 1972), the filter affects mainly $\langle \tau_{11} \rangle$ and $\langle \tau_{22} \rangle$. The effects become stronger with increasing $-z/L$ since the spectral peaks for the u and v components move to lower wavenumbers; therefore the level of anisotropy decreases. As the filter width decreases, $\langle \tau_{11} \rangle$ and $\langle \tau_{22} \rangle$ fall off much faster than $\langle \tau_{33} \rangle$, but $\langle \tau_{11} \rangle > \langle \tau_{22} \rangle$; therefore the SGS stress tends toward axisymmetric turbulence with one large eigenvalue. The transition from one small eigenvalue to one large eigenvalue appears to occur at $2 \leq \Lambda_w/\Delta_f \leq 4$ and $4 \leq \Lambda_w/\Delta_f \leq 8$ for the moderately and strongly convective cases, respectively. For very small filter widths, the SGS stress should tend towards isotropy.

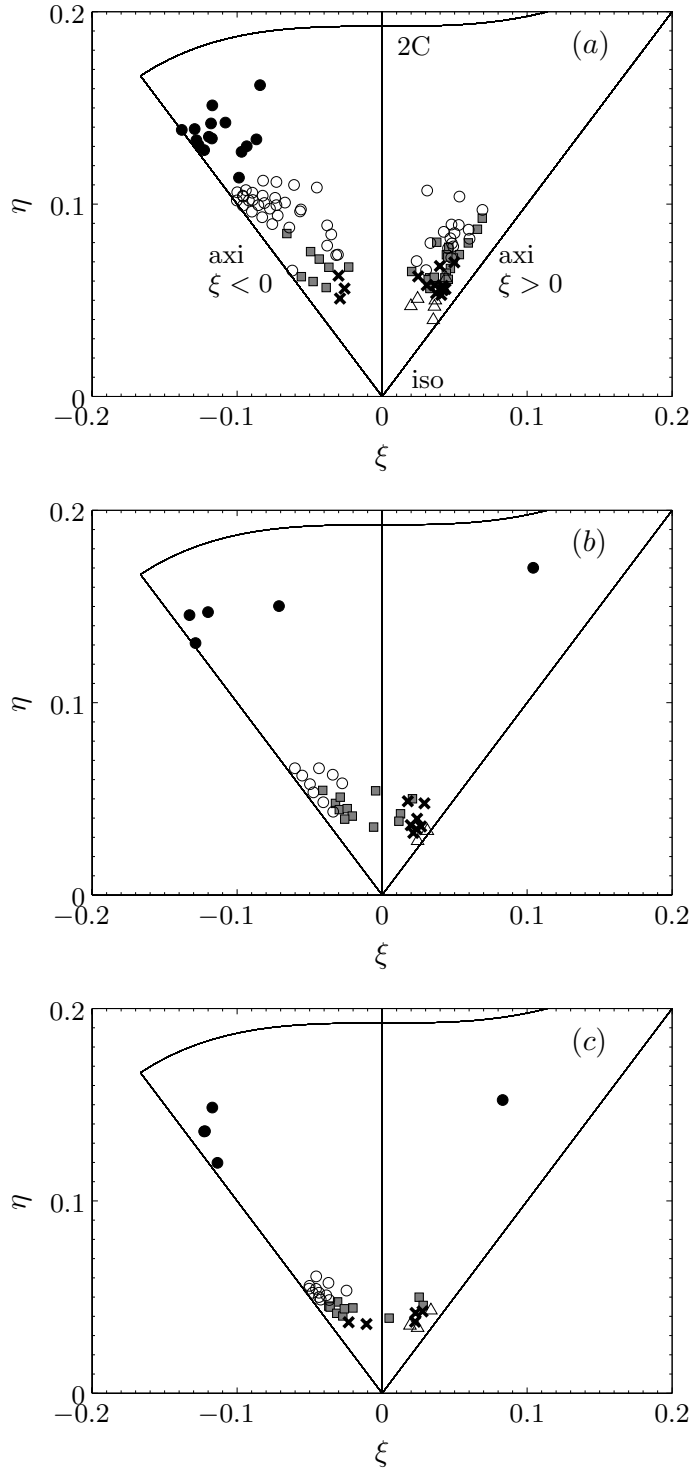

Figure 2.5: Lumley invariants of the mean Reynolds and SGS stress tensors for the (a) weakly ($0 < -z/L \leq 0.8$), (b) moderately ($0.8 < -z/L \leq 1.5$) and (c) strongly convective ($-z/L > 1.5$) surface layers: ●, Reynolds stress; ○, $0 < \Lambda_w/\Delta_f \leq 2$; ■, $2 < \Lambda_w/\Delta_f \leq 4$; ×, $4 < \Lambda_w/\Delta_f \leq 8$; △, $8 < \Lambda_w/\Delta_f \leq 20$.

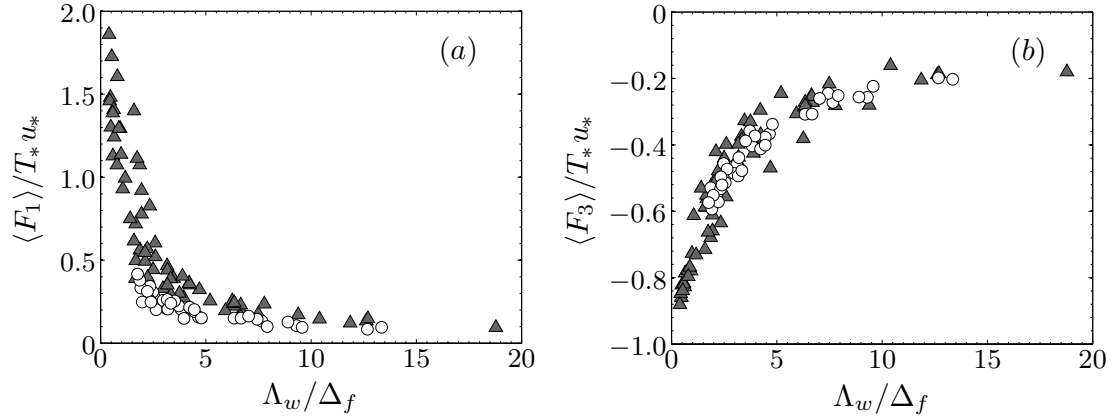

Figure 2.6: Measured mean SGS temperature flux components for the weakly (▲: $0 < -z/L \leq 1$) and strongly convective (○: $-z/L > 1$) surface layers.

The mean SGS potential temperature flux is shown in figure 2.6 as a function of Λ_w/Δ_f for the weakly and strongly convective surface layers. Note that the non-dimensionalized fluxes have the opposite sign relative to the actual fluxes since $T_* < 0$ for unstable surface layers. The results show that the SGS temperature flux has the largest magnitude near $\Lambda_w/\Delta_f = 0$ and decreases with increasing Λ_w/Δ_f. The horizontal temperature flux, $\langle F_1 \rangle$, shows a clear dependence on z/L and decreases with increasing instability, while the vertical flux, $\langle F_3 \rangle$, appears to be independent of z/L. For the near-neutral surface layer, $\langle F_1 \rangle$ is nearly twice the magnitude of $\langle F_3 \rangle$. However, as $-z/L$ increases, $\langle F_1 \rangle$ should vanish as the local free convection condition is approached (Wyngaard et al. 1971).

2.3.2 SGS TKE budget

In this section, we discuss the results for the various terms in the budget of the SGS TKE. The budget terms are non-dimensionalized by $\kappa z/u_*^3$. Assuming nominal horizontal homogeneity of the field site (i.e. that mean quantities vary only in the vertical direction), the turbulent transport and pressure transport terms are treated as non-zero only in the vertical direction. The SGS TKE budget equation (equation 2.10) thus reduces to

$$0 = \frac{1}{2}\frac{\partial}{\partial x_3}\langle T_{ii3}^{(t)} \rangle + \langle \mathcal{P} \rangle + \langle \mathcal{P}_B \rangle + \frac{1}{2}\frac{\partial}{\partial x_3}\langle T_{ii3}^{(p)} \rangle - \langle \epsilon \rangle. \tag{2.28}$$

Here, the viscous transport term is small and has been neglected, and $\langle \epsilon_{ks} \rangle$ is approximated by $\langle \epsilon \rangle$ since the filter scale is much larger than the Kolmogorov scale. We approximate the non-dimensional energy dissipation rate as $\kappa z \langle \epsilon \rangle / u_*^3 = -(1 + 0.75|z/L|^{2/3})^{3/2}$ as suggested by Caughey and Wyngaard (1979). The individual budget terms are presented separately in figures 2.7-2.10 to emphasize their dependencies on Λ_w/Δ_f and z/L. We then show a summary of the TKE budget in figure 2.11.

The non-dimensional mechanical production rate of the SGS TKE, $\kappa z \langle \mathcal{P} \rangle / u_*^3$, is shown in figure 2.7. The values of the curves for very small and very large Λ_w/Δ_f are based on the total TKE production rate and the dissipation rate, respectively. Here we use the mechanical production rate of the total TKE from Wyngaard (1971) to determine the values of the curves for $\Lambda_w/\Delta_f = 0$. For neutral surface layers, mechanical production and viscous dissipation are the dominant terms in the TKE budget. Therefore, in the limit as $-z/L$ and Λ_w/Δ_f approach zero, the mechanical production rate of the SGS TKE should approach that of the total TKE with a normalized value of $\kappa z \langle \mathcal{P} \rangle / u_*^3 = 1$. For unstable surface layers, the mechanical production rate for very small values of Λ_w/Δ_f should decrease with increasing $-z/L$ because the mean shear is weakened by the large convective eddies sweeping the surface layer (energy is also gained through buoyant production and pressure transport). As Λ_w/Δ_f increases (filter width decreases), the mechanical production rate for the unstable surface layers should increase as the energy gained by the resolvable scales due to buoyant production and pressure transport is increasingly cascading down to the subgrid scales through spectral transfer (i.e. the SGS mechanical production). It also increases with $-z/L$ because more energy enters the cascade due to the higher buoyant production and pressure transport at large scales. For very large values of Λ_w/Δ_f, the TKE budget reduces to a balance between the SGS production and viscous dissipation.

The buoyant production rate of the SGS TKE, shown in figure 2.8, is a gain in the unstable surface layer and increases with $-z/L$. For very small values of Λ_w/Δ_f (very large filter widths), the buoyant production rate of the SGS TKE should approach that of the total TKE and hence scale with the stability parameter. It has the maximum magnitude at $\Lambda_w/\Delta_f = 0$ and monotonically decreases with the filter width since buoyancy has a diminishing effect on the smaller SGS eddies (Wyngaard 2004).

Turbulent transport (shown in figure 2.9) exports energy upward, and therefore is a loss in the SGS TKE budget. The results for the weakly unstable surface layer and large filter widths

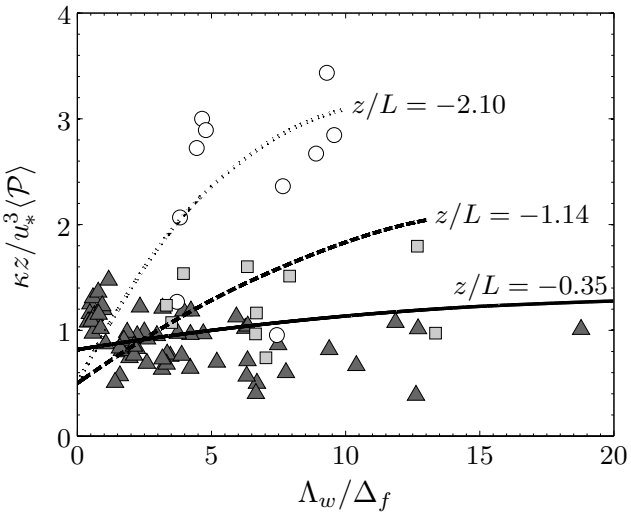

Figure 2.7: Non-dimensional mechanical production rate of SGS TKE as a function of Λ_w/Δ_f and z/L. The data are grouped into weakly (▲: $0 < -z/L \leq 0.8$), moderately (■: $0.8 < -z/L \leq 1.5$), and strongly convective (○: $-z/L > 1.5$) cases. The z/L value shown for each curve is the weight-averaged value for each stability group.

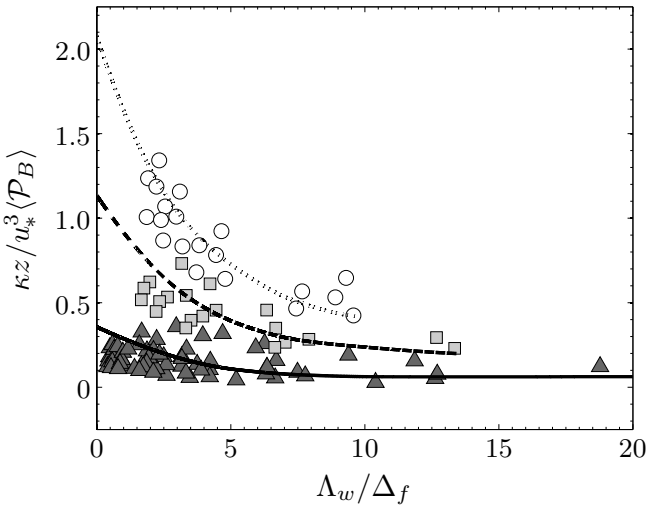

Figure 2.8: Non-dimensional buoyant production rate of SGS TKE as a function of Λ_w/Δ_f and z/L. The data are grouped as in figure 2.7.

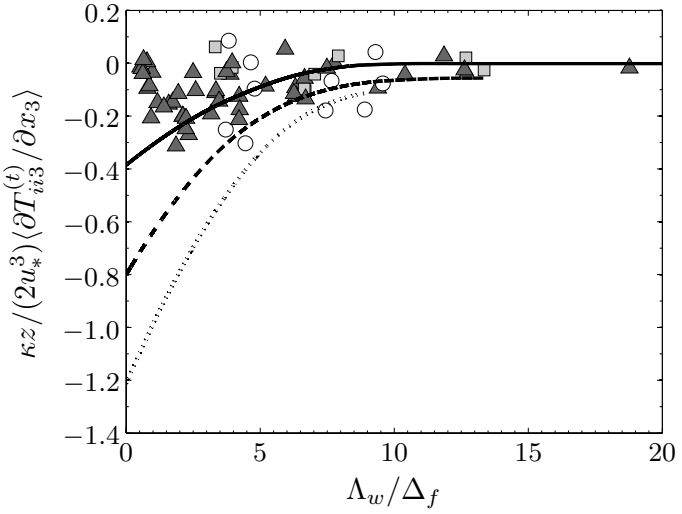

Figure 2.9: Non-dimensional turbulent transport rate of SGS TKE as a function of Λ_w/Δ_f and z/L. The data are grouped as in figure 2.7.

agree with Wyngaard et al. (1971), although the scatter is somewhat larger. This may be due to the errors involved in approximating vertical derivatives using one-sided finite differencing, in addition to the statistical uncertainties in computing third-order moments. In general, the rate of turbulent transport increases with $-z/L$ due to the stronger thermal plumes transporting energy upward. For each stability range, it has the maximum magnitude at $\Lambda_w/\Delta_f = 0$ and decreases with increasing Λ_w/Δ_f (decreasing filter width), asymptotically approaching zero for large values of Λ_w/Δ_f since transport has a diminishing effect on the smaller SGS eddies.

The rate of pressure transport of the SGS TKE is shown in figure 2.10 for three ranges of z/L (due to the amount of pressure data available, the mean stability values here differ from those of the previous figures). The pressure transport is a gain in the budget of the SGS TKE and increases with $-z/L$, while its magnitude has a trend similar to that of the SGS turbulent transport. In the limit as Λ_w/Δ_f approaches zero, the SGS pressure transport should approach that of the total TKE. So we compare our results with those of the total TKE budget obtained in previous studies: For near-neutral surface layers, the pressure transport is small and the primary source of energy is mechanical production (fed by the mean flow). For convective surface layers, our results show that the pressure transport is a major gain in the budget of the SGS TKE. Numerous studies have inferred the magnitude of the pressure transport term in the budget of the total TKE (e.g. Wyngaard and Coté 1971; McBean and Elliott 1975; Bradley et al. 1981; Wilczak and Businger

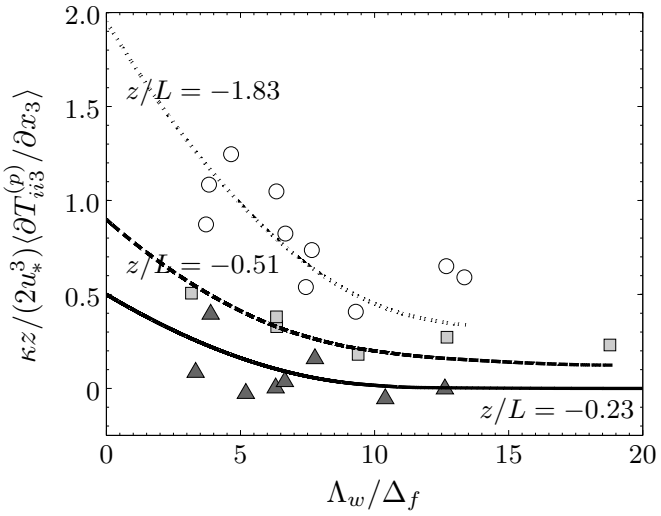

Figure 2.10: Non-dimensional pressure transport rate of SGS TKE for the weakly (▲: $0 < -z/L \leq 0.3$), moderately (■: $0.3 < -z/L \leq 1$), and strongly convective (○: $-z/L > 1$) surface layers.

1984), showing that it nearly balances the rate of turbulent transport for unstable surface layers. The magnitude of the pressure term inferred in these studies agree closely with those in figure 2.10 (for small values of Λ_w/Δ_f) for the given values of z/L. The trends in figure 2.10 for large values of Λ_w/Δ_f also agree with Elliott (1972), who analysed microscale pressure fluctuations measured within the ABL. He showed that large-scale pressure fluctuations are approximately in phase with downward velocity fluctuations, whereas, for small scales, there is a large phase difference. This was argued to be the result of the large eddies interacting with the surface and the small scales being 'free' from the effects of the ground. Thus, as Λ_w/Δ_f increases, the rate of pressure transport should decrease and asymptotically approach zero as the smaller SGS eddies are less affected by the surface.

To summarize the SGS TKE budget we show in figure 2.11 all of the terms discussed above. We plot the rate of viscous dissipation as a horizontal line since it is independent of Λ_w/Δ_f. For neutral surface layers, similar to the total TKE budget we expect an approximate balance between the mechanical production and the viscous dissipation for the SGS TKE budget. For near-neutral surface layers (figure 2.11*a*), the buoyant production, the SGS turbulent transport, and the SGS pressure transport begin to contribute to the budget. For unstable surface layers (figures 2.11*b* and 2.11*c*), the mechanical production, the buoyant production, and the SGS pressure transport are balanced by the SGS turbulent transport and the viscous dissipation for large filter widths.

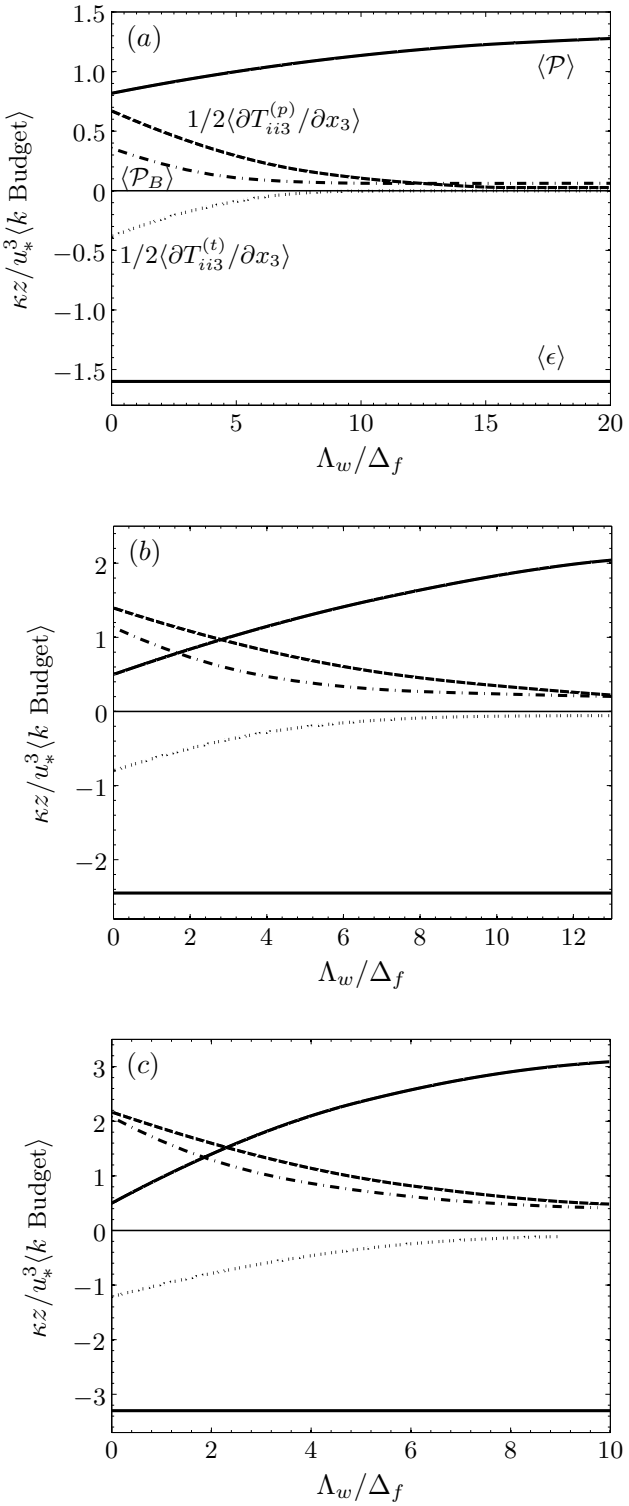

Figure 2.11: Summary of the SGS TKE budget as a function of Λ_w/Δ_f for (a) $z/L = -0.35$, (b) $z/L = -1.14$, and (c) $z/L = -2.10$. Mechanical production, $\mathcal{P}$; buoyant production, $\mathcal{P}_B$; turbulent transport, $1/2(\partial T^{(t)}_{ii3}/\partial x_3)$; pressure transport, $1/2(\partial T^{(p)}_{ii3}/\partial x_3)$; and dissipation, ϵ.

As the filter width decreases, the buoyancy and transport terms become less significant, and the budget is reduced to a balance between the mechanical production (spectral transfer) and the viscous dissipation, both increasing with $-z/L$. The magnitude and trends of each term, notably the gain by the SGS pressure transport under unstable conditions, are consistent with those of the total TKE summarized by Högström (1990) and Wyngaard (1992). The sum of the measured mechanical production, buoyant production, and SGS pressure transport balances the sum of the SGS turbulent transport and the viscous dissipation to within 10% of their magnitudes.

2.3.3 SGS stress budgets

In this section, we discuss the results for the various terms in the budgets of the SGS stress components. Owing to the nominal horizontal homogeneity of the field site, the pressure transport terms in the budgets of $\langle\tau_{11}\rangle$ and $\langle\tau_{22}\rangle$ are assumed to be zero. Hence, the SGS velocity–pressure-gradient correlation terms are equal to the SGS pressure–strain-rate correlations. Likewise, turbulent transport is non-zero only in the vertical direction. The budget equation (equation 2.1) for $\langle\tau_{\alpha\alpha}\rangle$ ($\alpha = 1, 2$; no summation) thus reduces to

$$0 = \frac{\partial}{\partial x_3}\langle T^{(t)}_{\alpha\alpha 3}\rangle + \langle P_{\alpha\alpha}\rangle + \langle \mathcal{R}_{\alpha\alpha}\rangle - \langle \epsilon_{\alpha\alpha}\rangle, \tag{2.29}$$

where the viscous transport term in equation 2.1 has been neglected and $\langle\epsilon_{s\alpha\alpha}\rangle$ is approximated as $\langle\epsilon_{\alpha\alpha}\rangle = 2\nu\langle(\partial u_\alpha/\partial x_k)^2\rangle$. The budget equations for $\langle\tau_{33}\rangle$ and $\langle\tau_{13}\rangle$ are

$$0 = \frac{\partial}{\partial x_3}\langle T^{(t)}_{333}\rangle + \langle P_{33}\rangle + \langle P_{B33}\rangle + \langle \mathcal{R}_{33}\rangle - \frac{\partial}{\partial x_3}\langle T^{(p)}_{333}\rangle - \langle \epsilon_{33}\rangle \tag{2.30}$$

and

$$0 = \frac{\partial}{\partial x_3}\langle T^{(t)}_{133}\rangle + \langle P_{13}\rangle + \langle P_{B13}\rangle + \langle \Pi_{13}\rangle, \tag{2.31}$$

respectively. The viscous transport and dissipation are small and are neglected in equation 2.31.

The budget of the SGS stress component $\langle\tau_{11}\rangle$, given by equation 2.29, includes the mechanical production, the turbulent transport, the pressure–strain-rate correlation, and the dissipation. The mechanical production rate of $\langle\tau_{11}\rangle$, $\langle P_{11}\rangle$, is shown in figure 2.12. Note that for very small values of Λ_w/Δ_f (very large filter widths), $\langle\tau_{ij}\rangle$ should approach the Reynolds stress. Hence, for the near-neutral surface layer, $\langle P_{11}\rangle$ should approach a normalized value of $\kappa z\langle P_{11}\rangle/u_*^3 = 2$ (twice the pro-

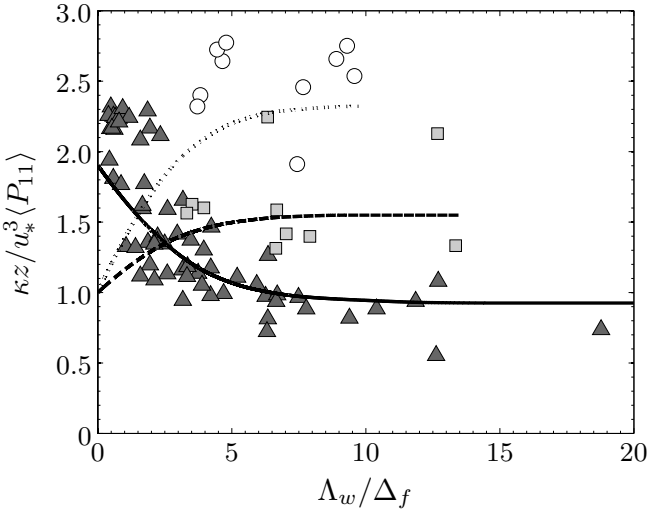

Figure 2.12: Non-dimensional production rate of $\langle \tau_{11} \rangle$ for the weakly (▲: $0 < -z/L \leq 0.8$), moderately (□: $0.8 < -z/L \leq 1.5$), and strongly convective (○: $-z/L > 1.5$) surface layers.

duction rate of the total TKE), thereby balancing the normalized dissipation rate ($\kappa z \langle \epsilon_{11} \rangle / u_*^3 = 2$). For very large values of Λ_w/Δ_f (very small filter widths), $\langle P_{11} \rangle$ essentially becomes the spectral transfer rate for $\langle \tau_{11} \rangle$, which equals two-thirds of the SGS TKE. Therefore $\langle P_{11} \rangle$ should approach a normalized value of $(2/3)\kappa z \langle \epsilon \rangle / u_*^3 = 2/3$, the dissipation rate of $\langle \tau_{11} \rangle$ under neutral stability. For weakly convective surface layers, $\langle P_{11} \rangle$ decreases with increasing Λ_w/Δ_f (decreasing filter width). For moderately and strongly convective surface layers, $\langle P_{11} \rangle$ appears to increase with Λ_w/Δ_f; it also increases with $-z/L$. For these surface layers, $\langle P_{11} \rangle$ for very small Λ_w/Δ_f should be smaller than that under near-neutral conditions because the mean shear is weakened by the convective mixing. Again we use the results for the Reynolds stress obtained by Wyngaard (1971) to determine the values of the curves for $\Lambda_w/\Delta_f = 0$. For very large values of Λ_w/Δ_f, $\langle P_{11} \rangle$ becomes the spectral transfer rate, which is higher for unstable surface layers due to the high buoyant production rate of the resolvable scales, resulting in more energy cascading down to the subgrid scales. Hence, $\langle P_{11} \rangle$ is higher and increases with $-z/L$.

The rate of turbulent transport of $\langle \tau_{11} \rangle$, $\langle \partial T_{113}^{(t)} / \partial x_3 \rangle$, shown in figure 2.13, is a loss in the budget of $\langle \tau_{11} \rangle$. The results for the weakly unstable surface layer and $\Lambda_w/\Delta_f = 0$ agree well with Wyngaard and Coté (1971), although there is some scatter. In general, the magnitude of $\langle \partial T_{113}^{(t)} / \partial x_3 \rangle$ increases with increasing instability and decreases with decreasing filter width, asymptotically approaching zero for large values of Λ_w/Δ_f since the mentioned inhomogeneity has a diminishing effect

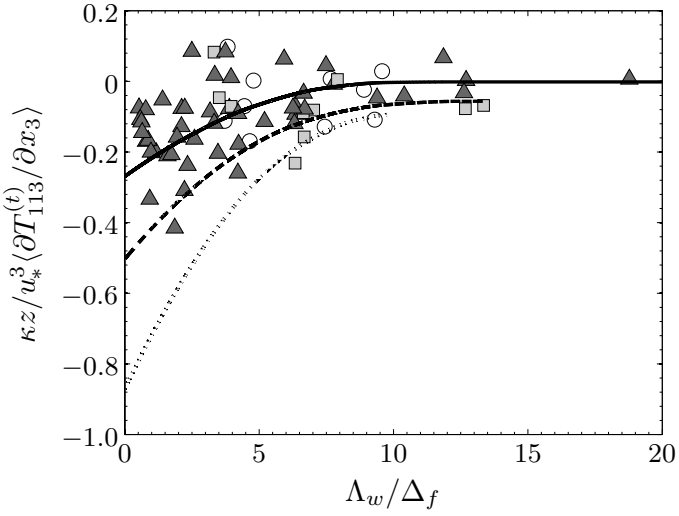

Figure 2.13: Non-dimensional turbulent transport rate of $\langle\tau_{11}\rangle$ as a function of Λ_w/Δ_f and z/L. The data are grouped as in figure 2.12.

on the smaller SGS eddies.

The SGS pressure–strain-rate correlation term in the budget of $\langle\tau_{11}\rangle$, $\langle\mathcal{R}_{11}\rangle$, is shown in figure 2.14. For near-neutral surface layers, the subgrid scales gain energy primarily through $\langle P_{11}\rangle$ (at large filter widths). Hence for these surface layers, $\langle\mathcal{R}_{11}\rangle$ is a loss (negative), indicating that the pressure–strain-rate correlation is removing energy from $\langle\tau_{11}\rangle$ and redistributing it to the other normal SGS components ($\langle\tau_{22}\rangle$ and $\langle\tau_{33}\rangle$). It has the maximum magnitude at $\Lambda_w/\Delta_f = 0$. As Λ_w/Δ_f increases, $\langle P_{ij}\rangle$ and $\langle\tau_{ij}\rangle$ become less anisotropic; therefore the magnitude of $\langle\mathcal{R}_{11}\rangle$ decreases and approaches zero for very large values of Λ_w/Δ_f. For moderately and strongly convective surface layers, $\langle\mathcal{R}_{11}\rangle$ is positive for small values of Λ_w/Δ_f because it is a major gain for the Reynolds stress component $\langle u_1' u_1'\rangle$. This is due to the surface blockage of the large, downward returning, convective eddies (e.g. Wyngaard 1992), resulting in energy being transferred from the vertical ($\langle\tau_{33}\rangle$) to the horizontal velocity components. For larger $-z/L$, buoyancy is more dominant; thus the blockage effect is stronger and the energy being produced in the vertical direction is increasingly transferred to the horizontal components by the SGS pressure–strain-rate correlation, causing $\langle\mathcal{R}_{11}\rangle$ to increase (for small values of Λ_w/Δ_f). As Λ_w/Δ_f increases, the effects of the ground blockage and buoyancy are reduced for smaller eddies while the anisotropy in $\langle\tau_{ij}\rangle$ becomes relatively more important. Thus $\langle\mathcal{R}_{11}\rangle$ reverses sign for moderate values of Λ_w/Δ_f, becoming a sink in the budget of $\langle\tau_{11}\rangle$ and acting to transfer energy back to $\langle\tau_{33}\rangle$. This transition (zero crossing) occurs approximately at $\Lambda_w/\Delta_f = 3$

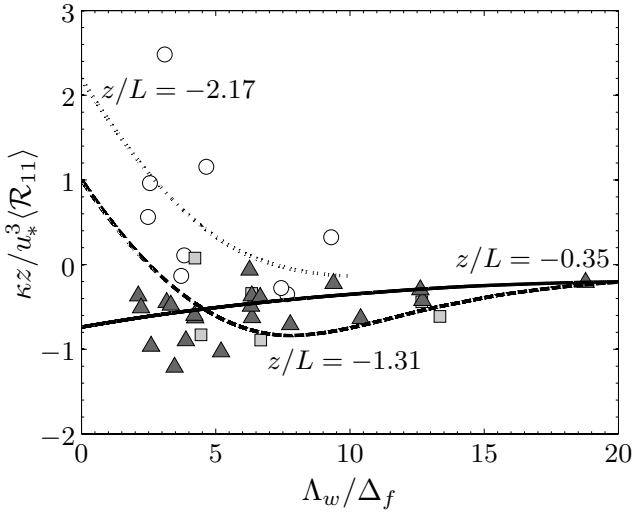

Figure 2.14: Non-dimensional SGS pressure–strain-rate correlation in the budget of $\langle\tau_{11}\rangle$ for the weakly (▲: $0 < -z/L \leq 0.75$), moderately (■: $0.75 < -z/L \leq 1.75$), and strongly convective (○: $-z/L > 1.75$) surface layers.

and 8 for the moderately and strongly convective cases, respectively, consistent with the transition of the SGS stress from one small to one large eigenvalue (figure 2.5). For very large values of Λ_w/Δ_f, $\langle\tau_{ij}\rangle$ becomes increasingly isotropic, and hence we expect the effects of $\langle\mathcal{R}_{ij}\rangle$ to diminish and $\langle\mathcal{R}_{11}\rangle$ to approach zero. Thus, $\langle\mathcal{R}_{11}\rangle$ has a non-monotonic dependence on Λ_w/Δ_f for large values of $-z/L$.

To summarize the $\langle\tau_{11}\rangle$ budget for unstable surface layers, we show in figure 2.15 all the budget terms as functions of Λ_w/Δ_f for $z/L = -2.10$. For very large filter widths, energy is supplied to $\langle\tau_{11}\rangle$ by the mechanical production and by the SGS pressure–strain-rate correlation (with energy transferred from $\langle\tau_{33}\rangle$), with the latter being the dominant source. These gains are balanced by the SGS turbulent transport and the viscous dissipation. As the filter width decreases, $\langle\mathcal{R}_{11}\rangle$ decreases and becomes negative before approaching zero for very small filter widths. The SGS turbulent transport also decreases (monotonically), resulting in a balance between the mechanical production and viscous dissipation. The imbalance of the terms in the budget is generally within 10% of the sum of the gain (or loss) terms.

The budget of the SGS stress component $\langle\tau_{22}\rangle$, given by equation 2.29, includes the mechanical production, the pressure–strain-rate correlation, the turbulent transport, and the viscous dissipation. The mechanical production rate of $\langle\tau_{22}\rangle$, $\langle P_{22}\rangle$, is shown in figure 2.16. In the limit as Λ_w/Δ_f approaches zero (very large filter widths), $\langle P_{22}\rangle$ should approach zero for all z/L since

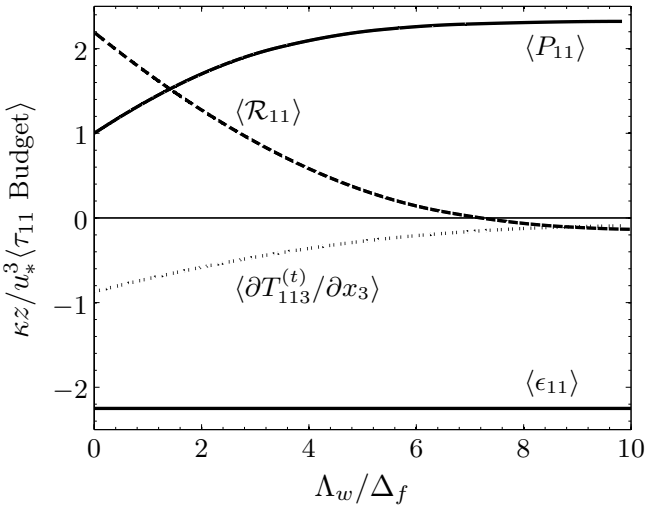

Figure 2.15: Summary of the budget of $\langle \tau_{11} \rangle$ as a function of Λ_w/Δ_f for $z/L = -2.10$.

the production rate of the Reynolds stress component $\langle u_2' u_2' \rangle$ is zero due to the nominal horizontal homogeneity of the surface layer. Figure 2.16 shows that $\langle P_{22} \rangle$ increases with increasing Λ_w/Δ_f (decreasing filter width) and increasing instability. Similar to $\langle P_{11} \rangle$, for very large values of Λ_w/Δ_f (very small filter widths) $\langle P_{22} \rangle$ should approach the mean dissipation rate, $\langle \epsilon_{22} \rangle = (2/3)\langle \epsilon \rangle$.

The SGS pressure–strain-rate correlation term in the budget of $\langle \tau_{22} \rangle$, $\langle \mathcal{R}_{22} \rangle$, is shown in figure 2.17. For weakly unstable surface layers and large filter widths, $\langle \mathcal{R}_{22} \rangle$ is a gain since the pressure–strain-rate correlation redistributes energy from $\langle \tau_{11} \rangle$ and $\langle \tau_{33} \rangle$ to $\langle \tau_{22} \rangle$ (for the surface layers studied, both $\langle \mathcal{R}_{11} \rangle$ and $\langle \mathcal{R}_{33} \rangle$ are negative). As Λ_w/Δ_f increases, the anisotropy in $\langle \tau_{ij} \rangle$ becomes relatively more important, causing $\langle \mathcal{R}_{22} \rangle$ to become a sink in the budget of $\langle \tau_{22} \rangle$ as energy is transferred back to $\langle \tau_{33} \rangle$. These effects become stronger with increasing instability. For strongly convective surface layers and small Λ_w/Δ_f, $\langle \mathcal{R}_{22} \rangle$ is positive with a larger magnitude. Again this is a result of the larger convective eddies being blocked by the surface and of increasing buoyancy production and pressure transport in the vertical direction, causing energy transfer from the vertical to the horizontal velocity components. Thus, the magnitude of $\langle \mathcal{R}_{22} \rangle$ increases (positively) with increasing instability. However, as Λ_w/Δ_f increases, the effects of the surface and buoyancy are again reduced while the anisotropy in $\langle \tau_{ij} \rangle$ becomes relatively more important. Therefore $\langle \mathcal{R}_{22} \rangle$ should reverse sign for moderate values of Λ_w/Δ_f, now becoming a loss in the budget of $\langle \tau_{22} \rangle$ and acting to drive $\langle \tau_{ij} \rangle$ towards isotropy. For very large values of Λ_w/Δ_f, we again expect $\langle \mathcal{R}_{22} \rangle$ to approach zero.

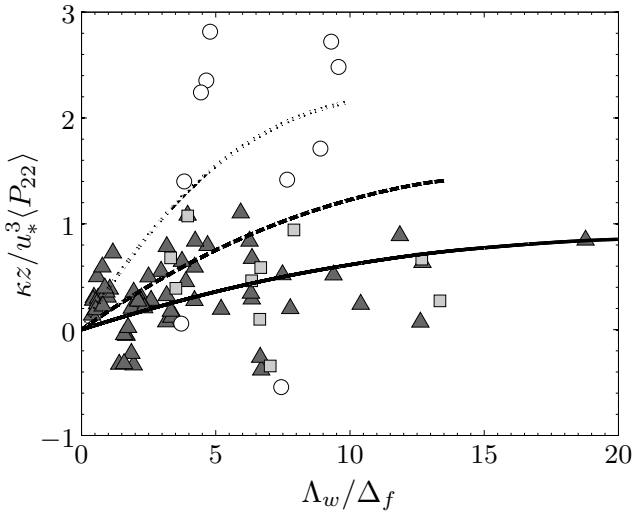

Figure 2.16: Non-dimensional production rate of $\langle \tau_{22} \rangle$ for the weakly (▲: $0 < -z/L \leq 0.8$), moderately (□: $0.8 < -z/L \leq 1.5$), and strongly convective (○: $-z/L > 1.5$) surface layers.

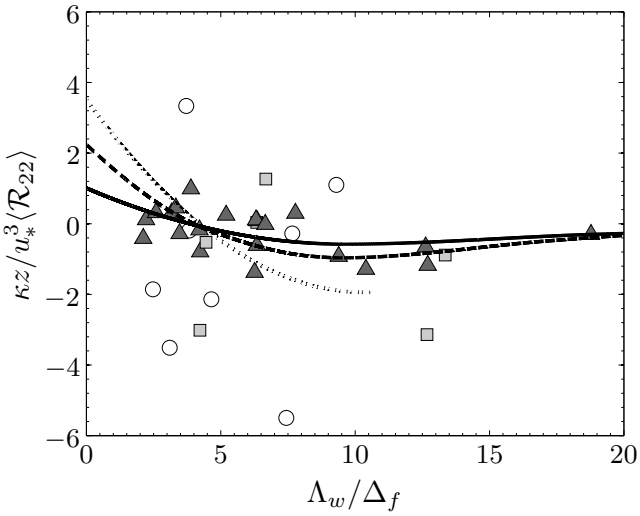

Figure 2.17: Non-dimensional SGS pressure–strain-rate correlation in the budget of $\langle \tau_{22} \rangle$ for the weakly (▲: $0 < -z/L \leq 0.75$), moderately (□: $0.75 < -z/L \leq 1.75$), and strongly convective (○: $-z/L > 1.75$) surface layers.

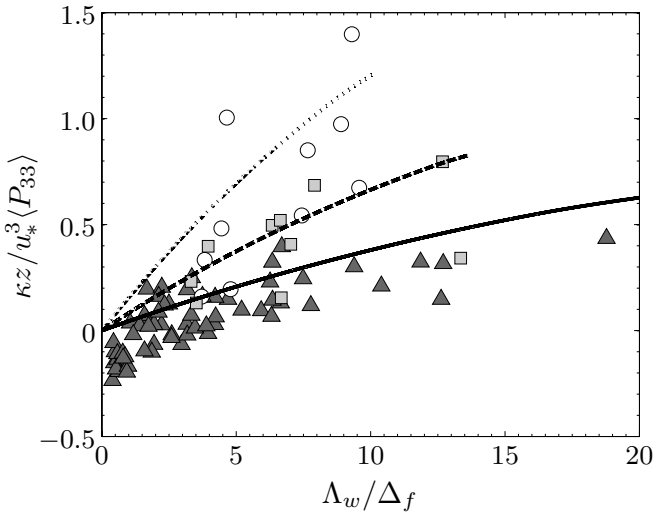

Figure 2.18: Non-dimensional production rate of $\langle\tau_{33}\rangle$ for the weakly (▲: $0 < -z/L \leq 0.8$), moderately (■: $0.8 < -z/L \leq 1.5$), and strongly convective (●: $-z/L > 1.5$) surface layers.

The budget of the SGS stress component $\langle\tau_{33}\rangle$, given by equation 2.30, includes the mechanical production, the buoyant production (same as that of the SGS TKE), the pressure–strain-rate correlation, the pressure transport (same as that of the SGS TKE), the turbulent transport, and the viscous dissipation. The mechanical production rate of $\langle\tau_{33}\rangle$, $\langle P_{33}\rangle$, is shown in figure 2.18. For very small values of Λ_w/Δ_f (very large filter widths), the magnitude of $\langle P_{33}\rangle$ is small because the mean shear does not contribute to $\langle P_{33}\rangle$. For smaller filter widths, $\langle P_{33}\rangle$ should increase with increasing instability because more resolvable-scale energy is cascading down to the subgrid scales. Figure 2.18 shows that $\langle P_{33}\rangle$ also increases with increasing Λ_w/Δ_f (decreasing filter width) because the buoyant production is smaller, thus $\langle\tau_{33}\rangle$ relies more on the spectral transfer to supply energy. For very small filter widths, $\langle P_{33}\rangle$ should approach $\langle\epsilon_{33}\rangle = (2/3)\langle\epsilon\rangle$, thereby balancing the mean dissipation rate. The buoyant production rate, $\langle P_{B33}\rangle$, is the same as that of the total SGS TKE (figure 2.8, with twice the magnitude). For moderately and strongly convective surface layers, buoyant production is a major gain in the budget of $\langle\tau_{33}\rangle$ for large filter widths, with the magnitude of $\langle P_{B33}\rangle$ increasing with increasing $-z/L$. This energy being produced in the vertical direction is then transferred to the horizontal components by the pressure–strain-rate correlation. For small filter widths, mechanical production is the dominant gain in the budget of $\langle\tau_{33}\rangle$, while $\langle P_{B33}\rangle$ approaches zero.

The SGS pressure–strain-rate correlation term in the budget of $\langle\tau_{33}\rangle$, $\langle\mathcal{R}_{33}\rangle$, is shown in figure 2.19. For strongly convective surface layers, $\langle\mathcal{R}_{33}\rangle$ should be a sink in the budget of $\langle\tau_{33}\rangle$ for

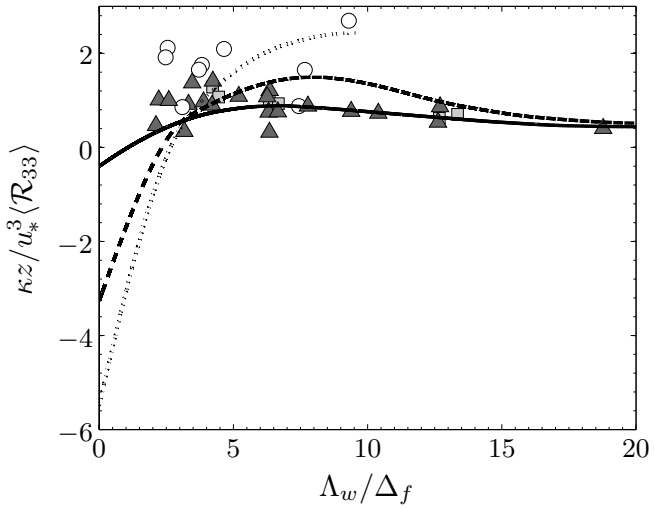

Figure 2.19: Non-dimensional SGS pressure–strain-rate correlation in the budget of $\langle\tau_{33}\rangle$ for the weakly (▲: $0 < -z/L \leq 0.75$), moderately (□: $0.75 < -z/L \leq 1.75$), and strongly convective (○: $-z/L > 1.75$) surface layers.

small values of Λ_w/Δ_f, again because energy is redistributed from $\langle\tau_{33}\rangle$ to $\langle\tau_{11}\rangle$ and $\langle\tau_{22}\rangle$. Here, energy gained in the vertical direction through buoyancy production and pressure transport is fed to the horizontal components by the pressure–strain-rate correlation as the vertical motion of the large convective eddies are blocked by the ground. As Λ_w/Δ_f increases, the anisotropy in $\langle\tau_{ij}\rangle$ becomes relatively more important than the effects of the ground blockage and buoyancy, causing $\langle\mathcal{R}_{33}\rangle$ to reverse sign and become positive ($\langle\tau_{33}\rangle$ now receiving energy from $\langle\tau_{11}\rangle$ and $\langle\tau_{22}\rangle$ through the pressure–strain-rate correlation). For very large values of Λ_w/Δ_f, we expect $\langle\mathcal{R}_{33}\rangle$ to approach zero as $\langle P_{33}\rangle$ becomes the main energy source. Hence, we expect $\langle\mathcal{R}_{33}\rangle$ to have a non-monotonic dependence on Λ_w/Δ_f under convective conditions. For neutral surface layers, $\langle\mathcal{R}_{33}\rangle$ should be positive (not shown) because it is the main energy source in the $\langle\tau_{33}\rangle$ budget. As Λ_w/Δ_f increases, $\langle\tau_{ij}\rangle$ becomes more isotropic, causing $\langle\mathcal{R}_{33}\rangle$ to decrease. For large values of Λ_w/Δ_f, we again expect $\langle\mathcal{R}_{33}\rangle$ to asymptotically approach zero as $\langle P_{33}\rangle$ becomes the dominant energy source.

The budget terms for $\langle\tau_{22}\rangle$ and $\langle\tau_{33}\rangle$ appear to have larger scatters and imbalances (typically 20% to 30%) compared to 10% for $\langle\tau_{11}\rangle$. However, the trends of the terms are consistent with each other and, for large filter widths, with those of the Reynolds stress. Thus these differences do not affect the conclusions drawn from the results.

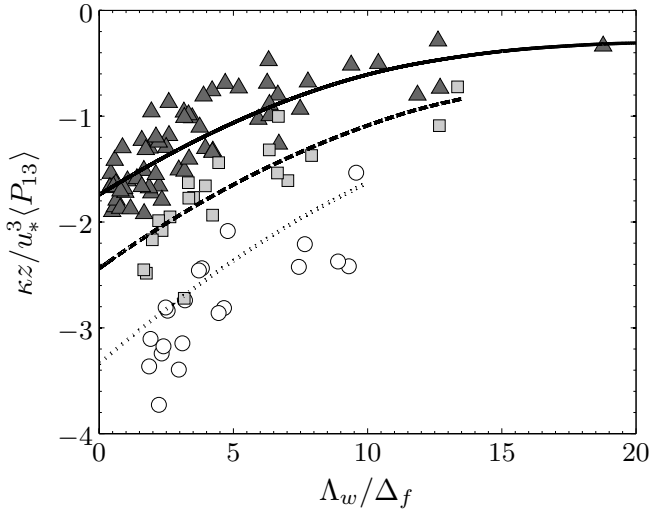

Figure 2.20: Non-dimensional shear production rate of $\langle\tau_{13}\rangle$ for the weakly (▲: $0 < -z/L \leq 0.8$), moderately (■: $0.8 < -z/L \leq 1.5$), and strongly convective (○: $-z/L > 1.5$) surface layers.

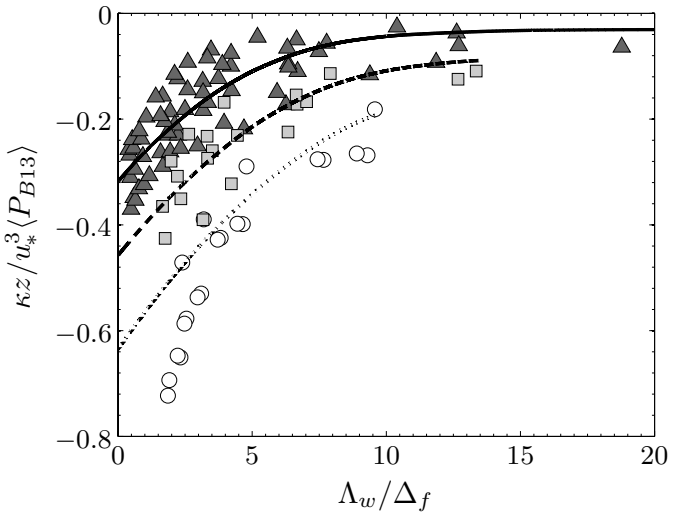

Figure 2.21: Non-dimensional buoyant production rate of $\langle\tau_{13}\rangle$ as a function of Λ_w/Δ_f and z/L. The data are grouped as in figure 2.20.

The budget of the SGS stress component $\langle\tau_{13}\rangle$, given by equation 2.31, is dominated by the shear production, the buoyant production, and the velocity–pressure-gradient correlation (turbulent transport is small, while viscous dissipation is negligible due to local isotropy). The SGS shear production rate and buoyant production rate of $\langle\tau_{13}\rangle$, $\langle P_{13}\rangle$ and $\langle P_{B13}\rangle$, are shown in figures 2.20

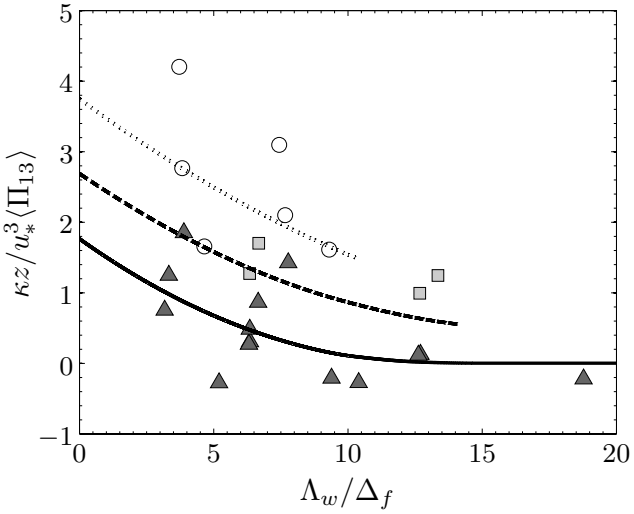

Figure 2.22: Non-dimensional SGS velocity–pressure-gradient correlation in the budget of $\langle\tau_{13}\rangle$ for the weakly (▲: $0 < -z/L \leq 0.75$), moderately (■: $0.75 < -z/L \leq 1.75$), and strongly convective (●: $-z/L > 1.75$) surface layers.

and 2.21, respectively. For very small values of Λ_w/Δ_f, the magnitudes of $\langle P_{13}\rangle$ and $\langle P_{B13}\rangle$ should approach the shear production and buoyant production rates of the Reynolds shear stress, respectively. Here, we use the production rates of the Reynolds shear stress obtained by Wyngaard et al. (1971) to determine the values of the curves for $\Lambda_w/\Delta_f = 0$. Figure 2.20 shows that $\langle P_{13}\rangle$ decreases (smaller magnitude, since $\langle\tau_{13}\rangle$ is negative) with increasing Λ_w/Δ_f because the production tensor $\langle P_{ij}\rangle$ and the SGS stress become more isotropic for smaller filter widths. Consistent with the trends of the Reynolds shear stress, $\langle P_{13}\rangle$ also increases with $-z/L$. The trends of $\langle P_{B13}\rangle$ are similar to those of $\langle P_{13}\rangle$, but the magnitude is smaller. Here $\langle P_{B13}\rangle$ approaches zero for neutral surface layers and increases with increasing $-z/L$. It monotonically decreases with increasing Λ_w/Δ_f (decreasing filter width).

The SGS velocity–pressure-gradient correlation, $\langle\Pi_{13}\rangle$, which combines the effects of the pressure–strain-rate correlation and the pressure transport, is generally positive (figure 2.22) and, hence, a loss in the shear stress budget. In the limit as Λ_w/Δ_f approaches zero, $\langle\Pi_{13}\rangle$ should approach the velocity–pressure-gradient correlation term in the budget of the Reynolds shear stress. Here, its trend and magnitude agree well with those inferred by Wyngaard et al. (1971). It monotonically decreases with increasing Λ_w/Δ_f (smaller filter width) and increases with increasing $-z/L$. The trends of $\langle\Pi_{13}\rangle$ generally counter those of $\langle P_{13}\rangle$ and $\langle P_{B13}\rangle$, thereby closing the quasi-steady

shear stress budget. Thus, in a way similar to the Reynolds shear stress budget, the SGS shear stress budget is dominated by the production and pressure destruction terms.

2.3.4 SGS temperature flux budgets

In this section, we discuss the results for the various terms in the budget equations of the SGS horizontal temperature flux, $\langle F_1 \rangle$,

$$0 = \frac{\partial}{\partial x_3} \langle T^{(t)}_{F13} \rangle + \langle P_{F1} \rangle + \langle \mathcal{R}_{F1} \rangle, \tag{2.32}$$

and the SGS vertical temperature flux, $\langle F_3 \rangle$,

$$0 = \frac{\partial}{\partial x_3} \langle T^{(t)}_{F33} \rangle + \langle P_{F3} \rangle + \langle P_{BF3} \rangle + \langle \Pi_{F3} \rangle. \tag{2.33}$$

Again, we assume nominal horizontal homogeneity of the field site, thus the pressure transport term is zero in equation 2.32. The budget terms are non-dimensionalized by $\kappa z/(T_* u_*^2)$. We summarize the behaviour of the production and pressure terms using fewer curves since their magnitudes vary slowly for $-z/L >> 1$ as the local free convection condition is approached (Wyngaard et al. 1971).

The budget of the SGS horizontal temperature flux, $\langle F_1 \rangle$, given by equation 2.32, includes the production (due to shear and stratification), the turbulent transport, and the pressure–temperature-gradient correlation. The total production rate of $\langle F_1 \rangle$, $\langle P_{F1} \rangle$, is shown in figure 2.23. For both weakly and strongly convective surface layers, $\langle P_{F1} \rangle$ is positive, with the largest magnitude at $\Lambda_w/\Delta_f = 0$. It monotonically decreases with increasing Λ_w/Δ_f (decreasing filter width) because the SGS velocity and scalar become less anisotropic (there must be anisotropy for a non-zero heat flux). It also decreases with increasing instability because the turbulence becomes more horizontally isotropic as local free convection is approached. The production rate of $\langle F_1 \rangle$ due to mean shear exceeds production due to stratification (not shown individually), however both terms follow the trends shown in figure 2.23. Turbulent transport is a gain, but is generally less than 10% of the production.

The pressure–temperature-gradient correlation term in the budget of $\langle F_1 \rangle$, $\langle \mathcal{R}_{F1} \rangle$, is shown in figure 2.24. For both weakly and strongly convective surface layers, $\langle \mathcal{R}_{F1} \rangle$ is negative, indicating that it is a sink in the budget of $\langle F_1 \rangle$ and acts to drive the turbulence scalar field towards isotropy.

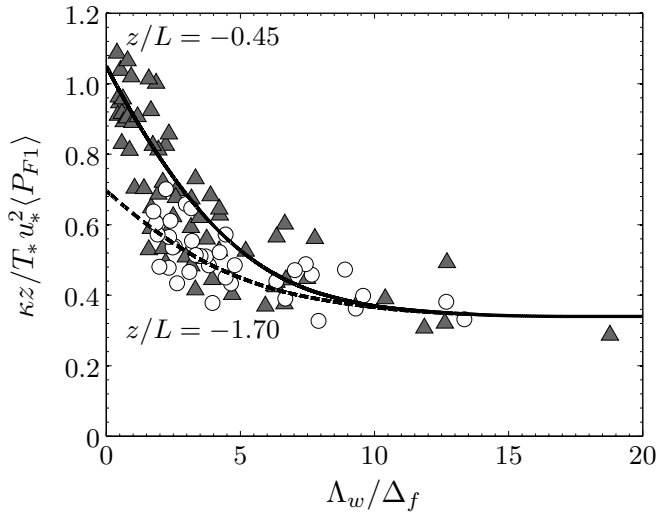

Figure 2.23: Non-dimensional production rate of SGS horizontal temperature flux for the weakly (▲: $0 < -z/L \leq 1$) and strongly convective (○: $-z/L > 1$) surface layers.

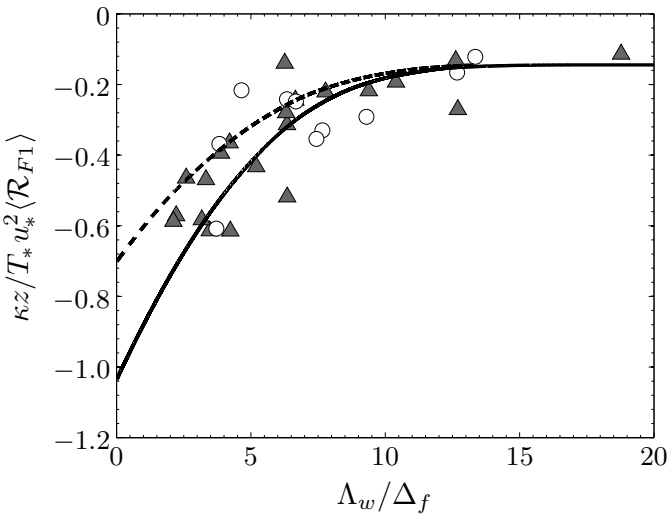

Figure 2.24: Non-dimensional SGS pressure–temperature-gradient correlation in the budget of $\langle F_1 \rangle$ as a function of Λ_w/Δ_f and z/L. The data are grouped as in figure 2.23.

It has the maximum magnitude at $\Lambda_w/\Delta_f = 0$, and decreases with increasing Λ_w/Δ_f (decreasing filter width) and increasing instability. The trends and magnitudes of $\langle \mathcal{R}_{F1} \rangle$ agree well with those inferred by Wyngaard et al. (1971) (for large filter widths) and approximately balance the measured SGS production (figure 2.23). The magnitude of the imbalance is within 15% of the total budget, similar to that obtained by Wilczak and Bedard (2004) for the budget of the total horizontal heat flux.

The budget of the SGS vertical temperature flux, $\langle F_3 \rangle$, given by equation 2.33, includes the stratification production, the buoyant production, the turbulent transport, and the temperature–pressure-gradient correlation (the shear production is zero due to horizontal homogeneity). The SGS stratification production and buoyant production rate of $\langle F_3 \rangle$, $\langle P_{F3} \rangle$ and $\langle P_{BF3} \rangle$, are shown in figures 2.25 and 2.26, respectively. For both weakly and strongly convective surface layers, $\langle P_{F3} \rangle$ and $\langle P_{BF3} \rangle$ are negative, indicating production of F_3. The values of the curves for $\Lambda_w/\Delta_f = 0$ are based on the results of Wyngaard et al. (1971) for the Reynolds vertical temperature flux, $\langle \theta' u_3' \rangle$. Under unstable conditions, Wyngaard et al. (1971) showed that $\langle \theta' u_3' \rangle$ is produced at an essentially constant rate and, hence, the curves for the moderately ($z/L = -0.45$) and strongly ($z/L = -1.70$) convective surface layers should collapse. As the filter width decreases, $\langle P_{F3} \rangle$ should also decrease since the stratification has a diminishing effect on the smaller SGS eddies. Similarly, the rate of buoyant production has the maximum magnitude at $\Lambda_w/\Delta_f = 0$ and increases slowly with $-z/L$ as local free convection is approached. It decreases with the filter width since the effects of buoyancy are diminished.

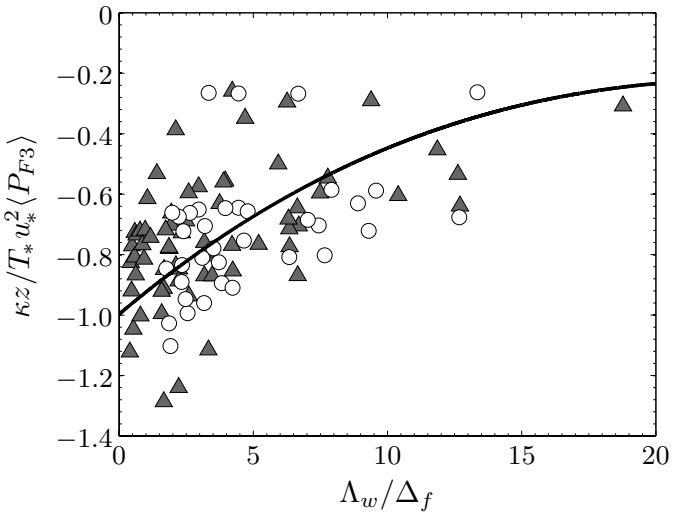

Figure 2.25: Non-dimensional production rate of SGS vertical temperature flux for the weakly (▲: $0 < -z/L \leq 1$) and strongly convective (○: $-z/L > 1$) surface layers.

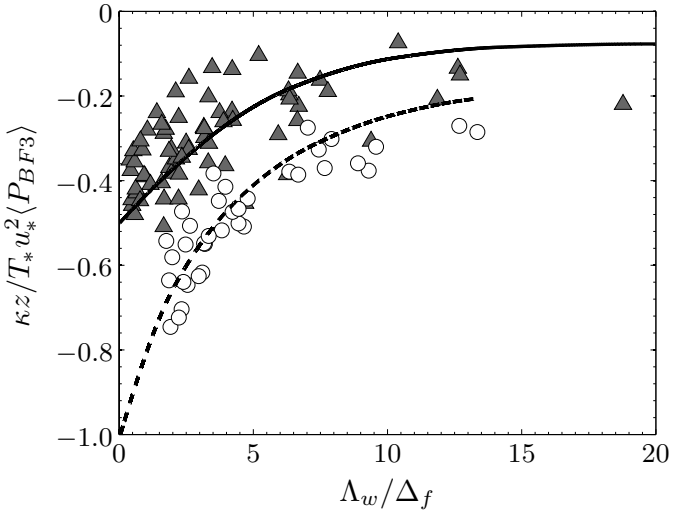

Figure 2.26: Non-dimensional buoyant production rate of SGS vertical temperature flux as a function of Λ_w/Δ_f and z/L. The data are grouped as in figure 2.25.

The temperature–pressure-gradient correlation, $\langle \Pi_{F3} \rangle$, which includes the effects of pressure transport and pressure destruction of $\langle F_3 \rangle$, is positive for both weakly and strongly convective surface layers (figure 2.27), indicating that it is a sink in the budget of $\langle F_3 \rangle$ and acts to drive the scalar field towards isotropy. It has the maximum magnitude at $\Lambda_w/\Delta_f = 0$ and should increase slowly

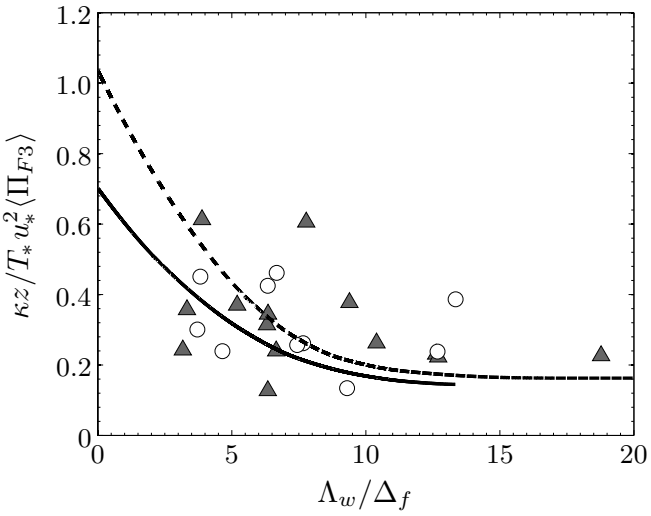

Figure 2.27: Non-dimensional SGS temperature–pressure-gradient correlation in the budget of $\langle F_3 \rangle$ as a function of Λ_w/Δ_f and z/L. The data are grouped as in figure 2.25.

with $-z/L$ since $\langle P_{F3} \rangle$ and $\langle P_{BF3} \rangle$ do the same. Although the trends of $\langle \Pi_{F3} \rangle$ counter those of $\langle P_{F3} \rangle$ and $\langle P_{BF3} \rangle$, our results show that its magnitude is only 50% of the total production. This imbalance may be due to the attenuation of the measured fluctuating vertical pressure gradient by the finite difference scheme. Note that this attenuation effect is different from that in evaluating the vertical derivative of a statistic (e.g. the SGS pressure transport term in the SGS TKE budget), which is much less affected by the finite spacing.

2.4 Discussion and conclusions

Turbulence measurement data from the AHATS field campaign were used to analyse the complete budgets of the SGS TKE, the SGS stress, and the SGS temperature flux in the convective atmospheric surface layer. In AHATS, the array technique previously used to obtain the SGS velocity and temperature was extended to include pressure sensors to measure the fluctuating pressure, enabling separation of the resolvable- and subgrid-scale pressure, and therefore for the first time allowing for all of the terms in the SGS stress and temperature flux transport equations to be obtained.

The results show that for large filter widths the SGS TKE budget is similar to that of the Reynolds stress TKE budget. For near-neutral surface layers, there is a balance between the me-

chanical production (a gain) and the viscous dissipation (a loss). For unstable surface layers, the gain terms, including the mechanical production, the buoyant production, and the SGS pressure transport, are balanced by the loss terms, including the SGS turbulent transport and the viscous dissipation. As the filter width decreases, the buoyancy and transport terms become less significant, and the budget is reduced to a balance between the mechanical production and the viscous dissipation.

Analyses of the SGS stress show that the budgets of the normal components of $\langle \tau_{ij} \rangle$ have more complex behaviours in unstable surface layers than in neutral surface layers due to the interactions among shear, buoyancy, pressure, and the presence of the ground. For neutral surface layers and very large filter widths, kinetic energy is supplied to $\langle \tau_{11} \rangle$ through the mean shear (mechanical) production. The pressure–strain-rate correlation transfers a portion of this energy to the $\langle \tau_{22} \rangle$ and $\langle \tau_{33} \rangle$ components. As the filter width decreases, the mechanical production for the latter components become significant. For very small filter widths, there is an eventual approach to equal partitioning of energy among the three normal components, and therefore the SGS pressure–strain-rate correlation vanishes.

For unstable surface layers, energy is supplied to $\langle \tau_{11} \rangle$ through the mechanical production and to $\langle \tau_{33} \rangle$ through the buoyant production and the SGS pressure transport. For very large filter widths, the SGS pressure–strain-rate correlation transfers energy from $\langle \tau_{33} \rangle$ to $\langle \tau_{11} \rangle$ and $\langle \tau_{22} \rangle$, while the mechanical production for $\langle \tau_{11} \rangle$ is smaller. Thus, in contrast to neutral surface layers, where the SGS pressure–strain-rate correlation acts to reduce the anisotropy in $\langle \tau_{ij} \rangle$, in unstable surface layers it is the main cause of anisotropy for large filter widths. In this case it contains both the effects of the ground blockage of the vertical downward motions of the large convective eddies and of the tendency to return to isotropy, with the former dominating. For smaller filter widths, the ground blockage effect is reduced and the effects of return to isotropy become relatively more important, therefore the pressure–strain-rate correlation reverses role and acts to transfer energy from $\langle \tau_{11} \rangle$ and $\langle \tau_{22} \rangle$ to $\langle \tau_{33} \rangle$. For very small filter widths, we expect $\langle \tau_{ij} \rangle$ to become increasingly more isotropic and the SGS pressure–strain-rate correlation to diminish. There is again an equal partitioning of energy among the three normal components, but with larger magnitudes than for the neutral surface layer.

Unlike those of the normal SGS stress components, the budgets of the SGS shear stress component, $\langle \tau_{13} \rangle$, and the SGS temperature flux components, $\langle F_i \rangle$, are qualitatively similar for neutral and unstable surface layers. They are an approximate balance between production and

pressure destruction. This aspect of the budgets is striking given the role played by the pressure transport and turbulent transport terms in the SGS dynamics in the unstable surface layer. In the budget of $\langle F_3 \rangle$, the measured pressure term does not completely balance the production terms, probably due to the finite difference scheme used to evaluate the vertical pressure derivative.

There is some imbalance in the measured budgets (10% for the SGS TKE, $\langle \tau_{11} \rangle$, and $\langle F_1 \rangle$; 20% to 30% for $\langle \tau_{22} \rangle$ and $\langle \tau_{33} \rangle$; and 50% for $\langle F_3 \rangle$). However, the trends of the terms are consistent with each other and, for large filter widths, with those of the Reynolds stress and flux. Thus these imbalances do not affect the conclusions drawn from the results.

The results of the present study have strong implications for modelling the SGS stress and flux. The approximate balance between production and pressure destruction for the mean SGS shear stress and temperature flux for neutral and unstable surface layers and for all filter widths indicates that the pressure plays the usual role of return-to-isotropy in the dynamics of $\langle \tau_{13} \rangle$ and $\langle F_i \rangle$. For unstable surface layers, however, the pressure–strain-rate correlation is the main cause of anisotropy in the normal SGS stress components for large filter widths (and, hence, for the normal Reynolds stress components). This change in the role of the pressure is due to the surface blockage of the large-scale vertical motions: the pressure fluctuations are largely due to the velocity field and its image field (with respect to the surface). Thus, Rotta's model is inconsistent with the measurement results; it has the opposite sign and cannot account for the ground effects for these filter widths. Therefore, using it alone is likely to underestimate the variances of the horizontal velocity components. Previous studies (e.g. Gibson and Launder 1978) have included an additional term to account for wall effects,

$$\mathcal{R}_{ij}^{(w)} = c_1' \frac{\epsilon}{k} \frac{l}{z\kappa} \left(\langle u_3 u_3 \rangle \delta_{ij} - \frac{3}{2} \langle u_i u_3 \rangle \delta_{j3} - \frac{3}{2} \langle u_j u_3 \rangle \delta_{i3} \right),$$

where $c_1' = 0.5$ and $l = -\langle u_1 u_3 \rangle^{3/2} / \epsilon$ is a length scale, which is approximately proportional to the integral length scale of the vertical velocity. In the surface layer, l/z is approximately constant, and the contribution from $\mathcal{R}_{ij}^{(w)}$ is determined only by $\langle u_i' u_j' \rangle$. Thus, the model effectively assumes that the ground blockage effects come from eddies of scale l, which would be valid for neutral boundary layers. In convective boundary layers, however, the large-scale convective eddies have length and velocity scales (z_i and w_*, respectively) much larger than the surface-layer scales (z and u_*), and ground blockage of these eddies results in much stronger pressure fluctuations than in neutral surface

layers. Thus, for Reynolds stress models and transport-equation-based SGS models at large filter scales, new models of $\mathcal{R}_{ij}$ reflecting the surface blockage of the large convective eddies are needed.

For very small filter widths, the effects of the surface are weaker and the pressure–strain-rate correlation causes return to isotropy. For intermediate filter widths, there is a competition between return to isotropy and ground blockage effects. Properly modelling these effects is expected to be important for predicting the SGS anisotropy.

Chapter 3

Investigation of subgrid-scale physics in the convective atmospheric surface layer using the budgets of the conditional mean subgrid-scale stress and temperature flux

3.1 Introduction

Although the SGS model affects the instantaneous LES flow field, its impact on the flow statistics is arguably more important. In fact, Langford and Moser (1999) and Pope (2004) argue that there exists only a statistical correspondence between an LES field and the true resolvable-scale flow field. To better understand the effects of the SGS turbulence on resolvable-scale statistics and those of the SGS model on LES statistics, Chen et al. (2003) and Chen and Tong (2006) developed a statistical approach based on the evolution equation of the one-time, one-point joint probability density function (JPDF) of the resolvable-scale velocity, which contains all one-point resolvable-scale velocity statistics. They showed that the necessary conditions for LES to correctly predict the resolvable-scale velocity JPDF are that the conditional means of the SGS stress and SGS stress production rate must be reproduced by the SGS model. Similarly, the effects of the SGS temperature flux on the resolvable-scale potential temperature can be studied statistically using the transport equation of the one-time, one-point probability density function (PDF) of the

resolvable-scale temperature, which shows that the necessary conditions for LES to correctly predict the resolvable-scale temperature PDF are that the conditional means of the SGS temperature flux and SGS temperature variance production rate must be reproduced by the SGS model.

Previous studies have successfully applied the JPDF equation to study the SGS dynamics, to identify SGS model deficiencies, and to evaluate SGS model performance in numerical simulations. *A priori* tests of the Smagorinsky model, the nonlinear model, the mixed model and the Kosović nonlinear model have found that, although these models can predict well certain components of the conditional mean SGS stress and SGS production rate, none are able to correctly predict both terms in full (Chen and Tong 2006). The Smagorinsky model and the Kosović nonlinear model under-predict the anisotropy and the variations of the level of anisotropy, which are considered to be important for predicting the mean shear and the streamwise velocity variance, whereas the nonlinear model and the mixed model over-predict both. These results are consistent with *a posteriori* tests performed using the JPDF equation (Chen et al. 2009).

To develop improved SGS parameterizations, additional physics, including history and non-local effects, must be incorporated into the SGS model. Transport-equation-based SGS models are well-suited for this purpose and have the potential to predict LES statistics with more accuracy (Deardorff 1972, 1973; Wyngaard 2004; Hatlee and Wyngaard 2007; Nguyen et al. 2013). Recent *a posteriori* tests of the transport-equation-based SGS model have found that the modelled SGS conservation equations could predict the conditional mean deviatoric SGS stress and its production rate better than could an eddy-diffusivity closure (Ramachandran 2010). Both, however, under-predict considerably the level of near-wall anisotropy. The enhanced performance of the transport-equation-based model was attributed to the inclusion of additional production and advection mechanisms that are absent in eddy-diffusivity closures, while its inability to predict correctly the SGS anisotropy was argued to be due to the absence of a model for the rapid pressure term in the modelled pressure–strain-rate correlation (Ramachandran and Wyngaard 2011). Recent analyses of the full SGS transport equations by Nguyen et al. (2013) using field measurement data, however, elucidated the role of the pressure–strain-rate correlation in the convective atmospheric surface layer and showed that it is the main cause of anisotropy, contrary to its commonly modelled role of causing return to isotropy. In the present study, we further investigate the SGS physics that govern the evolution of the resolvable-scale JPDF using the transport equations of the conditional mean SGS stress and SGS temperature flux.

In order for LES to predict correctly the resolvable-scale velocity JPDF and the resolvable-scale temperature PDF, the SGS model needs to predict the conditional mean SGS stress and the conditional mean SGS temperature flux. The former transports the velocity JPDF in both velocity and physical spaces, while the latter transports the temperature PDF in both scalar and physical spaces. To obtain the conditions for correctly predicting the conditional mean SGS stress and SGS flux, we utilize their transport equations, which are derived in appendix A following the method given by Pope (2010) for the self-conditioned LES field. The transport equation for the conditional mean SGS stress, $\langle \tau_{ij} | \boldsymbol{u}^r = \boldsymbol{v} \rangle$, is

$$\begin{aligned}\frac{\partial \langle \tau_{ij} | \boldsymbol{u}^r \rangle}{\partial t} =& - v_k \frac{\partial \langle \tau_{ij} | \boldsymbol{u}^r \rangle}{\partial x_k} - \left\langle \left(\frac{\partial u_l^r}{\partial t} + u_k^r \frac{\partial u_l^r}{\partial x_k} \right) \middle| \boldsymbol{u}^r \right\rangle \frac{\partial \langle \tau_{ij} | \boldsymbol{u}^r \rangle}{\partial v_l} \\ &+ \left\langle \frac{\partial}{\partial x_k} T_{ijk}^{(t)} \middle| \boldsymbol{u}^r \right\rangle + \langle P_{ij} | \boldsymbol{u}^r \rangle + \langle P_{Bij} | \boldsymbol{u}^r \rangle + \langle \Pi_{ij} | \boldsymbol{u}^r \rangle - \langle \epsilon_{ij} | \boldsymbol{u}^r \rangle \\ &- \frac{1}{f_u} \frac{\partial}{\partial v_l} \left[\mathrm{cov} \left(\tau_{ij} \, , \frac{\partial u_l^r}{\partial t} + u_k^r \frac{\partial u_l^r}{\partial x_k} \middle| \boldsymbol{u}^r \right) f_u \right], \end{aligned} \tag{3.1}$$

where u_i is the velocity and $\tau_{ij} = (u_i u_j)^r - u_i^r u_j^r$ is the conventional definition of the SGS stress (strictly, it is the SGS kinematic momentum flux or the negative of the apparent kinematic SGS stress), with superscript r denoting a resolvable-scale variable. We refer to $\langle \tau_{ij} | \boldsymbol{u}^r = \boldsymbol{v} \rangle$ as the conditional mean SGS stress, defined to be the mean SGS stress obtained for given values of the resolvable-scale velocity. For convenience, the notation $\langle \cdot \, | \boldsymbol{u}^r = \boldsymbol{v} \rangle$ has been abbreviated to omit the velocity sample-space variable $\boldsymbol{v}$ in (3.1) and hereinafter. The first two terms on the right-hand side of (3.1) represent advection of the conditional mean SGS stress in physical and velocity spaces, respectively, with the latter due to the conditional mean resolvable-scale acceleration. The remaining terms are, in order, the conditional means of the turbulent transport of τ_{ij}

$$\frac{\partial}{\partial x_k} T_{ijk}^{(t)} = \frac{\partial}{\partial x_k} \left[u_k^r \left(u_i u_j \right)^r - \left(u_i u_j u_k \right)^r + \left(\tau_{ik} u_j^r + \tau_{jk} u_i^r \right) \right], \tag{3.2}$$

the rate of mechanical production

$$P_{ij} = - \left(\tau_{ik} \frac{\partial u_j^r}{\partial x_k} + \tau_{jk} \frac{\partial u_i^r}{\partial x_k} \right), \tag{3.3}$$

the rate of buoyant production

$$P_{Bij} = \frac{g}{\Theta}\{\delta_{i3}\left[(\theta u_j)^r - \theta^r u_j^r\right] + \delta_{j3}\left[(\theta u_i)^r - \theta^r u_i^r\right]\}, \tag{3.4}$$

the velocity–pressure-gradient correlation

$$\Pi_{ij} = -\left[\left(u_i\frac{\partial p}{\partial x_j} + u_j\frac{\partial p}{\partial x_i}\right)^r - \left(u_i^r\frac{\partial p^r}{\partial x_j} + u_j^r\frac{\partial p^r}{\partial x_i}\right)\right], \tag{3.5}$$

and the rate of viscous dissipation and transport,

$$\epsilon_{ij} = 2\nu\left[\left(\frac{\partial u_i}{\partial x_k}\frac{\partial u_j}{\partial x_k}\right)^r - \frac{\partial u_i^r}{\partial x_k}\frac{\partial u_j^r}{\partial x_k}\right] + \nu\frac{\partial^2 \tau_{ij}}{\partial x_k \partial x_k}, \tag{3.6}$$

where Θ, θ, p, g, and ν are the mean and fluctuating potential temperatures, kinematic pressure, gravitational acceleration and kinematic viscosity, respectively, and δ_{ij} is the Kronecker delta. For high-Reynolds-number flows, viscous transport is small and viscous dissipation is almost entirely in the subgrid scales since the smallest resolvable scales are much larger than the Kolmogorov scale in the surface layer. The last term in (3.1) is the covariance of the conditional mean fluctuations of the SGS stress and the conditional mean resolvable-scale acceleration. The SGS velocity–pressure-gradient correlation can be decomposed into a pressure–strain-rate correlation and a pressure transport term,

$$\Pi_{ij} = \mathcal{R}_{ij} - \frac{\partial}{\partial x_k}T_{ijk}^{(p)}, \tag{3.7}$$

respectively, where

$$\mathcal{R}_{ij} = \left(p\frac{\partial u_i}{\partial x_j} + p\frac{\partial u_j}{\partial x_i}\right)^r - \left(p^r\frac{\partial u_i^r}{\partial x_j} + p^r\frac{\partial u_j^r}{\partial x_i}\right) \tag{3.8}$$

is the SGS pressure–strain-rate correlation tensor, and

$$T_{ijk}^{(p)} = \delta_{jk}\left[(pu_i)^r - p^r u_i^r\right] + \delta_{ik}\left[(pu_j)^r - p^r u_j^r\right]. \tag{3.9}$$

The trace of $\mathcal{R}_{ij}$ is zero, consequently the pressure–strain-rate correlation acts to redistribute energy among the three normal SGS stress components.

Equation 3.1 provides the necessary conditions for LES to correctly predict the conditional mean SGS stress: The conditional mean SGS mechanical and buoyant production, the conditional

mean SGS turbulent and pressure transport, the conditional mean SGS pressure–strain-rate correlation, and the conditional mean SGS dissipation must be reproduced by the SGS model. Since it is necessary to correctly predict the conditional mean SGS production in order to correctly model the conditional mean SGS stress, the necessary conditions for correctly predicting the resolvable-scale velocity JPDF are also implicitly satisfied. Similar to Reynolds stress modelling, the main challenge in transport-equation-based LES is expected to come from modelling of the pressure–strain-rate correlation.

The transport equation for the conditional mean SGS temperature flux, $\langle F_i|\theta^r=\psi\rangle$, also derived in appendix A, is

$$\begin{aligned}\frac{\partial\langle F_i|\theta^r\rangle}{\partial t}=&-\left\{\langle u_k^r|\theta^r\rangle\frac{\partial\langle F_i|\theta^r\rangle}{\partial x_k}+\operatorname{cov}\left(u_k^r\,,\frac{\partial F_i}{\partial x_k}\middle|\theta^r\right)\right\}\\&-\left\langle\left(\frac{\partial\theta^r}{\partial t}+\langle u_k^r|\theta^r\rangle\frac{\partial\theta^r}{\partial x_k}\right)\middle|\theta^r\right\rangle\frac{\partial\langle F_i|\theta^r\rangle}{\partial\psi}\\&+\left\langle\frac{\partial}{\partial x_k}T_{Fik}^{(t)}\middle|\theta^r\right\rangle+\langle P_{Fi}|\theta^r\rangle+\langle P_{BFi}|\theta^r\rangle+\langle\Pi_{Fi}|\theta^r\rangle\\&-\frac{1}{f_\theta}\frac{\partial}{\partial\psi}\left[\operatorname{cov}\left(F_i\,,\frac{\partial\theta^r}{\partial t}+\langle u_k^r|\theta^r\rangle\frac{\partial\theta^r}{\partial x_k}\middle|\theta^r\right)f_\theta\right],\end{aligned}\tag{3.10}$$

where $F_i=(\theta u_i)^r-\theta^r u_i^r$ is the SGS temperature flux in the i-direction. We refer to $\langle F_i|\theta^r=\psi\rangle$ as the conditional mean SGS temperature flux, defined to be the mean SGS temperature flux obtained for given values of the resolvable-scale temperature. Similarly, the notation $\langle\,\cdot\,|\theta^r=\psi\rangle$ has been abbreviated to omit the potential temperature sample-space variable ψ in (3.10) and hereinafter. The first two terms on the right-hand side of (3.10) represent advection of the conditional mean SGS temperature flux in physical and scalar spaces, respectively, with the latter due to the total time rate of change of the conditioning variable (the resolvable-scale temperature). The remaining terms are, in order, the conditional means of the turbulent transport of F_i

$$\frac{\partial}{\partial x_k}T_{Fik}^{(t)}=-\frac{\partial}{\partial x_k}\left[(\theta u_i u_k)^r-\theta^r(u_i u_k)^r-u_i^r(\theta u_k)^r-u_k^r(\theta u_i)^r+2\theta^r u_i^r u_k^r\right],\tag{3.11}$$

the rate of gradient (stratification) production and tilting production

$$P_{Fi}=-\tau_{ik}\frac{\partial\theta^r}{\partial x_k}-F_k\frac{\partial u_i^r}{\partial x_k},\tag{3.12}$$

respectively, the rate of buoyant production

$$P_{BFi} = \delta_{i3} \frac{g}{\Theta} \left[\left(\theta^2\right)^r - \left(\theta^r\right)^2 \right], \tag{3.13}$$

and the temperature–pressure-gradient correlation

$$\Pi_{Fi} = - \left[\left(\theta \frac{\partial p}{\partial x_i} \right)^r - \theta^r \frac{\partial p^r}{\partial x_i} \right]. \tag{3.14}$$

The last term in (3.10) is the covariance of the conditional mean fluctuations of the SGS flux and the substantial derivative of the resolvable-scale temperature. Note that the SGS temperature–pressure-gradient correlation can be decomposed into a correlation between the fluctuating pressure and temperature gradient and a transport term representing heat flux divergences due to the fluctuating pressure,

$$\Pi_{Fi} = \mathcal{R}_{Fi} - \frac{\partial}{\partial x_k} T^{(p)}_{Fik}, \tag{3.15}$$

respectively, where

$$\mathcal{R}_{Fi} = \left(p \frac{\partial \theta}{\partial x_i} \right)^r - p^r \frac{\partial \theta^r}{\partial x_i} \tag{3.16}$$

and

$$T^{(p)}_{Fik} = \delta_{ik} \left[(p\theta)^r - p^r \theta^r \right]. \tag{3.17}$$

Equation 3.10 provides the necessary conditions for LES to correctly predict the conditional mean SGS temperature flux: The conditional mean SGS gradient, tilting, and buoyant production, the conditional mean SGS turbulent and pressure transport, and the conditional mean SGS pressure–temperature-gradient correlation must be reproduced by the SGS model. Although the production terms for both the SGS stress and SGS flux are not directly modelled, they must be correctly predicted by the SGS model. Based on these conditions, investigations of the physics of the SGS stress and scalar flux should therefore focus on the conditional mean budget terms. In the present study, we analyse these budget terms and their dependence on the stability condition and filter width using field measurement data.

The rest of the paper is organized as follows. Section 3.2 outlines the field campaign and the use of sensor arrays to obtain resolvable- and subgrid-scale variables. Section 3.3 examines the dependence of the measured SGS terms on the surface layer stability and the filter width: the results

for the conditional mean SGS stress and the conditional mean SGS temperature flux are presented in §3.3.1, term-by-term analyses of their budgets are presented in §3.3.2 and §3.3.3, and the combined effects of the budgets terms on the conditional mean SGS stress are summarized in §3.3.4. Discussion and conclusions are given in §3.4. Derivations of the transport equations are presented in appendix A.

3.2 Field campaign

The field measurements for this study, named the Advection Horizontal Array Turbulence Study (AHATS), were conducted in the San Joaquin Valley, California, during the summer of 2008 as a collaboration between Clemson University, Penn State University, and the National Center for Atmospheric Research (NCAR). Horst et al. (2004) and Nguyen et al. (2013) describe the field site in detail. The field measurement design is based on the transverse array technique, proposed, studied, and first implemented successfully by Tong et al. (1997, 1998, 1999) for surface-layer measurements in the atmospheric boundary layer (ABL). In the context of LES, the technique uses horizontal sensor arrays to perform two-dimensional filtering to obtain resolvable- and subgrid-scale variables. It has subsequently been implemented by others in the ABL over land and ocean (Porté-Agel et al. 2001; Kleissl et al. 2003; Horst et al. 2004; Sullivan et al. 2006), within vegetation (Patton et al. 2011), over a glacier (Bou-Zeid et al. 2010), and in engineering flows (Cerutti et al. 2000; Tong 2001; Wang and Tong 2002; Rajagopalan and Tong 2003; Chen et al. 2003; Wang et al. 2004). Similar to these field studies, AHATS uses two vertically spaced arrays of sensors, shown in figure 3.1b, to obtain filtered variables and their derivatives. The arrays are centered in the lateral direction and aligned perpendicular to the prevailing wind direction.

In AHATS, a third line of sonic anemometers was added upwind to measure spatial differences in the streamwise direction (figure 3.1a). Additionally, two lines of turbulent pressure probes were added to measure, for the first time, the resolvable- and subgrid-scale pressure. The pressure probes are modified commercial versions of the quad-disk design by Nishiyama and Bedard (1991), which are insensitive to velocity fluctuations and are capable of measuring pressure covariances with reasonable accuracy (Wyngaard et al. 1994). The pressure probes are mounted level with the sonic anemometers and are offset slightly in the along- and cross-wind directions (figure 3.1c) relative to the sonic anemometers to avoid flow-induced distortion of the velocity measurements (Wyngaard

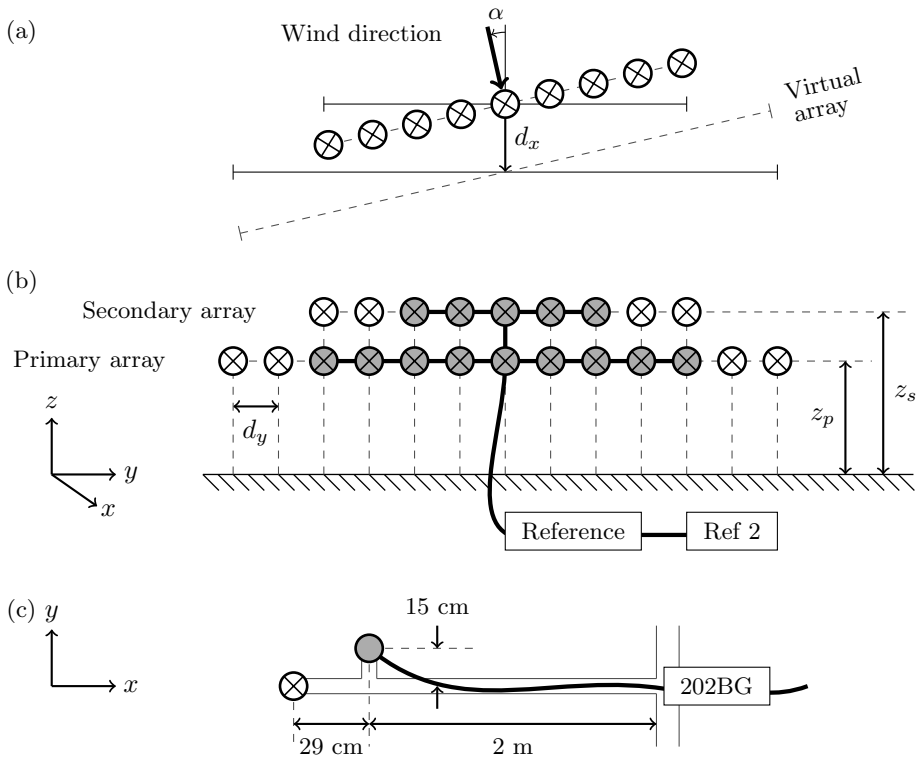

Figure 3.1: (a) Top view of arrays. The upwind and downwind arrays are centered laterally, with d_x denoting their streamwise separation distance. Due to variations in the run-averaged wind direction, we rotate the coordinate system and interpolate the velocity, temperature, and pressure in the virtual Cartesian coordinate system defined by the mean along-wind and cross-wind directions. (b) Front view of downwind array. Sonic anemometers ⊗ in the primary and secondary arrays are located at heights z_p and z_s, respectively; the horizontal spacing is d_y. Pressure ports ● are embedded at the center of the sonic arrays. (c) Top view of an individual mast. The reference side of the pressure transducers are connected to a common reference reservoir through thin tubing ——. An additional transducer measures the reference pressure using a second reference reservoir.

1981; Miller et al. 1999). Each probe is connected to a differential pressure transducer (Paroscientific Model 202BG), the reference side of which is connected to a common reference reservoir. Following Wilczak and Bedard (2004), the reference reservoir is filled with loosely packed steel wool and buried to prevent generation of dynamic pressure from convection and to maintain a uniform temperature (and hence pressure) through conduction. However, due to persistent low-frequency pressure fluctuations within the reference system induced by radiative heating and advective cooling of the reference tubing, an additional transducer was added to measure the reference pressure using a second reference reservoir. The absolute pressure is obtained by adding the reference pressure back to the measured (probe) pressure. This pressure signal still contains some residual low-frequency fluctuations (less than 0.05 Hz). However, because the lengths of the reference tubes are on the order of 10 m, the pipe-organ resonance frequencies are much higher; therefore, the tubes do not support acoustic waves of such low frequencies. Helmholtz resonance, if it exists, would be very weak and at much higher frequencies since the reference system is sealed. Thus, the low-frequency fluctuations have the same phase and affect the signals of all the pressure transducers in the same way. The fluctuations were found to affect the pressure terms in the Reynolds stress budget as well as those in the SGS stress budget for very large filter widths (those much larger than the horizontal integral length scale of the vertical velocity). Thus, we only obtain the SGS pressure terms for filter widths smaller than those of the energy-containing eddies.

In the present study, we use the arrays to approximate top-hat filters. In the streamwise direction, adoption of Taylor's hypothesis (Lumley 1965) allows using the time-filtered signal as a surrogate for streamwise spatial filtering. Filtering in the transverse direction is performed by weight-averaging the output of the sensor array (Tong et al. 1998). Streamwise and spanwise derivatives are approximated using fourth-order central finite-difference schemes, while vertical derivatives are approximated using a first-order one-sided finite difference scheme. The validity of the array filtering technique, including the accuracy of two-dimensional filtering and use of Taylor's hypothesis, has been thoroughly studied. Using a spectral cutoff array filter, Tong et al. (1998) showed that the r.m.s. values of the filtered variables differed from that of a true spectral cutoff filter by less than 10%. The accuracy of the top-hat array filter is expected to be higher (Chen and Tong 2006). They also showed two-dimensional filtering to be a good approximation of three-dimensional filtering with a 10% to 14% higher variance. Field measurements by Higgins et al. (2007) confirmed this result and showed that the difference can be interpreted as a 16% reduction in the filter size. Tong et al.

(1998) showed that among the mechanisms that could affect the accuracy of Taylor's hypothesis, including the effects of different convecting velocities for different wavenumber components, temporal changes in the reference moving with the mean velocity, and the fluctuating convecting velocity, only the last was significant. Kleissl et al. (2003) studied the errors associated with approximating gradients by finite differences; they evaluated the divergence-free condition for the filtered velocity field using fourth- and first-order finite difference schemes for the horizontal and vertical derivatives, respectively, and concluded that the errors were acceptable for studying the SGS dynamics. Horst et al. (2004) further examined various issues of using the array technique, including the aliasing errors associated with evaluating derivatives using finite differences, and furthermore demonstrated reasonable accuracy of the technique.

Five different array configurations, shown in table 3.1, are employed in AHATS in order to vary the filter (grid) aspect ratio, z/Δ_f, and the stability parameter, z/L, where z, Δ_f, and $L = -\left(u_*^3\Theta\right) / \left(\kappa g \langle u_3'\theta'\rangle\right)$ are the height above the ground, the filter width, and the Monin-Obukhov length, respectively, with primes denoting fluctuations and angle brackets denoting an ensemble average. We refer to z as the height of the primary array z_p here and hereinafter. Note, $\kappa = 0.41$, $u_* = (-\langle u_1' u_3'\rangle)^{1/2}$ (with u_1' in the mean wind direction), and $\langle u_3'\theta'\rangle = Q_0$ are the von Kármán constant, the friction velocity, and the vertical temperature flux, respectively. We define the surface-layer temperature scale by $T_* = -Q_0/u_*$. In the present work, we study the unstable surface layer (i.e. for which $z/L < 0$) using data from the medium and wide array configurations. The resolved fields are obtained using several different filter widths, resulting in a filter aspect ratio ranging from 0.10 to 1.87 and therefore allowing for the effects of grid anisotropy to be studied. We use 26 data segments, each generally $30 - 90$ min in length, collected during the daytime and spanning a wide range of $-z/L$. Each data segment has a steady mean velocity and approximately stationary fluctuating velocities. The lengths for most datasets correspond to approximately 2000 advection time scales of the vertical-velocity energy-containing eddies (evaluated as the ratio of the length of each dataset to its advection time scale, $t_a = z/U$, where U is the mean velocity in the along-wind direction); and, although the precise level of statistical uncertainty is difficult to determine for the statistics obtained, it is sufficiently low for determining the dependence of the statistics on the important parameters discussed in §3.3.

Array Spacing	Start PDT	End PDT	d_y (m)	d_x (m)	z_p (m)	z_s (m)	z_u (m)
Wide 1	1200 25 June	1200 01 July	4.00	16.00	3.24	4.24	3.74
Wide 2	1300 01 July	0600 18 July	4.00	16.00	3.24	4.24	3.24
Medium 1	1600 20 July	0600 29 July	1.29	5.12	3.64	4.64	3.64
Medium 2	1230 29 July	0600 08 Aug	1.29	5.12	4.83	5.83	4.83
Narrow	1800 09 Aug	0900 16 Aug	0.43	3.12	6.98	7.98	6.98

Table 3.1: AHATS array configurations, with z_u denoting the height of the upwind array. The streamwise array separation distance, d_x, was chosen to minimize flow distortion at the downwind array.

3.3 Results

In the following, we study the evolution of the conditional mean SGS stress and the conditional mean SGS temperature flux by analysing term-by-term their transport equations. A summary of the combined effects of the budget terms on the conditional mean SGS stress is given in §3.3.4. The dependence of the budget terms on the surface-layer stability and filter width are examined using two non-dimensional parameters, z/L and Λ_w/Δ_f, where Λ_w is the wavelength corresponding to the peak of the vertical-velocity spectrum (i.e. the horizontal integral length scale of the vertical velocity). The dimensionless height, z/L, is a measure of the stability of the surface layer. The wavelength–filter-width ratio, Λ_w/Δ_f, is a measure of the resolution of the filter relative to the turbulence field (i.e. a large value of Λ_w/Δ_f corresponds to a filter width much smaller than the energy-containing scales, and therefore a well-resolved LES field). Following Sullivan et al. (2003), we assume $\Lambda_w = 2\pi U t_f$ using Taylor's hypothesis, and determine the Eulerian integral time scale t_f by fitting an exponential of the form $\rho(t) = \exp(-t/t_f)$ to the autocorrelation function of the vertical velocity (Lenschow et al. 1993; Kaimal and Finnigan 1994). For sufficiently convective surface layers ($-z/L > 0.2$), the ratio z/Λ_w is constant.

In the present study, the SGS statistics are non-dimensionalized using surface-layer scaling: The conditional mean SGS pressure and conditional mean SGS stress are normalized by u_*^2, while the budget terms in the transport equation of the conditional mean SGS stress are normalized by $\kappa z/u_*^3$. The conditional mean temperature flux is normalized by $T_* u_*$, while the budget terms in its transport equation are normalized by $\kappa z/(T_* u_*^2)$.

The measured SGS stress and its budget terms are conditioned on the fluctuating parts of the streamwise and vertical components of the resolvable-scale velocity (u_1^r and u_3^r, respectively),

both of which are normalized by their respective resolved-scale r.m.s. values. The spanwise velocity component, u_2^r, plays a lesser role in the dynamics of the SGS stress (Chen and Tong 2006; Chen et al. 2009), and therefore is not included as a conditioning variable for most terms. The measured SGS temperature flux and its budget terms are conditioned on the fluctuating part of the resolvable-scale potential temperature, θ^r, normalized by its resolved-scale r.m.s. value. Conditional mean statistics are obtained using the first-order kernel density estimation method (Wand and Jones 1995), resulting in faster convergence and lower bias. We limit the results to the central part of the sample space containing at least 99.5% of the probability of the velocity and temperature PDFs. To achieve further statistical convergence, we weight-average and combine the results for data sets collected under similar stability conditions with comparable values of Λ_w/Δ_f.

3.3.1 Conditional mean SGS stress and SGS temperature flux

Following previous studies of subgrid-scale physics in the weakly convective atmospheric surface layer (Chen and Tong 2006; Chen et al. 2010), we first present the results for the conditional mean SGS stress and SGS temperature flux and examine their filter-scale dependence in the strongly convective surface layer. The results for the conditional mean SGS stress (figure 3.2) show that $\langle \tau_{ij} | \boldsymbol{u}^r \rangle$ generally increases with u_1^r (u_2^r) and u_3^r due to the stronger vertical shear and buoyancy acceleration. To better understand the effects of the filter width, we characterize the level of anisotropy of $\langle \tau_{ij} | \boldsymbol{u}^r \rangle$ in figure 3.3 using the Lumley triangle (Lumley 1978). Here, the two invariants, ξ and η, of the normalized anisotropy tensor

$$\langle b_{ij} | \boldsymbol{u}^r \rangle = \frac{\langle \tau_{ij} | \boldsymbol{u}^r \rangle}{\langle \tau_{kk} | \boldsymbol{u}^r \rangle} - \frac{1}{3}\delta_{ij} \tag{3.18}$$

defined by (Pope 2000)

$$6\xi^3 \equiv 3\mathrm{III}_b = \langle b_{ii} | \boldsymbol{u}^r \rangle^3 = \langle b_{ij} | \boldsymbol{u}^r \rangle \langle b_{jk} | \boldsymbol{u}^r \rangle \langle b_{ki} | \boldsymbol{u}^r \rangle, \tag{3.19}$$

$$6\eta^2 \equiv -2\mathrm{II}_b = \langle b_{ii} | \boldsymbol{u}^r \rangle^2 = \langle b_{ij} | \boldsymbol{u}^r \rangle \langle b_{ji} | \boldsymbol{u}^r \rangle, \tag{3.20}$$

are used characterize the shape of the stress ellipsoid and the state of SGS anisotropy. In the left half of the Lumley triangle, the shape of the stress ellipsoid is a prolate spheroid (one small

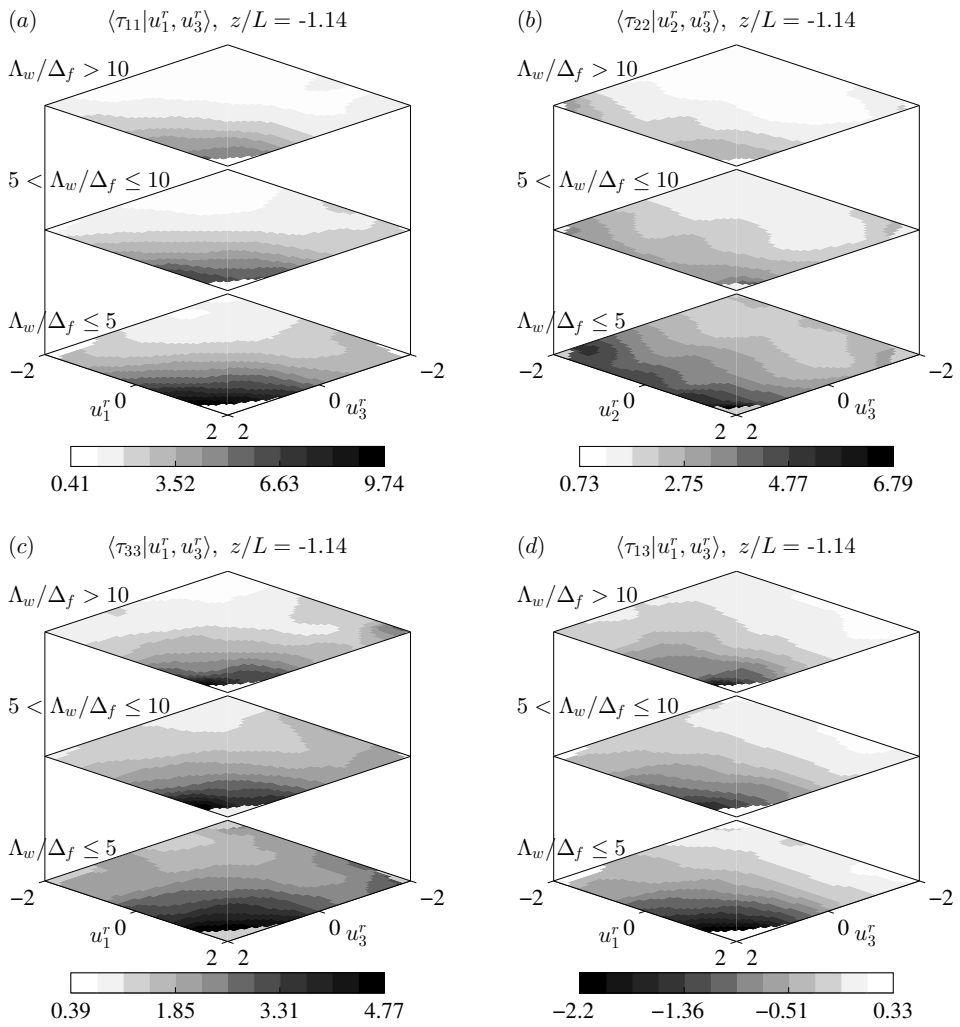

Figure 3.2: Conditional mean of the measured SGS stress components for the strongly convective ($0.8 < -z/L \leq 1.5$) surface layer.

eigenvalue). In the right half, the stress ellipsoid is an oblate spheroid (one large eigenvalue). If $\langle\tau_{ij}|\boldsymbol{u}^r\rangle$ is isotropic, both ξ and η are zero. The results in figure 3.3 show that the conditional mean SGS stress is generally close to axisymmetric and is less anisotropic (smaller values of ξ and η) for the strongly convective surface layer than for the weakly convective one due to the weaker vertical shear. For large filter widths, figures 3.3(a) and 3.3(c) show that $\langle\tau_{ij}|\boldsymbol{u}^r\rangle$ is quite anisotropic when u_3^r is positive. For negative u_1^r, the state of anisotropy is close to $\eta = -\xi$ (one small eigenvalue) since the SGS stress is more horizontally isotropic due to the weaker vertical shear. For positive u_1^r, it transitions toward $\eta = \xi$ (one large eigenvalue) due to stronger shear. When u_3^r is negative, the SGS stress is generally much less anisotropic.

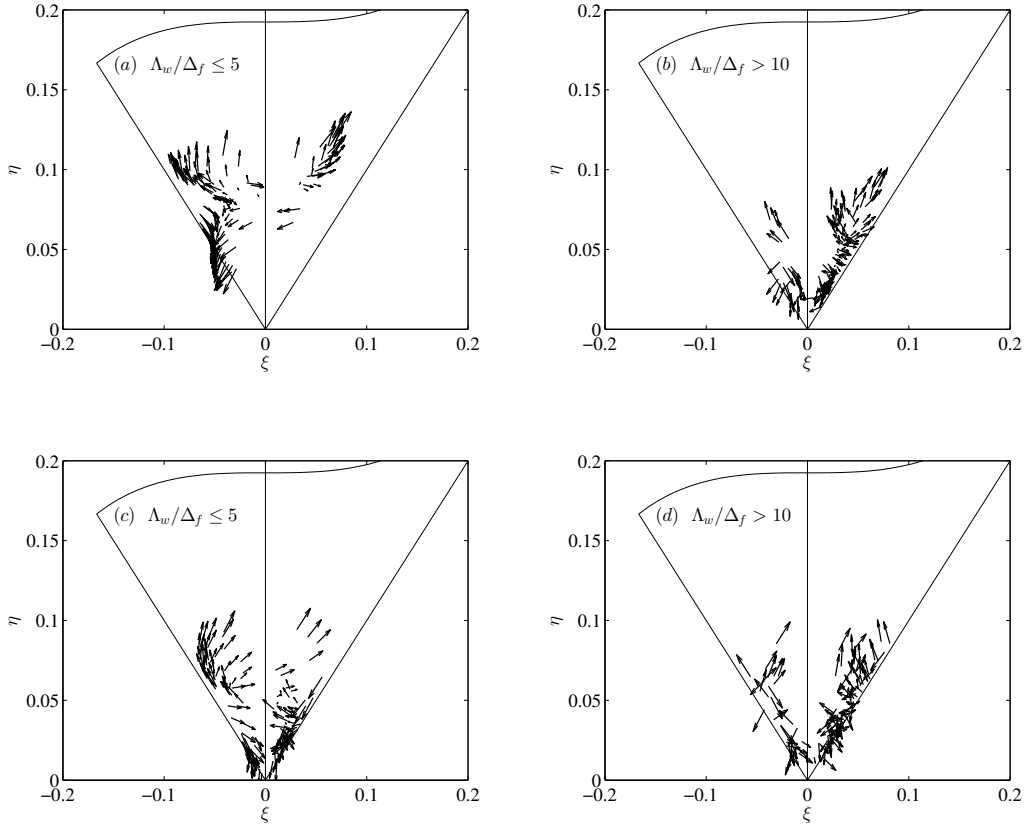

Figure 3.3: The Lumley triangle representation of the invariants, ξ and η, characterizing the anisotropy of the conditional mean SGS stress for the (a)-(b) weakly ($0 < -z/L \leq 0.8$) and (c)-(d) strongly convective ($0.8 < -z/L \leq 1.5$) surface layers. Arrows represent the conditioning velocity vector (u_1^r, u_3^r).

As the filter width decreases (figures 3.3(b) and 3.3(d)), the state of anisotropy tends to move toward $\eta = \xi$, indicating that $\langle \tau_{ij} | \boldsymbol{u}^r \rangle$ is close to axisymmetric with one large eigenvalue. This change is consistent with the fact that the peaks of the u and v spectra occur at lower wavenumbers than that of the w spectrum (Kaimal et al. 1972), and therefore a smaller filter width will cause $\langle \tau_{11} | \boldsymbol{u}^r \rangle$ and $\langle \tau_{22} | \boldsymbol{u}^r \rangle$ to fall off much faster than $\langle \tau_{33} | \boldsymbol{u}^r \rangle$. In addition, the shear production plays a greater role, resulting in larger magnitudes of $\langle \tau_{11} | \boldsymbol{u}^r \rangle$ compared to $\langle \tau_{22} | \boldsymbol{u}^r \rangle$ (figure 3.2). For very small filter widths, however, the SGS stress appears to approach isotropy. The results also show that the peak of the conditional mean SGS stress decreases by at most 40% when the filter width is decreased by a factor of 5 (figure 3.2), while the magnitude of the (unconditional) mean SGS stress $\langle \tau_{ij} \rangle$ decreases by nearly 60% for the same filter width reduction (Nguyen et al. 2013). Therefore, although it is less anisotropic, the dependence of $\langle \tau_{ij} | \boldsymbol{u}^r \rangle / \langle \tau_{ij} \rangle$ (the magnitude of the conditional mean SGS stress relative to its unconditional mean) on $\boldsymbol{u}^r$ does not become weaker as the filter width decreases, contrary to the notion of local isotropy, which suggests that the dependence of SGS stress on the resolvable-scale velocity should weaken.

The horizontal and vertical components of the conditional mean SGS potential temperature flux, $\langle F_1 | \theta^r \rangle$ and $\langle F_3 | \theta^r \rangle$, are shown in figures 3.4 and 3.5, respectively, for the weakly and strongly convective surface layers. We note that the non-dimensionalized conditional mean fluxes have the opposite signs relative to the actual fluxes since $T_* < 0$ for unstable surface layers. The results show that $\langle F_1 | \theta^r \rangle$ ($\langle F_3 | \theta^r \rangle$) is positive (negative) and increases in magnitude with θ^r. For negative θ^r, the magnitude of $\langle F_i | \theta^r \rangle$ is smaller and its dependence on θ^r is weaker. It also decreases with increasing Λ_w / Δ_f since the SGS temperature flux is more isotropic for smaller filter widths. The horizontal flux is weaker for the strongly convective surface layer since, in a horizontally homogeneous surface layer, horizontal scalar flux is produced primarily by tilting of vertical scalar flux by vertical wind shear (Hatlee and Wyngaard 2007; Chen et al. 2010), which disappears under free convection. In contrast, the vertical flux appears to be much less dependent on the surface-layer instability.

Similar to the conditional mean SGS stress, the conditional mean SGS temperature flux has a non-diminishing dependence on the resolvable-scale temperature for all filter widths, although its level of anisotropy decreases. Figures 3.4 and 3.5 show that the peaks of the conditional mean SGS horizontal and vertical fluxes decrease by at most 50% when the filter width is decreased by a factor of 5, although the magnitudes of the mean fluxes decrease by nearly 70% for the same filter width reduction (Nguyen et al. 2013). Therefore, although it is less anisotropic, the dependence of

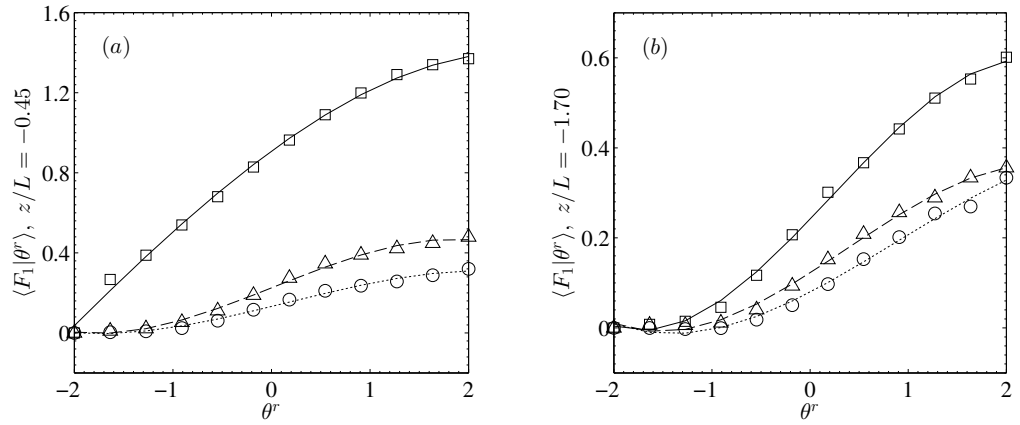

Figure 3.4: Conditional mean of the measured SGS horizontal temperature flux for the (a) weakly ($0 < -z/L \leq 1$) and (b) strongly convective ($1 < -z/L \leq 2.5$) surface layers and varying values of the wavelength–filter-width ratio: $\square$: $\Lambda_w/\Delta_f \leq 5$, $\triangle$: $5 < \Lambda_w/\Delta_f \leq 10$, $\bigcirc$: $\Lambda_w/\Delta_f > 10$.

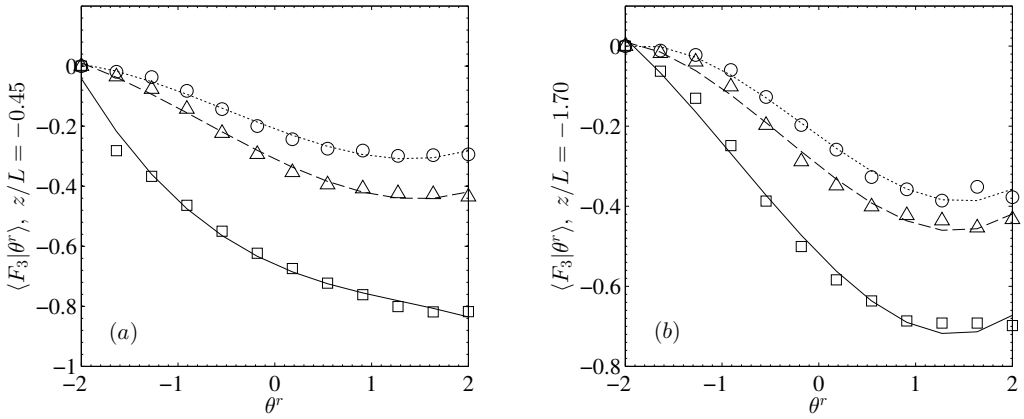

Figure 3.5: Conditional mean of the measured SGS vertical temperature flux for the (a) weakly ($0 < -z/L \leq 1$) and (b) strongly convective ($1 < -z/L \leq 2.5$) surface layers. The data are grouped as in figure 3.4.

the normalized conditional mean SGS temperature flux $\langle F_i|\theta^r\rangle/\langle F_i\rangle$ does not become weaker as the filter width decreases, suggesting that it has a strong influence on the resolvable-scale temperature PDF even for inertial-range filter widths.

3.3.2 Conditional mean SGS stress budget

3.3.2.1 *Conditional mean SGS production*

The results for the conditional mean SGS production rate show that the trends of $\langle P_{11}|\boldsymbol{u}^r\rangle$ and $\langle P_{22}|\boldsymbol{u}^r\rangle$ are similar to those of $\langle \tau_{11}|\boldsymbol{u}^r\rangle$ and $\langle \tau_{22}|\boldsymbol{u}^r\rangle$ (generally increasing with u_3^r) and therefore are not repeated here. The trends of $\langle P_{B33}|\boldsymbol{u}^r\rangle$ are similar to those of $\langle \tau_{33}|\boldsymbol{u}^r\rangle$, while $\langle P_{33}|\boldsymbol{u}^r\rangle$ generally decreases with u_3^r. Instead, to better understand the conditional energy transfer among the normal components of the SGS stress by $\langle P_{\alpha\alpha}|\boldsymbol{u}^r\rangle$, we examine the deviatoric and isotropic contributions of the production tensor, $P_{ij} = P_{ij}^d - 2/3\tau_{kk}S_{ij}$, where $P_{ij}^d = -[\tau_{ik}^d\left(\partial u_j^r/\partial x_k\right) + \tau_{jk}^d\left(\partial u_i^r/\partial x_k\right)]$ and S_{ij} is the resolvable-scale strain rate. Here, $\langle P_{ij}^d|\boldsymbol{u}^r\rangle$ represents conditional production due to the interaction between the deviatoric part of the SGS stress and the resolvable-scale velocity gradient (anisotropic production), while $\langle -2/3\tau_{kk}S_{ij}|\boldsymbol{u}^r\rangle$ represents conditional production due to the straining of the isotropic part of the SGS stress by the resolvable-scale strain rate (isotropic production). The normal components of the former ($P_{\alpha\alpha}^d$) transfer energy from the resolvable to the subgrid scales (i.e. spectral transfer), while those of the latter ($-2/3\tau_{kk}S_{\alpha\alpha}$) redistribute energy among the normal components of the SGS stress since $-2/3\tau_{kk}S_{ii} = 0$. The conditional mean production rates of the streamwise and vertical SGS stress components are shown in figures 3.6(a)-3.6(d); the spanwise production component has trends qualitatively similar to that of the streamwise component and therefore is not included. Figures 3.6(b) and 3.6(d) show that, for negative u_3^r fluctuations (downdrafts), $\langle -2/3\tau_{kk}S_{11}|\boldsymbol{u}^r\rangle$ (and $\langle -2/3\tau_{kk}S_{22}|\boldsymbol{u}^r\rangle$) are negative and $\langle -2/3\tau_{kk}S_{33}|\boldsymbol{u}^r\rangle$ is positive, indicating inter-component exchange ($\langle \tau_{11}|\boldsymbol{u}^r\rangle$ and $\langle \tau_{22}|\boldsymbol{u}^r\rangle$ losing energy to $\langle \tau_{33}|\boldsymbol{u}^r\rangle$); the conditional spectral transfer (figures 3.6(a) and 3.6(c)) is also weaker and negative for very intense downdrafts. However, because their magnitudes are relatively small, the effects of $\langle -2/3\tau_{kk}S_{\alpha\alpha}|\boldsymbol{u}^r\rangle$ and $\langle P_{\alpha\alpha}^d|\boldsymbol{u}^r\rangle$ on the SGS anisotropy are weak. For positive u_3^r fluctuations (updrafts), $\langle -2/3\tau_{kk}S_{11}|\boldsymbol{u}^r\rangle$ is positive and $\langle -2/3\tau_{kk}S_{33}|\boldsymbol{u}^r\rangle$ is negative, indicating conditional energy transfer from the vertical to the horizontal velocity components; the conditional spectral transfer is also positive and much larger for $\langle \tau_{11}|\boldsymbol{u}^r\rangle$, resulting in surface-layer anisotropy.

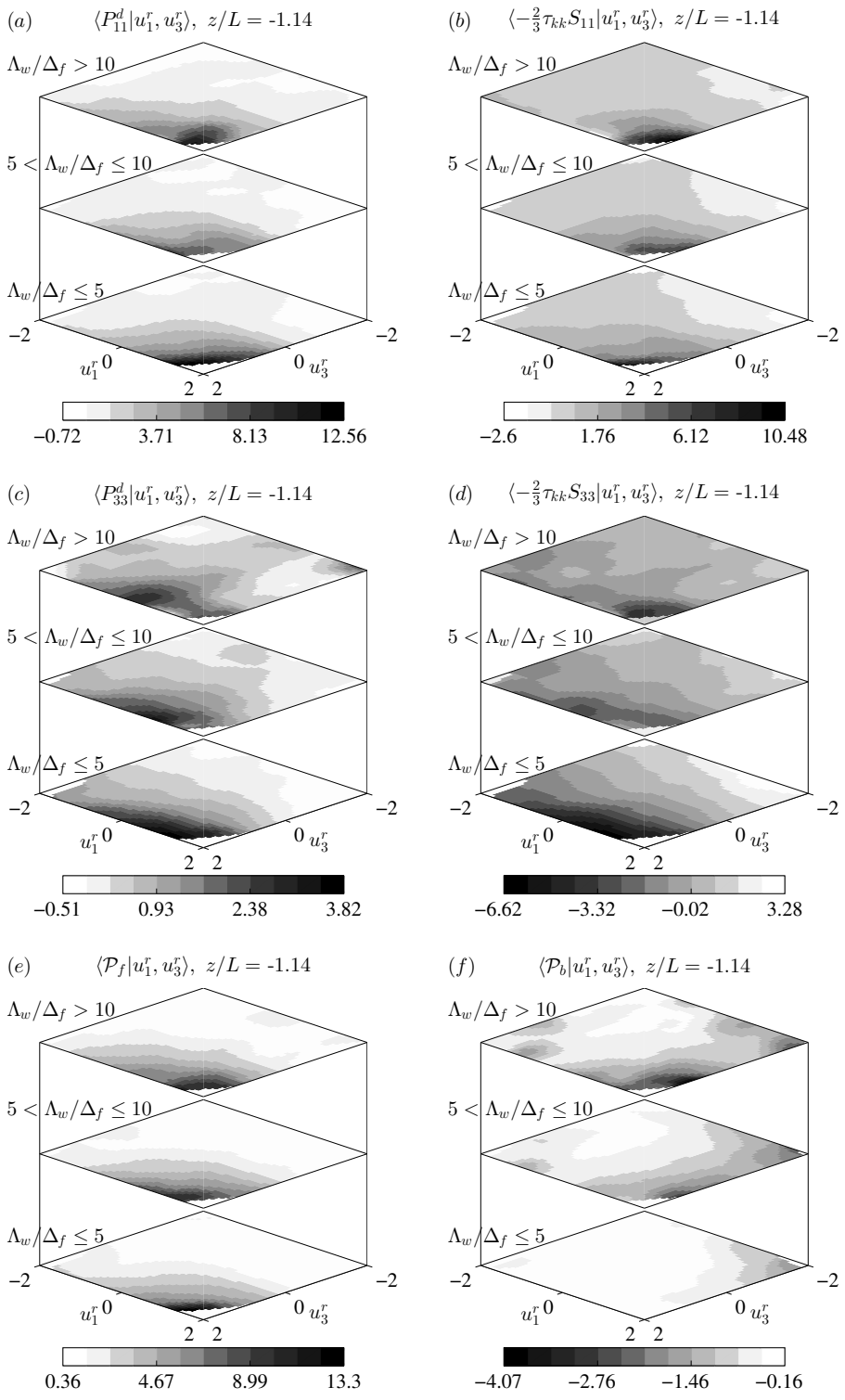

Figure 3.6: Conditional mean deviatoric and isotropic production of (a)-(b) $\langle \tau_{11} | \boldsymbol{u}^r \rangle$ and (c)-(d) $\langle \tau_{33} | \boldsymbol{u}^r \rangle$; and the conditional mean (e) forward and (f) backscatter contributions of SGS TKE.

The forward contribution to the conditional mean transfer, $\langle \mathcal{P}_f | \boldsymbol{u}^r \rangle$, and the backscatter contribution, $\langle \mathcal{P}_b | \boldsymbol{u}^r \rangle$, of SGS turbulent kinetic energy (TKE) are shown in figures 3.6(e) and 3.6(f), respectively; here, $\mathcal{P}_f = 1/2(\mathcal{P} + |\mathcal{P}|)$, $\mathcal{P}_b = 1/2(\mathcal{P} - |\mathcal{P}|)$, and $\mathcal{P} = \mathcal{P}_f + \mathcal{P}_b$ (Piomelli et al. 1996), where $\mathcal{P} = P_{kk}/2$ is the production rate of TKE. The results show strong conditional forward transfer ($\mathcal{P}_f > |\mathcal{P}_b|$) for positive u_3^r (and u_1^r) since the spectral transfer associated with the normal and shear strain rates is positive for updrafts, while for downdrafts there is conditional backscatter ($\mathcal{P}_f < |\mathcal{P}_b|$). The backscatter contribution to the conditional mean transfer increases with Λ_w/Δ_f (decreasing filter width), consistent with the observations of Sullivan et al. (2003) for the mean production. Similar to the conditional mean SGS stress, the conditional mean SGS production rate also has a non-diminishing dependence on the resolvable-scale velocity for all filter widths. Its magnitude is also non-diminishing, which is expected for the normal components of the production tensor since their sum is the spectral transfer rate, but suggests that $\langle P_{ij} | \boldsymbol{u}^r \rangle$ has a strong influence on the resolvable-scale velocity JPDF even for inertial-range filter widths.

3.3.2.2 *Conditional mean SGS pressure*

To aid our analysis of the conditional mean SGS pressure–strain-rate correlation, we present the results for the conditional mean SGS pressure, $\langle p - p^r | \boldsymbol{u}^r \rangle$, in figure 3.7 for the weakly and strongly convective surface layers. Due to the limited amount of pressure data available, the mean (weight-averaged) values of the stability parameter here differ from those of the conditional mean SGS production since the number of datasets is reduced. The results show that $\langle p - p^r | \boldsymbol{u}^r \rangle$ is strongly dependent on both the streamwise and vertical components of the resolvable-scale velocity. It is generally positive (negative) for negative (positive) u_3^r fluctuations, the former due to the deceleration of the mixed-layer eddies as they approach the ground. It also increases with u_1^r and its dependence on u_1^r is enhanced by negative u_3^r and weakened by positive u_3^r. In neutral boundary layers, such dependence has been attributed to the coherent structures generally found in turbulent boundary layer flows (Robinson 1991): Strong positive pressure fluctuations associated with negative u_3^r and positive u_1^r are due to large-scale sweeps of high-velocity fluid downward toward the wall, while strong negative pressure fluctuations associated with positive u_3^r and negative u_1^r are likely due to ejections of low-momentum fluid upward away from the wall.

In convective surface layers, the large convective eddies have dominant contributions to the horizontal velocity fluctuations, resulting in similar but stronger trends for negative u_3^r fluctu-

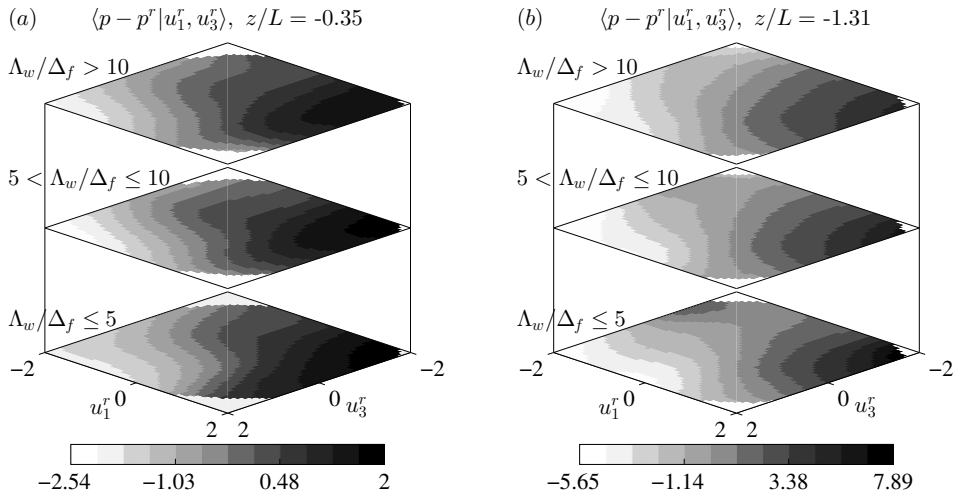

Figure 3.7: Conditional mean of the measured SGS pressure for the (a) weakly ($0 < -z/L \leq 0.75$) and (b) strongly convective ($0.75 < -z/L \leq 1.75$) surface layers.

ations. For positive u_3^r fluctuations, strong temperature fluctuations in thermal plumes generate low-pressure regions and hence negative values of $\langle p - p^r | \boldsymbol{u}^r \rangle$ near the surface, which are enhanced by negative u_1^r fluctuations (smaller u_1^r). The magnitude of $\langle p - p^r | \boldsymbol{u}^r \rangle$ increases with $-z/L$ since the characteristic length scales of the convective eddies increase with unstable stratification, resulting in a larger fluctuating pressure field and stronger pressure reflections from the image velocity field. Recall here that the convective atmospheric surface layer is characterized by small regions of intense buoyancy-driven updrafts surrounded by broader regions of downdrafts caused by the large convective eddies of the size of the boundary layer depth (Kaimal et al. 1976; Lenschow and Stephens 1980; Wilczak and Tillman 1980; Khanna and Brasseur 1997). The trends of $\langle p - p^r | \boldsymbol{u}^r \rangle$ for the strongly convective surface layer are generally similar to those of the weakly convective ABL. For the former, the results show much stronger positive pressure fluctuations compared to negative pressure events, suggesting much stronger large-scale vertical eddy compression during downdrafts compared to relatively weaker eddy stretching during updrafts, therefore resulting in broader regions of coherent positive pressure fluctuations at the wall. As the filter width decreases, the dependence of the SGS pressure on u_3^r generally weakens since the smaller SGS eddies (those with length scales smaller than the measurement height) are less likely to be affected by the wall (Elliott 1972).

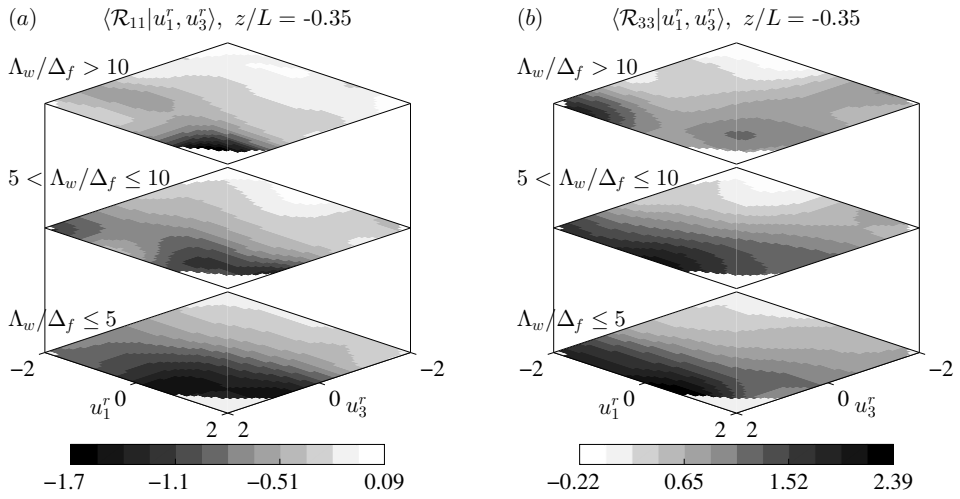

Figure 3.8: The (a) streamwise and (b) vertical components of the conditional mean SGS pressure–strain-rate correlation for the weakly convective ($0 < -z/L \leq 0.75$) surface layer.

3.3.2.3 *Conditional mean SGS pressure–strain-rate correlation*

The streamwise and vertical components of the conditional mean SGS pressure–strain-rate tensor, $\langle \mathcal{R}_{11}|\boldsymbol{u}^r\rangle$ and $\langle \mathcal{R}_{33}|\boldsymbol{u}^r\rangle$, are shown in figures 3.8 and 3.9. Nguyen et al. (2013) previously showed that, for weakly convective surface layers, the streamwise component of the mean SGS pressure–strain-rate tensor, $\langle \mathcal{R}_{11}\rangle$, is negative for all filter scales. This is expected since, for these surface layers, energy from the mean flow is fed to the subgrid scales through $\langle P_{11}\rangle$ and redistributed to $\langle \tau_{22}\rangle$ and $\langle \tau_{33}\rangle$ through $\langle \mathcal{R}_{ij}\rangle$. Figures 3.8(a) and 3.8(b) show $\langle \mathcal{R}_{11}|\boldsymbol{u}^r\rangle < 0$ and $\langle \mathcal{R}_{33}|\boldsymbol{u}^r\rangle > 0$ for most values of u_1^r and u_3^r, indicating conditional energy redistribution from the streamwise to the vertical velocity component through pressure-strain interaction. Recall that, for small values of $-z/L$, $\langle \tau_{11}|\boldsymbol{u}^r\rangle$ is much larger than $\langle \tau_{33}|\boldsymbol{u}^r\rangle$ and $\langle P_{11}|\boldsymbol{u}^r\rangle$ is much larger than $\langle P_{33}|\boldsymbol{u}^r\rangle$ and $\langle P_{B33}|\boldsymbol{u}^r\rangle$; therefore, the redistribution is consistent with return to isotropy. The weaker rate of pressure redistribution for negative u_3^r reflects the wall blocking effect (hereinafter, we use this term to refer to the restriction of the vertical-velocity fluctuations): During downdrafts, the wall blocking results in a reduction of the wall-normal SGS velocity component and the rate of redistribution. The pressure fluctuations reflecting from the wall (due to the image velocity field or the image Green's function), on the other hand, can enhance the rate of redistribution, as was alluded to by Hanjalić and Jakirlić (2002). The wall blocking effect, however, is likely to be stronger. Thus, for the weakly convective surface layer, the effect of the wall is to dampen the rate of conditional energy

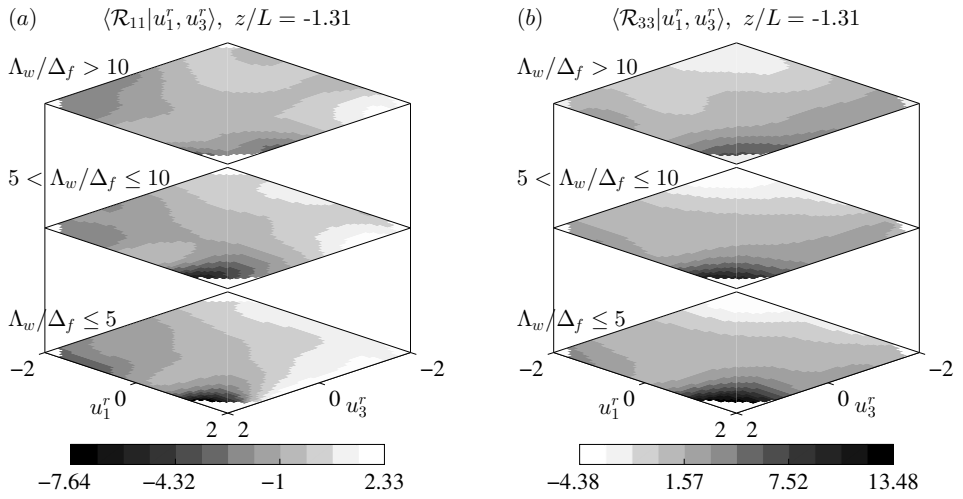

Figure 3.9: The (a) streamwise and (b) vertical components of the conditional mean SGS pressure–strain-rate correlation for the strongly convective ($0.75 < -z/L \leq 1.75$) surface layer.

redistribution from $\langle \tau_{11} | \boldsymbol{u}^r \rangle$ to $\langle \tau_{22} | \boldsymbol{u}^r \rangle$ and $\langle \tau_{33} | \boldsymbol{u}^r \rangle$ through $\langle \mathcal{R}_{ij} | \boldsymbol{u}^r \rangle$, therefore weakening the rate of return to isotropy. The magnitude of $\langle \mathcal{R}_{ij} | \boldsymbol{u}^r \rangle$ also decreases with increasing Λ_w/Δ_f due to the isotropization of the SGS stress with decreasing filter width.

For moderately and strongly convective surface layers, the results show that energy is also fed to $\langle \tau_{33} | u_i^r \rangle$ through buoyant production and pressure transport (§3.3.2.4). Nguyen et al. (2013) have shown that, for sufficiently convective surface layers, the mean pressure–strain-rate tensor $\langle \mathcal{R}_{ij} \rangle$ has a non-monotonic dependence on the filter width: While return to isotropy dominates for small filter widths, $\langle \mathcal{R}_{ij} \rangle$ causes SGS anisotropy for large filter widths. For these surface layers, figure 3.9 shows that $\langle \mathcal{R}_{11} | \boldsymbol{u}^r \rangle$ and $\langle \mathcal{R}_{33} | \boldsymbol{u}^r \rangle$ are negatively and positively correlated with u_3^r, respectively, and that their magnitudes generally increase with $|u_3^r|$. For positive u_3^r fluctuations (updrafts), $\langle \mathcal{R}_{11} | \boldsymbol{u}^r \rangle$ is negative and $\langle \mathcal{R}_{33} | \boldsymbol{u}^r \rangle$ positive, indicating conditional energy redistribution from $\langle \tau_{11} | \boldsymbol{u}^r \rangle$ to $\langle \tau_{33} | \boldsymbol{u}^r \rangle$ through pressure–strain-rate interaction. The rate of this inter-component exchange increases with (positive) u_3^r owing to stronger vertical stretching of the integral-scale eddies, resulting in a larger conditional energy transfer rate from the horizontal to the vertical velocity component.

For negative u_3^r fluctuations, $\langle \mathcal{R}_{11} | \boldsymbol{u}^r \rangle$ is positive and $\langle \mathcal{R}_{33} | \boldsymbol{u}^r \rangle$ is negative (for negative u_1^r), indicating conditional energy redistribution from $\langle \tau_{33} | \boldsymbol{u}^r \rangle$ to $\langle \tau_{11} | \boldsymbol{u}^r \rangle$ (although there are some positive values of $\langle \mathcal{R}_{33} | \boldsymbol{u}^r \rangle$ for positive u_1^r, which are likely due to the one-sided finite-difference approximation of the vertical derivative). The results thus show that $\langle \mathcal{R}_{ij} | \boldsymbol{u}^r \rangle$ generates anisotropy

due to the near-wall positive SGS pressure fluctuations found in the stagnation region within downdrafts. We note that if the updrafts were identical to downdrafts (but with reversed velocity), the stagnation region would also contain positive SGS pressure fluctuations and the contributions to $\langle \mathcal{R}_{\alpha\alpha} \rangle$ from both updrafts and downdrafts would cancel each other. The negative values of $\langle \mathcal{R}_{33} \rangle$ and positive values of $\langle \mathcal{R}_{11} \rangle$ (and $\langle \mathcal{R}_{22} \rangle$) are therefore primarily a consequence of the updrafts and downdrafts being asymmetric. The role played by the wall blocking effect within this mechanism is to impede the vertical-velocity fluctuations, thus enhancing anisotropy. In the meantime, the pressure reflected from the surface acts to augment the pressure fluctuations and therefore is likely to enhance anisotropy (but unlikely to be the main cause of it). Thus, unlike the weakly convective (shear-dominated) surface layer, where the wall blocking and pressure reflections have the opposite effects, here both act to enhance anisotropy. The contribution from the downward flow dominates the evolution of the (unconditional) mean SGS stress and therefore causes generation of anisotropy through the mean SGS pressure–strain-rate correlation, as was previously alluded to by Nguyen et al. (2013).

The above-mentioned effects are, moreover, enhanced by convective instability (since buoyancy is more dominant, and therefore the convective eddies are more energetic) and weakened as the filter width decreases since the wall contribution diminishes for very small filter widths and the effects of return to isotropy, although also weakening in absolute terms, becomes relatively more important (Nguyen et al. 2013). For very small filter widths ($\Lambda_w/\Delta_f > 10$), there is an eventual reversal of the direction of energy exchange ($\langle \tau_{33} | u_i^r \rangle$ now receiving from $\langle \tau_{11} | u_i^r \rangle$, regardless of the value of u_3^r) and the role of $\langle \mathcal{R}_{ij} | \boldsymbol{u}^r \rangle$ for these filter widths is similar to that for the weakly convective surface layer (i.e. return to isotropy).

The dependence of $\langle \mathcal{R}_{22} | \boldsymbol{u}^r \rangle$ on u_3^r is less apparent due to larger scatter in the computed statistics and therefore is not shown here. However, our previous analysis of $\langle \mathcal{R}_{22} \rangle$ has shown that the spanwise component of the mean pressure–strain-rate correlation is qualitatively similar to that of the vertical component for the weakly convective surface layer ($\langle \tau_{22} \rangle$ receiving energy from $\langle \tau_{11} \rangle$) and to that of the streamwise component for moderately and strongly convective surface layers ($\langle \tau_{22} \rangle$ receiving energy from $\langle \tau_{33} \rangle$). Similarly, based on the budgets of $\langle \tau_{11} | \boldsymbol{u}^r \rangle$ and $\langle \tau_{33} | \boldsymbol{u}^r \rangle$, we can infer that the behaviour of $\langle \mathcal{R}_{22} | \boldsymbol{u}^r \rangle$ is probably similar to that of $\langle \mathcal{R}_{33} | \boldsymbol{u}^r \rangle$ for the near-neutral surface layer (conditional energy redistribution from $\langle \tau_{11} | \boldsymbol{u}^r \rangle$ to $\langle \tau_{22} | \boldsymbol{u}^r \rangle$). For strongly convective surface layers, its behaviour is likely to be similar to that of $\langle \mathcal{R}_{11} | \boldsymbol{u}^r \rangle$.

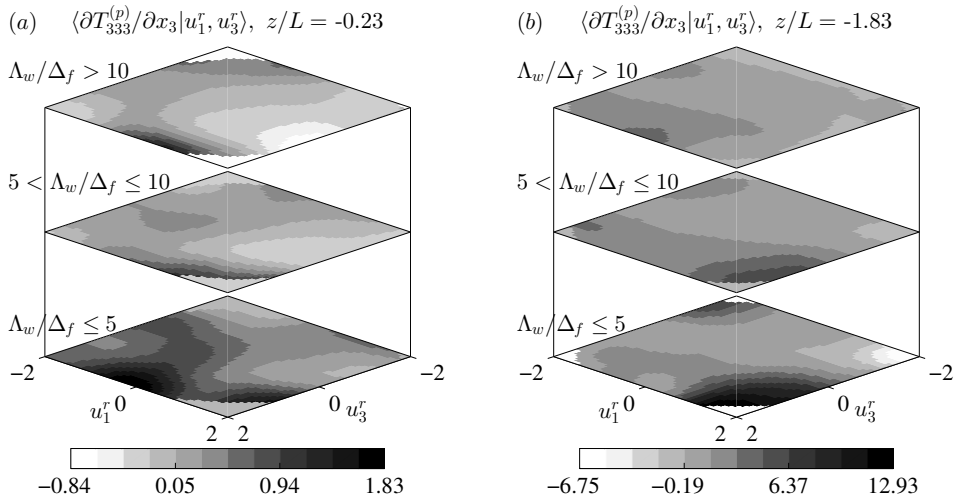

Figure 3.10: Conditional mean SGS pressure transport of $\langle \tau_{33} | \boldsymbol{u}^r \rangle$ for the (a) weakly ($0 < -z/L \leq 0.3$) and (b) strongly convective ($1 < -z/L \leq 2.5$) surface layers.

3.3.2.4 *Conditional mean SGS pressure transport*

Previous analyses of the (unconditional) mean SGS stress by Nguyen et al. (2013) showed that the SGS pressure transport is a major source of energy in the budget of $\langle \tau_{33} \rangle$ (and, therefore, a major source of energy in the budget of the mean SGS turbulent kinetic energy), with magnitudes comparable to those inferred in the literature (Wyngaard and Coté 1971; McBean and Elliott 1975; Bradley et al. 1981; Wilczak and Businger 1984). The results for the conditional mean SGS pressure transport, $\langle \partial T^{(p)}_{333}/\partial x_3 | \boldsymbol{u}^r \rangle$, shown in figure 3.10, however, indicate that it can be both a source and a sink of energy in the evolution of $\langle \tau_{33} | \boldsymbol{u}^r \rangle$. It is generally small for weakly convective surface layers (figure 3.10(a)), except for large filter widths, for which it is a gain and generally increases with u^r_3. For strongly convective surface layers (figure 3.10(b)) and large filter widths, $\langle \partial T^{(p)}_{333}/\partial x_3 | \boldsymbol{u}^r \rangle$ is the dominant source of energy for $\langle \tau_{33} | \boldsymbol{u}^r \rangle$ for positive u^r_3 (since energy is imported downward from higher z by pressure work) and a small loss for negative u^r_3. For small filter widths, the pressure transport is generally weak for negative u^r_3 and a gain for positive u^r_3, depending weakly on u^r_1. The results for positive u^r_3 fluctuations suggest that the conditional mean pressure transport may be driven by the negative local pressure minima which follow large-scale updrafts (figure 3.7). The physics associated with negative SGS pressure transport for negative u^r_3 fluctuations, however, is unclear and warrants further study.

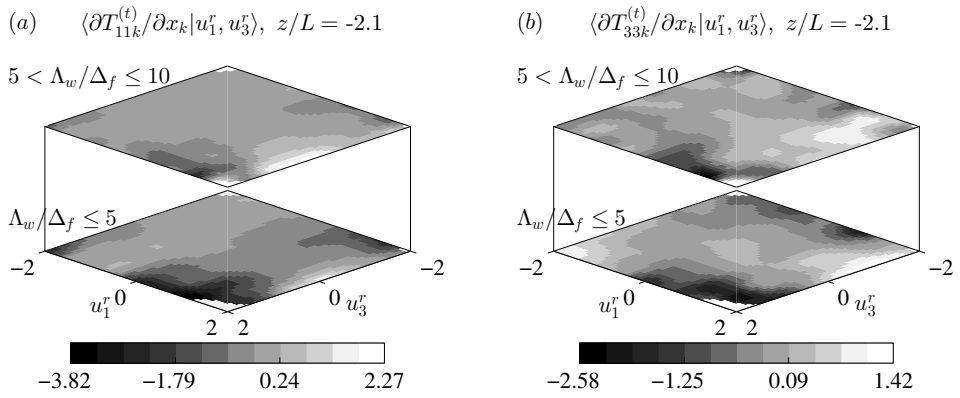

Figure 3.11: Conditional mean SGS turbulent transport of (a) $\langle \tau_{11} | \boldsymbol{u}^r \rangle$ and (b) $\langle \tau_{33} | \boldsymbol{u}^r \rangle$ for the strongly convective ($1.5 < -z/L \leq 2.5$) surface layer.

3.3.2.5 *Conditional mean SGS turbulent transport*

The conditional mean turbulent transport of $\langle \tau_{11} | \boldsymbol{u}^r \rangle$ and $\langle \tau_{33} | \boldsymbol{u}^r \rangle$, shown in figure 3.11 for the strongly convective surface layer, is generally negative for positive u^r_3 fluctuations, indicating upward transport of turbulent kinetic energy. It is small for negative u^r_3 fluctuations. Its magnitude generally decreases with the filter width and increases with $-z/L$ due to the stronger thermal plumes which are characteristic of the highly convective surface layer. The results also show that the magnitude and dependence of $\langle \partial T^{(t)}_{11k}/\partial x_k | \boldsymbol{u}^r \rangle$ on $\boldsymbol{u}^r$ are generally similar to those of $\langle \partial T^{(t)}_{33k}/\partial x_k | \boldsymbol{u}^r \rangle$, indicating that the conditional mean turbulent transport is nearly isotropic and therefore has a weak influence on the anisotropy of the conditional mean SGS stress. Its magnitude is also relatively small compared to the other budget terms, therefore making $\langle \partial T^{(t)}_{\alpha\alpha k}/\partial x_k | \boldsymbol{u}^r \rangle$ a relatively minor source of SGS energy. We note that the mean (weight-averaged) values of the stability parameter in figure 3.11 are slightly higher than those for the previous figures since calculation of the turbulent transport requires data from the upwind sonic anemometer array (for the streamwise derivative) and therefore reduces the number of usable datasets (from 26 to 18) since we require that both the upwind- and downwind-array measurements meet quality thresholds.

3.3.2.6 *Advection of the conditional mean SGS stress*

The vertical advection of $\langle \tau_{11} | \boldsymbol{u}^r \rangle$ and $\langle \tau_{33} | \boldsymbol{u}^r \rangle$ in physical space, shown in figure 3.12, is a major source (for negative u^r_3) and sink (for positive u^r_3) of energy in the budgets of the conditional mean SGS stress. For negative u^r_3 fluctuations, both $-v_3 \partial \langle \tau_{11} | \boldsymbol{u}^r \rangle / \partial x_3$ and $-v_3 \partial \langle \tau_{33} | \boldsymbol{u}^r \rangle / \partial x_3$ are

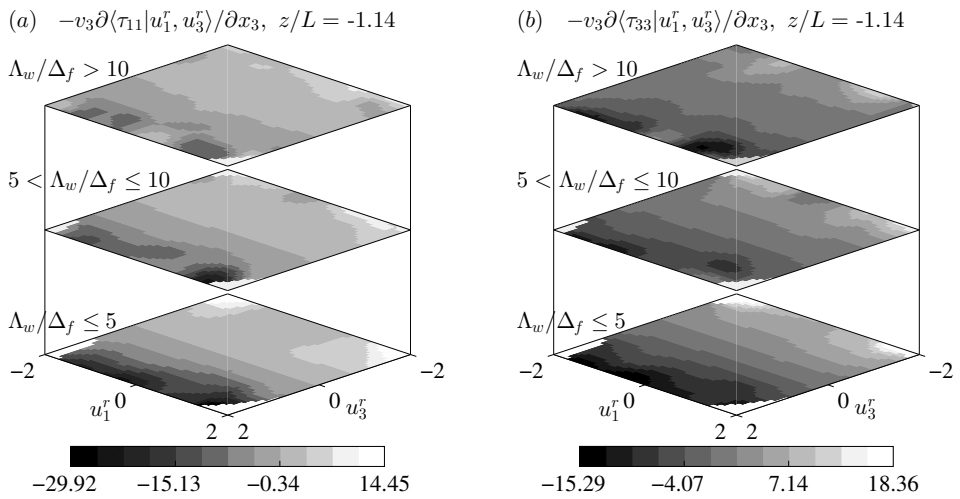

Figure 3.12: Vertical advection of (a) $\langle\tau_{11}|\boldsymbol{u}^r\rangle$ and (b) $\langle\tau_{33}|\boldsymbol{u}^r\rangle$ for the strongly convective ($0.8 < -z/L \le 1.5$) surface layer.

positive, indicating gains by $\langle\tau_{11}|\boldsymbol{u}^r\rangle$ and $\langle\tau_{33}|\boldsymbol{u}^r\rangle$ due to downward advection of SGS turbulent kinetic energy. For positive u_3^r fluctuations, the advection terms are negative, indicating losses by $\langle\tau_{11}|\boldsymbol{u}^r\rangle$ and $\langle\tau_{33}|\boldsymbol{u}^r\rangle$ due to upward advection of SGS energy. The energy loss due to upward advection is comparable in magnitude to the conditional mean shear production (for $\langle\tau_{11}|\boldsymbol{u}^r\rangle$) and the conditional mean pressure transport (for $\langle\tau_{33}|\boldsymbol{u}^r\rangle$), both of which are the major budget gains during updrafts. However, because it has similar effects on both $\langle\tau_{11}|\boldsymbol{u}^r\rangle$ and $\langle\tau_{33}|\boldsymbol{u}^r\rangle$, $-v_3\partial\langle\tau_{\alpha\alpha}|\boldsymbol{u}^r\rangle/\partial x_3$ does not contribute significantly to the SGS anisotropy. Advection of the conditional mean SGS stress in velocity space due to the resolvable-scale acceleration (second term in (3.1); not shown) is negligible, while the remaining budget term representing the covariance of the conditional mean fluctuations of the SGS stress and the conditional mean resolvable-scale acceleration is prohibitively difficult to compute and therefore omitted here.

3.3.2.7 *Conditional mean SGS shear stress budget*

Similar to $\langle\tau_{13}\rangle$, the evolution of $\langle\tau_{13}|\boldsymbol{u}^r\rangle$ is dominated by the conditional mean shear production, buoyant production, and velocity–pressure-gradient correlation. The conditional mean turbulent transport is small, while viscous dissipation is negligible due to local isotropy. The total production rate of $\langle\tau_{13}|\boldsymbol{u}^r\rangle$, $\langle P_{13} + P_{B13}|\boldsymbol{u}^r\rangle$, is shown in figure 3.13. (Although production of $\langle\tau_{13}|\boldsymbol{u}^r\rangle$ due to shear exceeds production due to buoyancy, both $\langle P_{13}|\boldsymbol{u}^r\rangle$ and $\langle P_{B13}|\boldsymbol{u}^r\rangle$ follow the

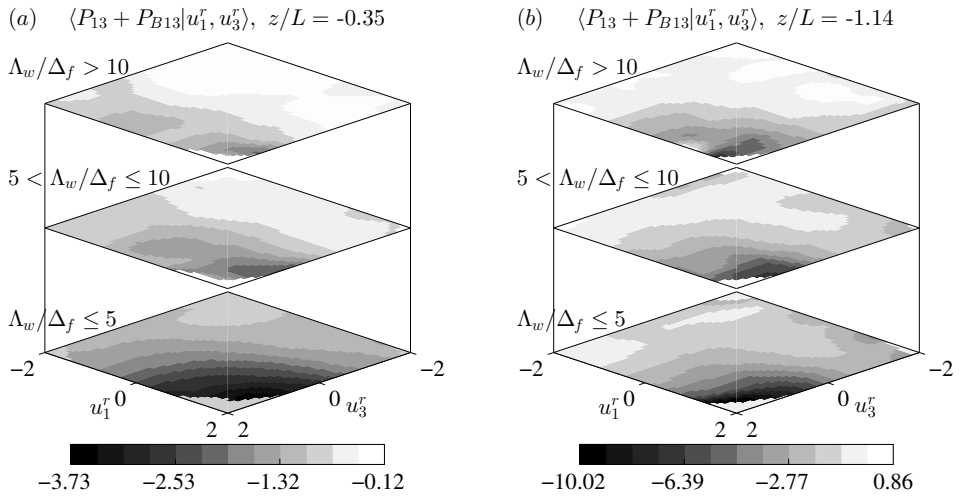

Figure 3.13: Sum of the conditional mean shear production and conditional mean buoyant production rates of $\langle \tau_{13} | \boldsymbol{u}^r \rangle$ for the (a) weakly ($0 < -z/L \leq 0.8$) and (b) strongly convective ($0.8 < -z/L \leq 1.5$) surface layers.

trends shown in figure 3.13.) The results show that $\langle P_{13} + P_{B13} | \boldsymbol{u}^r \rangle$ is negative, indicating production of $\langle \tau_{13} | \boldsymbol{u}^r \rangle$ since the shear stress is negative. Its magnitude generally increases with $\boldsymbol{u}^r$ and $-z/L$. The results for $\langle P_{13} | \boldsymbol{u}^r \rangle$ in terms of the contributions from the deviatoric and isotropic parts of the SGS stress (P_{13}^d and $-2/3\tau_{kk}S_{13}$, respectively; not shown) indicate that the former is positive, indicating destruction of the conditional mean SGS shear stress due to the straining and rotation of the anisotropic part of the SGS turbulence, while the latter is negative with nearly twice the magnitude, indicating production of $\langle \tau_{13} | \boldsymbol{u}^r \rangle$ due to the straining of the isotropic part of the SGS turbulence. Here, $\langle -2/3\tau_{kk}S_{13} | \boldsymbol{u}^r \rangle$ decreases in magnitude with increasing Λ_w/Δ_f (decreasing filter width) as the interaction between $\langle \tau_{kk} \rangle$ and the shear strain weaken, while $\langle P_{13}^d | \boldsymbol{u}^r \rangle$ also decreases with Λ_w/Δ_f since $\langle \tau_{ij} | \boldsymbol{u}^r \rangle$ is less anisotropic.

The conditional mean SGS velocity–pressure-gradient correlation, $\langle \Pi_{13} | \boldsymbol{u}^r \rangle$, which includes both the effects of the conditional mean pressure destruction and the conditional mean pressure transport of $\langle \tau_{13} | \boldsymbol{u}^r \rangle$, is shown in figure 3.14. The results show that $\langle \Pi_{13} | \boldsymbol{u}^r \rangle$ is positive for both weakly and strongly convective surface layers and all filter widths, indicating destruction of the conditional mean SGS shear stress. Similar to $\langle P_{13} | \boldsymbol{u}^r \rangle$ and $\langle P_{B13} | \boldsymbol{u}^r \rangle$, $\langle \Pi_{13} | \boldsymbol{u}^r \rangle$ increases in magnitude with u_1^r and u_3^r. Its dependence on u_i^r weakens with Λ_w/Δ_f since the resolvable-scale velocity has a diminishing effect on the smaller SGS eddies. The results for the conditional mean pressure–strain-rate correlation and the conditional mean pressure transport show that the former is dominant, with

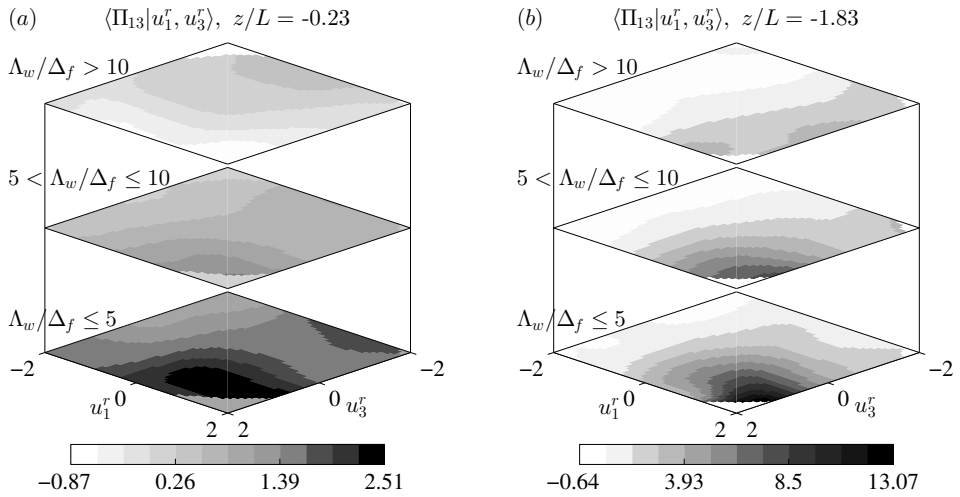

Figure 3.14: Conditional mean SGS velocity–pressure-gradient correlation in the transport equation of $\langle \tau_{13}|\boldsymbol{u}^r\rangle$ for the (a) weakly ($0 < -z/L \leq 0.75$) and (b) strongly convective ($1.75 < -z/L \leq 2.5$) surface layers.

trends similar to $\langle \Pi_{13}|\boldsymbol{u}^r\rangle$. We note that the trends and magnitude of $\langle \Pi_{13}|\boldsymbol{u}^r\rangle$ generally counter those of the conditional mean shear and buoyant production for both weakly and strongly convective surface layers and all filter widths, indicating that the conditional mean velocity–pressure-gradient correlation plays the usual role of causing return to isotropy in the evolution of $\langle \tau_{13}|\boldsymbol{u}^r\rangle$. The weaker rate of pressure destruction for negative u_3^r also indicates that the wall blocking effect merely dampens the rate of return to isotropy. The conditional mean advection (not shown) is positive (a sink) during updrafts and small during downdrafts, with magnitudes much smaller than the conditional mean production and pressure destruction.

3.3.3 Conditional mean SGS temperature flux budget

The conditional mean production rates of the horizontal and vertical components of the SGS potential temperature flux are shown in figures 3.15 and 3.16, respectively; we note that the non-dimensionalized flux production terms shown have the opposite signs relative to the actual flux production since $T_* < 0$ for unstable surface layers. The results show that $\langle P_{F1}|\theta^r\rangle$ is positive and $\langle P_{F3} + P_{BF3}|\theta^r\rangle$ is negative (indicating production of $\langle F_1|\theta^r\rangle$ and $\langle F_3|\theta^r\rangle$, respectively), both increasing in magnitude with θ^r. Although the production rate of $\langle F_3|\theta^r\rangle$ due to stratification ($\langle P_{F3}|\theta^r\rangle$) exceeds production due to buoyancy ($\langle P_{BF3}|\theta^r\rangle$) for the weakly convective surface layer, both generally follow the trends shown in figure 3.16. For positive θ^r fluctuations, the eddies

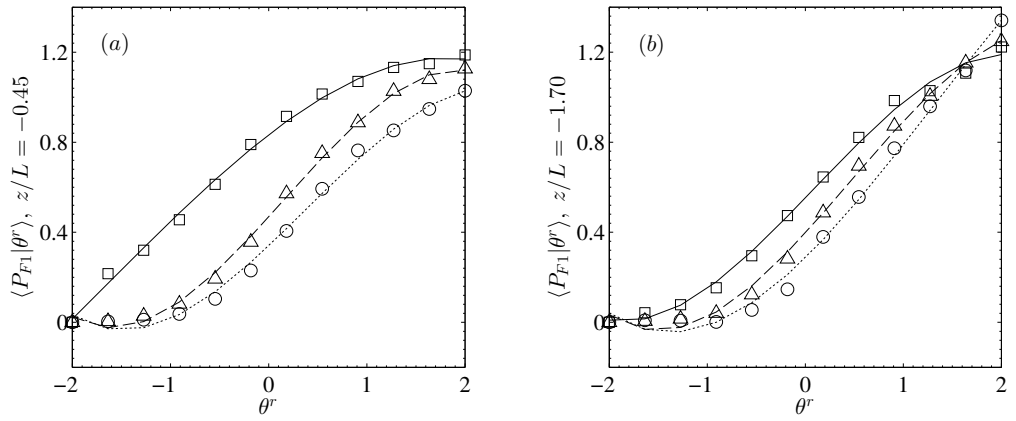

Figure 3.15: Conditional mean production of SGS horizontal temperature flux for the (a) weakly ($0 < -z/L \leq 1$) and (b) strongly convective ($1 < -z/L \leq 2.5$) surface layers and varying values of the wavelength–filter-width ratio: $\square$: $\Lambda_w/\Delta_f \leq 5$, $\triangle$: $5 < \Lambda_w/\Delta_f \leq 10$, $\bigcirc$: $\Lambda_w/\Delta_f > 10$.

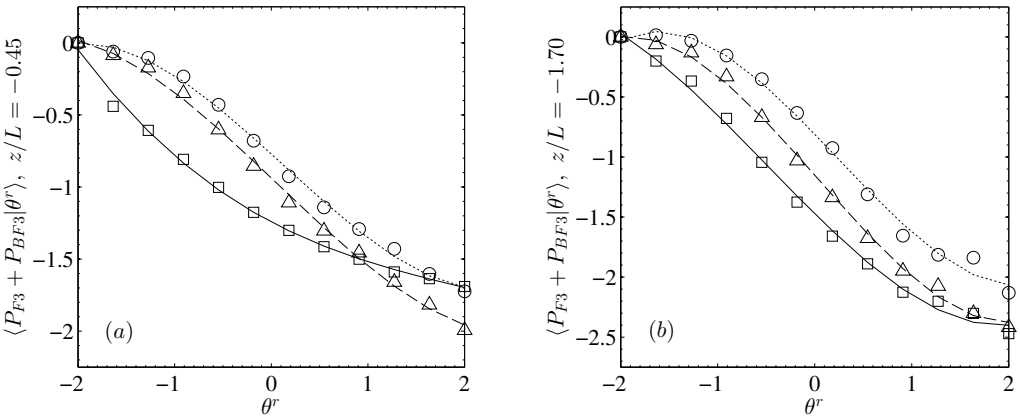

Figure 3.16: Conditional mean production of SGS vertical temperature flux for the (a) weakly ($0 < -z/L \leq 1$) and (b) strongly convective ($1 < -z/L \leq 2.5$) surface layers. The data are grouped as in figure 3.15.

associated with updrafts generally come from near the ground and therefore carry larger amounts of vertical SGS heat flux and SGS stress. They are also likely to have experienced stronger shear and vertical temperature gradient, both of which were shown to be the dominant contributions to $\langle P_{Fi} \rangle$ (Chen et al. 2010). For negative θ^r fluctuations, the eddies associated with downdrafts generally come from the mixed layer and carry relatively small amounts of SGS heat flux and SGS stress (buoyant production is also smaller); therefore, $\langle P_{Fi}|\theta^r \rangle$ (and $\langle P_{BF3}|\theta^r \rangle$) are smaller.

The magnitudes of $\langle P_{Fi}|\theta^r \rangle$ also decrease with increasing Λ_w/Δ_f because the SGS velocity and scalar are more isotropic for smaller filter widths (isotropy implies vanishing heat flux). For small filter widths, the dependence of $\langle P_{F1}|\theta^r \rangle$ on θ^r also weakens for negative temperature fluctuations (downdrafts) since the SGS flux carried by the returning downflow is likely to be well-mixed; this is less the case for positive temperature fluctuations (updrafts). As $-z/L$ increases, the conditional mean production rate of $\langle F_1|\theta^r \rangle$ decreases (for large filter widths) because the turbulence field is increasingly isotropic in the horizontal plane, resembling that of local free convection. The dependence of $\langle P_{F1}|\theta^r \rangle$ on z/L is weaker for larger values of Λ_w/Δ because, for these filter widths, the SGS flux is already quite isotropic (the effects of buoyancy are also weaker). Similar filter-width dependence is shown for $\langle P_{F3}|\theta^r \rangle$. As $-z/L$ increases, however, $\langle P_{F3}|\theta^r \rangle$, when non-dimensionalized using surface-layer scaling, should increase to a constant value since $\langle F_3|\theta^r \rangle$ is produced at a nearly constant rate in the free convection limit (Wyngaard et al. 1971). However, since $\langle P_{BF3}|\theta^r \rangle$ increases with $-z/L$, $\langle P_{F3} + P_{BF3}|\theta^r \rangle$ also increases slowly with $-z/L$.

The horizontal and vertical components of the conditional mean temperature–pressure-gradient correlation are shown in figures 3.17 and 3.18, respectively. Assuming nominal horizontal homogeneity of the field site, the pressure transport of $\langle F_1|\theta^r \rangle$ is small and hence $\langle \Pi_{F1}|\theta^r \rangle$ is dominated by the conditional mean SGS pressure–temperature-gradient correlation $\langle \mathcal{R}_{F1}|\theta^r \rangle$, which we show in place of $\langle \Pi_{F1}|\theta^r \rangle$. Figure 3.17 shows that $\langle \mathcal{R}_{F1}|\theta^r \rangle$ is negative for both weakly and strongly convective surface layers and all filter widths, indicating destruction of $\langle F_1|\theta^r \rangle$; its trends and magnitude generally balance those of $\langle P_{F1}|\theta^r \rangle$ (the advection and turbulent transport, not shown, are small). Similar to the flux production rate, its magnitude increases with increasing θ^r and Δ_f since the scalar field anisotropy increases with the vertical shear and filter scale. As Δ_f decreases, $\langle \mathcal{R}_{F1}|\theta^r \rangle$ weakens since the smaller SGS eddies are less anisotropic, therefore the tendency of $\langle \mathcal{R}_{F1}|\theta^r \rangle$ to drive the conditional mean flux towards isotropy weakens. It also decreases with increasing $-z/L$ since the scalar field is more horizontally isotropic as local free convection scaling is approached.

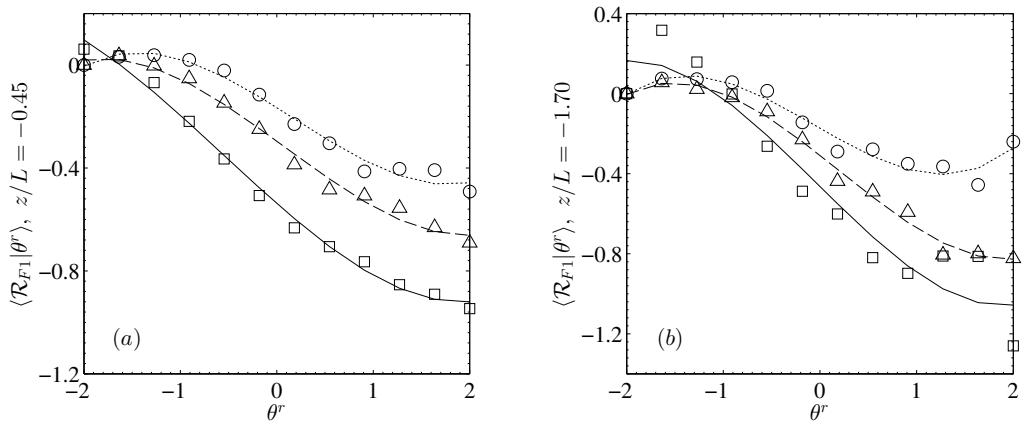

Figure 3.17: Conditional mean SGS pressure–temperature-gradient correlation in the budget of $\langle F_1|\theta^r\rangle$ for the (a) weakly ($0 < -z/L \leq 1$) and (b) strongly convective ($1 < -z/L \leq 2.5$) surface layers. The data are grouped as in figure 3.15.

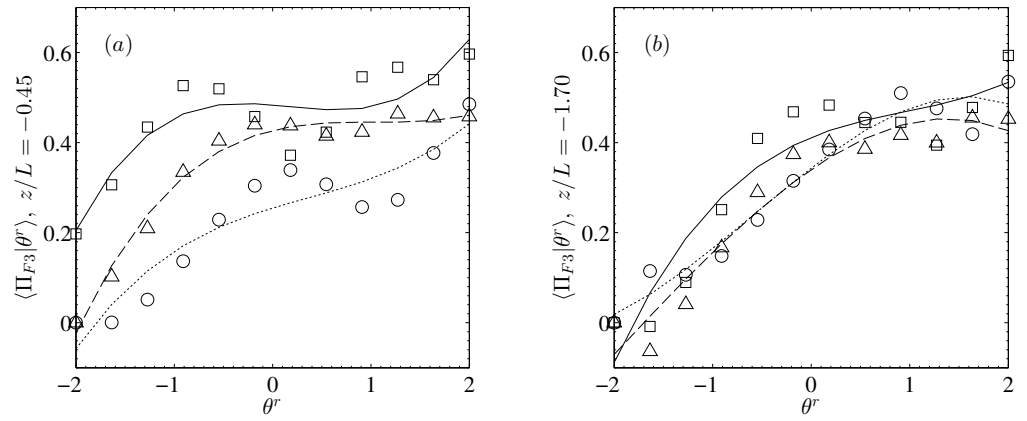

Figure 3.18: Conditional mean SGS temperature–pressure-gradient correlation in the budget of $\langle F_3|\theta^r\rangle$ for the (a) weakly ($0 < -z/L \leq 1$) and (b) strongly convective ($1 < -z/L \leq 2.5$) surface layers. The data are grouped as in figure 3.15.

Figure 3.18 shows that $\langle \Pi_{F3}|\theta^r\rangle$ (which includes the conditional mean SGS pressure transport and the conditional mean SGS pressure–temperature-gradient correlation) is positive for both weakly and strongly convective surface layers and all filter widths, indicating destruction of $\langle F_3|\theta^r\rangle$. Similar to the vertical SGS temperature flux production rate, its magnitude increases with increasing θ^r and decreases with decreasing filter width. It also increases asymptotically with $-z/L$ to a constant (local free convection) rate. Although the trends of $\langle \Pi_{F3}|\theta^r\rangle$ generally counter those of

$\langle P_{F3} + P_{BF3}|\theta^r\rangle$, its measured magnitude is considerably smaller than the total production rate, perhaps due to the attenuation of the fluctuating vertical pressure gradient by the finite difference scheme. Its trends, however, suggest that $\langle \Pi_{F3}|\theta^r\rangle$ plays the usual role of causing return to isotropy in the budget of $\langle F_3|\theta^r\rangle$.

3.3.4 Combined effects of the budget terms on the conditional mean SGS stress

The above results show that the budgets of the normal components of the conditional mean SGS stress are much more complex than those of the conditional mean SGS shear stress and SGS temperature flux, which are simply dominated by the conditional mean production and the pressure destruction. The budget of $\langle \tau_{11}|\boldsymbol{u}^r\rangle$ is dominated by the conditional mean production, the pressure–strain-rate correlation, and the turbulent transport; while that of $\langle \tau_{33}|\boldsymbol{u}^r\rangle$ also includes the conditional mean buoyant production and the pressure transport. To summarize the effects of the budget terms on the SGS stress structure, we show in figure 3.19 schematics of the conditional energy transfer during updrafts and downdrafts. A summary of the energy balance is given below.

When u_3^r (and u_1^r) are positive, $\langle \tau_{11}|\boldsymbol{u}^r\rangle$ receives large amounts of energy from the resolvable scales through the conditional mean shear production. Meanwhile, $\langle \tau_{33}|\boldsymbol{u}^r\rangle$ receives energy from the buoyant production, the pressure–strain-rate correlation, and the pressure transport, with the last term serving as the dominant source of SGS energy for positive u_3^r fluctuations. The conditional mean advection and, to a lesser extent, the conditional mean turbulent transport move much of this energy to higher z, while the pressure–strain-rate correlation redistributes relatively small amounts of energy from $\langle \tau_{11}|\boldsymbol{u}^r\rangle$ to $\langle \tau_{33}|\boldsymbol{u}^r\rangle$. The conditional redistribution part of the production tensor removes relatively small amounts of energy from $\langle \tau_{33}|\boldsymbol{u}^r\rangle$. Because the conditional mean advection has similar effects on both $\langle \tau_{11}|\boldsymbol{u}^r\rangle$ and $\langle \tau_{33}|\boldsymbol{u}^r\rangle$, it does not contribute significantly to the SGS anisotropy. However, due to the large gains by $\langle \tau_{11}|\boldsymbol{u}^r\rangle$ through shear production, the resulting SGS stress structure for positive u_3^r and u_1^r is anisotropic with one large eigenvalue. As u_1^r decreases, $\langle \tau_{ij}|\boldsymbol{u}^r\rangle$ remains anisotropic but transitions toward a one small eigenvalue structure since $\langle P_{11}|\boldsymbol{u}^r\rangle$ (although still larger than $\langle P_{33}|\boldsymbol{u}^r\rangle$) is relatively weaker (compared to its magnitude for positive u_1^r) and more comparable in magnitude to $\langle P_{22}|\boldsymbol{u}^r\rangle$.

When u_3^r is negative, the magnitudes of the budget terms are smaller due to generally

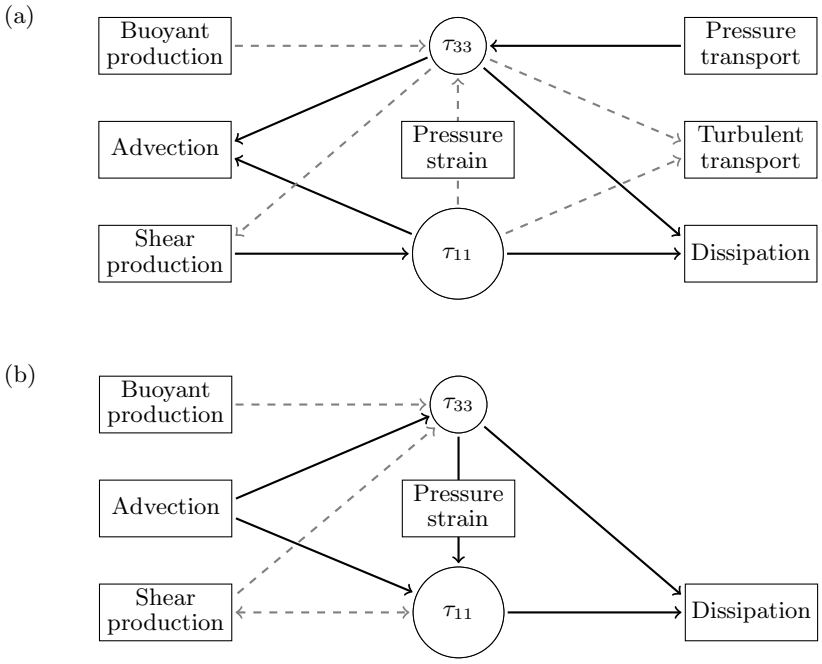

Figure 3.19: Schematics summarizing the conditional energy transfer during (a) updrafts and (b) downdrafts for the strongly convective surface layer and large filter widths. Solid and dashed arrows represent major and minor energy transfer (in relative magnitudes), respectively. The sizes of the circles containing τ_{11} and τ_{33} indicate their relative magnitudes. An arrow pointing towards (away from) a circle represents a source (sink). Because the pressure transport and turbulent transport are relatively weak and contain larger scatter for $u_3^r < 0$, we omit their contributions in (b).

weaker spectral transfer (and hence weaker production). Here, $\langle \tau_{11} | \boldsymbol{u}^r \rangle$ receives SGS energy from $\langle \tau_{33} | \boldsymbol{u}^r \rangle$ through the pressure–strain-rate correlation, contrary to return to isotropy. Meanwhile, both components receive a significant amount of energy through advection. Again, because the conditional mean advection has similar effects on both $\langle \tau_{11} | \boldsymbol{u}^r \rangle$ and $\langle \tau_{33} | \boldsymbol{u}^r \rangle$, it does not contribute significantly to the SGS anisotropy. Additionally, $\langle \tau_{11} | \boldsymbol{u}^r \rangle$ loses a small amount of energy to $\langle \tau_{33} | \boldsymbol{u}^r \rangle$ through the conditional redistribution part of the production tensor, while spectral transfer is small for both components (for very intense downdrafts, there is conditional backscatter). The conditional mean buoyant production, turbulent transport, and pressure transport are also weak, and therefore the magnitude of $\langle \tau_{33} | \boldsymbol{u}^r \rangle$ is smaller. Because both $\langle \tau_{11} | \boldsymbol{u}^r \rangle$ and $\langle \tau_{33} | \boldsymbol{u}^r \rangle$ and their budget terms are smaller, the conditional mean SGS stress is much less anisotropic for negative u_3^r.

The dominant SGS energy balance in the convective atmospheric surface layer is therefore as follows. Shear production and pressure transport provide energy (the former to $\langle \tau_{11} | \boldsymbol{u}^r \rangle$ and the latter to $\langle \tau_{33} | \boldsymbol{u}^r \rangle$) during updrafts. Advection, meanwhile, removes much of this energy to higher z. During downdrafts, energy is advected downward (from higher z) back to both components. At the same time, the pressure–strain-rate correlation redistributes the energy from $\langle \tau_{33} | \boldsymbol{u}^r \rangle$ to $\langle \tau_{11} | \boldsymbol{u}^r \rangle$ (which is relatively larger), causing strong SGS anisotropy. Dissipation, although not measured, is expected to be active and relatively isotropic. Using the current dataset, Nguyen et al. (2013) have shown that the budgets of the (unconditional) mean SGS stress and mean SGS temperature flux are approximately satisfied. In balancing the budgets of the normal components of the mean SGS stress, they approximated the mean dissipation rate using functional forms given in the literature (e.g. Caughey and Wyngaard 1979). In the present study, since the (conditional) dissipation rate was not measured, it is not possible to quantify the balance of the budgets of the normal components of the conditional mean SGS stress. However, for the conditional mean SGS shear stress (where dissipation is negligible due to local isotropy) and the conditional mean SGS temperature flux (where there is no dissipation), the conditional production is approximately balanced by the conditional pressure destruction (when their magnitudes are interpolated to comparable z/L), and therefore the budgets for these components appear to be satisfied. As stated previously, the imbalance of the vertical scalar flux budget may be due to the attenuation of the fluctuating vertical pressure gradient by the finite difference scheme.

3.4 Discussion and conclusions

Turbulence measurement data obtained in the convective atmospheric surface layer during the Advection Horizontal Array Turbulence Study were used to study the conditional mean SGS stress and the conditional mean SGS potential temperature flux. The AHATS field campaign notably includes measurements of the fluctuating pressure, therefore allowing for the budgets of the second-order SGS turbulence moments to be obtained. We showed that the terms which evolve the budgets of the conditional mean SGS stress and the conditional mean SGS temperature flux must be correctly predicted by the SGS model in order for LES to reproduce the resolvable-scale velocity JPDF and the resolvable-scale temperature PDF. We analysed the dependence of the budget terms on the surface-layer stability and filter width and showed that they are closely related to the dynamics of the convective atmospheric surface layer; more specifically, when conditioned on the resolvable-scale velocity, the budget terms show a strong dependence on the updrafts generated by buoyancy, downdrafts associated with the returning flow of convective eddies, and wall blocking effects. The results provide new insights into the SGS physics first educed in the previous study of the mean budget terms by Nguyen et al. (2013), particularly those involving the SGS pressure.

The present study shows that the budgets of the normal components of the conditional mean SGS stress are most complex for the strongly convective surface layer and large filter widths, where the conditional mean shear and buoyant production, advection in physical space, pressure transport, pressure–strain-rate interaction, and dissipation play an active role. During updrafts, the conditional mean shear production and the conditional mean pressure transport are the dominant sources of SGS energy (the former for $\langle \tau_{11} | \boldsymbol{u}^r \rangle$ and the latter for $\langle \tau_{33} | \boldsymbol{u}^r \rangle$), while the conditional mean advection and dissipation are the dominant sinks for both. During downdrafts, the conditional mean advection, which feeds back to $\langle \tau_{11} | \boldsymbol{u}^r \rangle$ and $\langle \tau_{33} | \boldsymbol{u}^r \rangle$ much of the energy taken from them during updrafts, is the dominant source for the latter. Much of the energy gained by $\langle \tau_{33} | \boldsymbol{u}^r \rangle$ from advection is transferred to $\langle \tau_{11} | \boldsymbol{u}^r \rangle$ by the conditional mean pressure–strain-rate correlation. Meanwhile, dissipation is a sink for both components. It is notable that the pressure transport is large only during updrafts, considering that much of the energy transfer from $\langle \tau_{33} | \boldsymbol{u}^r \rangle$ to $\langle \tau_{11} | \boldsymbol{u}^r \rangle$ through the pressure–strain-rate correlation occurs during downdrafts. The role played by the conditional mean advection is also notable given that advection of the (unconditional) mean SGS stress vanishes in a horizontally homogeneous atmospheric boundary layer.

The results for the conditional mean SGS pressure–strain-rate correlation show that the normal components of $\langle \mathcal{R}_{ij} | \boldsymbol{u}^r \rangle$ have more complex behaviours in strongly convective surface layers than in weakly convective ones due to the role played by strong updrafts, downdrafts, and wall effects. For weakly convective surface layers and large filter widths, much of the conditional energy transfer from the resolvable to the subgrid scales is first fed primarily to the streamwise velocity component and subsequently redistributed to the remaining (spanwise and vertical) components by the conditional mean pressure–strain-rate correlation, consistent with return to isotropy. For these surface layers, the role played by $\langle \mathcal{R}_{ij} | \boldsymbol{u}^r \rangle$ in the budget of the conditional mean SGS stress is similar to that of $\langle \mathcal{R}_{ij} \rangle$ in the budget of the (unconditional) mean SGS stress. For the former, we show that wall blockage of the vertical-velocity fluctuations during downdrafts dampens the rate of conditional energy redistribution. As the filter scale decreases, conditional mean production for the spanwise and vertical components becomes significant and the conditional mean SGS stress is likely to be more isotropic. Here, the role of $\langle \mathcal{R}_{ij} | \boldsymbol{u}^r \rangle$ diminishes, much like that of $\langle \mathcal{R}_{ij} \rangle$ in the budget of the mean SGS stress.

The behaviour of the conditional mean SGS pressure–strain-rate correlation for moderately and strongly convective surface layers is qualitatively different from that of the weakly convective surface layer. For these surface layers, $\langle \mathcal{R}_{ij} | \boldsymbol{u}^r \rangle$ redistributes energy from the (larger) horizontal to the (smaller) vertical velocity component during updrafts, likely due to stronger vertical stretching of the energy-containing eddies. During downdrafts, however, it redistributes SGS energy in the opposite direction (i.e. from the smaller vertical to the larger horizontal velocity components) and is the main cause of surface-layer SGS anisotropy, contrary to its commonly recognized role. The results also show that the conditional mean SGS pressure is generally positive for negative u_3^r and vice versa. Because of the asymmetry between the SGS pressure within updrafts and downdrafts, however, generation of SGS anisotropy is due to the positive SGS pressure fluctuations associated with the returning downflow of the convective eddies. The role played by the wall blocking effect and wall pressure reflection within this mechanism is to enhance the anisotropy, but the latter is unlikely to be the main cause of anisotropy. The results substantiate the importance of wall effects on the evolution of the (unconditional) mean SGS stress, for which the pressure–strain-rate correlation is the primary cause of anisotropy (Nguyen et al. 2013). These effects, however, weaken with decreasing filter width since the effects of the wall are reduced. For very small filter widths, the effects of return to isotropy become relatively more important and the role of $\langle \mathcal{R}_{ij} | \boldsymbol{u}^r \rangle$ is similar to that for the

weakly convective surface layer (i.e. causing return to isotropy).

In contrast, the role of the conditional mean SGS velocity–pressure-gradient correlation in the budget of the conditional mean SGS shear stress and that of the conditional mean SGS temperature–pressure-gradient correlation in the budget of the conditional mean SGS temperature flux are qualitatively similar for both weakly and strongly convective surface layers; that is, they act to counter the conditional mean production. The roles played by these terms are analogous to those of their unconditioned counterparts in the budgets of the mean SGS shear stress and mean SGS temperature flux.

The results also show that the pressure transport of turbulent kinetic energy is relatively small for weakly convective surface layers, while for strongly convective surface layers it can be both a source and a sink of SGS energy, depending strongly on the resolvable-scale vertical velocity. It is positive for positive u_3^r fluctuations and vice versa, the former suggesting that the import of turbulent kinetic energy into the surface layer by the pressure work is likely to be due to the negative local pressure minima which follow large-scale updrafts. The behaviour of the pressure transport for downdrafts, however, remains unclear and warrants further study.

The conditional analyses in the present work have important implications for SGS models, particularly models of the near-wall SGS pressure–strain-rate correlation. A common approach to modelling the pressure–strain-rate correlation in Reynolds-averaged Navier Stokes (RANS) parameterizations is to split the term into three parts (slow, rapid, and wall blocking (e.g. Pope 2000)) using the Green's function solution to the Poisson equation (Chou 1945) and to model each part separately. The slow and rapid parts promote energy redistribution as a means of reducing the anisotropy of the Reynolds stress and the Reynolds stress production tensors (e.g. Naot et al. 1970), respectively, whereas the wall blocking part dampens the rate of redistribution (e.g. Gibson and Launder 1978). The slow part is almost always modelled using Rotta's return-to-isotropy model (Rotta 1951). In the present study, the approximate balance between the SGS production and the SGS pressure destruction in the budgets of the conditional mean SGS shear stress and those of the conditional mean SGS heat flux for both weakly and strongly convective surface layers and all filter widths indicates that the pressure plays the expected role of causing return to isotropy, consistent with models for the slow and rapid pressure–strain-rate correlation. Similar behaviour for the normal components of $\langle \mathcal{R}_{ij} | \boldsymbol{u}^r \rangle$ for the weakly convective surface layer suggests that they can be modelled using conventional return-to-isotropy models, as is done in Ramachandran and Wyngaard (2011).

Smaller magnitudes of $\langle \mathcal{R}_{ij} | \boldsymbol{u}^r \rangle$ observed for negative u_3^r reflect the wall blocking effect, and can be properly modelled using existing wall damping models. These models, however, are unable to correctly predict the near-wall behaviour of the pressure–strain-rate correlation in the moderately and strongly convective surface layers, where the sign of $\langle \mathcal{R}_{ij} | \boldsymbol{u}^r \rangle$ is reversed during downdrafts. Because this effect is most significant for large filter widths, new models for both the Reynolds and SGS pressure–strain-rate correlation that can properly reflect the near-wall dynamics of the convective boundary layer, as revealed in the present study, are needed.

Chapter 4

Modelling of the subgrid-scale pressure–rate-of-strain: a scaling-based similarity approach

4.1 Introduction

In large-eddy simulation, the Navier-Stokes equations are spatially filtered to separate the large scales of the flow field from the small-scale motions. The large (or resolvable) scales are explicitly computed while the effects of the smaller (subgrid) scales are modelled. When the filter scale is in the inertial range, the role of the subgrid-scale model is to extract energy from the resolvable scales at the correct rate (Lilly 1967; Nieuwstadt and de Valk 1987; Domaradzki et al. 1993; Mason 1994; Borue and Orszag 1998; Wyngaard 2004). In LES of the atmospheric boundary layer, however, the smallest resolvable scales in the near-wall region are inevitably in the energy-containing range (Kaimal et al. 1972; Mason 1994; Peltier et al. 1996; Tong et al. 1998, 1999). As a result, a significant portion of the turbulent stress is carried by the subgrid scales, leading to strong dependence of the LES field on the SGS model, which must now represent the dynamics of the SGS stress tensor.

Developing improved SGS parameterizations requires incorporating additional physics, including history and non-local effects, into the SGS model. Transport-equation-based SGS modelling, which solves the full conservation equations for the SGS stress, is well-suited for this purpose and has

the potential to predict LES statistics with more accuracy (Deardorff 1972, 1973; Wyngaard 2004; Hatlee and Wyngaard 2007; Ramachandran 2010). Models for the terms in the SGS conservation equations are largely based on Reynolds stress second-moment closure models (Lumley 1983). Here, the production tensor is in closed form and dissipation is assumed to be isotropic. Turbulent transport is modelled using a gradient-diffusion model (or its transport equation, for buoyancy-driven flows). The pressure–velocity-gradient is decomposed into a transport term, which is often modelled along with turbulent transport, and a pressure–strain-rate correlation. Along with production and dissipation, the pressure–rate-of-strain is a dominant term in the Reynolds stress balance (Pope 2000; Launder and Sandham 2002), as well as in the near-wall SGS stress balance (Nguyen et al. 2013; Nguyen and Tong 2015), and therefore its modelling is crucial.

Insight into the pressure–rate-of-strain can be gained by examining the Poisson equation for the fluctuating pressure field,

$$\nabla^2 p' = -\frac{\partial^2}{\partial x_i \partial x_j}\left(u_i'u_j' - \langle u_i'u_j'\rangle\right) - 2\frac{\partial\langle u_i\rangle}{\partial x_j}\frac{\partial u_j'}{\partial x_i} - \frac{g}{\Theta}\frac{\partial\theta'}{\partial x_i}, \tag{4.1}$$

obtained by taking the divergence of the Navier-Stokes equations and subtracting its mean part, wherein p, u_i, Θ, θ, and g are the kinematic pressure, velocity, mean and fluctuating potential temperatures, and gravitational acceleration, respectively, with primes denoting fluctuations and angle brackets denoting an ensemble average. Equation (4.1) shows that pressure fluctuations are generated by three different source terms associated with the fluctuating velocity and temperature fields: a 'slow' component associated with turbulence-turbulence interactions, a 'rapid' component associated with mean shear interactions (so-called because it reacts instantly to imposed mean velocity gradients) and, for stratified flows, a buoyant component arising from density fluctuations. Integration of (4.1) using its Green's function solution (Chou 1945) yields the exact expression for the fluctuating pressure at $\boldsymbol{x}$ (e.g. Launder and Sandham 2002),

$$\begin{aligned} p' = {} & \underbrace{\frac{1}{4\pi}\int_V \frac{\partial^2}{\partial x_i \partial x_j}\left(u_i'u_j' - \langle u_i'u_j'\rangle\right)\frac{\mathrm{d}V(\boldsymbol{r})}{|\boldsymbol{r}-\boldsymbol{x}|}}_{p'^{(s)}} + \underbrace{\frac{1}{2\pi}\int_V \frac{\partial\langle u_i\rangle}{\partial x_j}\frac{\partial u_j'}{\partial x_i}\frac{\mathrm{d}V(\boldsymbol{r})}{|\boldsymbol{r}-\boldsymbol{x}|}}_{p'^{(r)}} \\ & + \underbrace{\frac{1}{4\pi}\int_V \frac{g}{\Theta}\frac{\partial\theta'}{\partial x_i}\frac{\mathrm{d}V(\boldsymbol{r})}{|\boldsymbol{r}-\boldsymbol{x}|}}_{p'^{(b)}} + \underbrace{\frac{1}{4\pi}\int_A \left[\frac{1}{|\boldsymbol{r}-\boldsymbol{x}|}\frac{\partial p'}{\partial n} - p'\frac{\partial}{\partial n}\left(\frac{1}{|\boldsymbol{r}-\boldsymbol{x}|}\right)\right]\mathrm{d}A(\boldsymbol{r})}_{p'^{(w)}}, \end{aligned} \tag{4.2}$$

wherein the volume and surface integrals are taken over all other points $\boldsymbol{r}$ (where the fluctuating velocity and pressure are given by $u_i'(\boldsymbol{r})$ and $p'(\boldsymbol{r})$, respectively). The resulting field is non-local and can be viewed as having two contributions: The first three volume integrals are free-space solutions to the Poisson equation, with $p'^{(s)}$, $p'^{(r)}$, and $p'^{(b)}$ denoting pressure fluctuations resulting from the slow, rapid, and buoyant source terms, respectively. The remaining surface integral, often called the 'wall' contribution, represents effects on the fluctuating pressure field due to the boundary conditions. For an infinite plane boundary, $p'^{(w)}$ can be related to pressure reflections from the wall using the method of images (Pope 2000).

Corresponding to $p'^{(s)}$, $p'^{(r)}$, $p'^{(b)}$, and $p'^{(w)}$, the Reynolds-stress pressure–strain-rate correlation can be expressed as the sum of a slow, rapid, buoyant, and wall component,

$$R_{ij} \equiv p' \left(\frac{\partial u_i'}{\partial x_j} + \frac{\partial u_j'}{\partial x_i} \right) = R_{ij}^{(s)} + R_{ij}^{(r)} + R_{ij}^{(b)} + R_{ij}^{(w)}, \tag{4.3}$$

where e.g. $R_{ij}^{(s)} \equiv p'^{(s)}(\partial u_i'/\partial x_j + \partial u_j'/\partial x_i)$. Note that $R_{\alpha\alpha}$ ($\alpha = 1, 2, 3$; no summation) acts to redistribute energy among the normal Reynolds stress components since $R_{kk} = 0$. Because they represent different physical processes, a common approach in Reynolds-averaged Navier-Stokes (RANS) parameterizations is to model each term in (4.3) separately (Pope 2000). The slow part is modelled as the linear return to isotropy of decaying homogeneous anisotropic turbulence, most often using Rotta's 'return to isotropy' model (Rotta 1951), though more elaborate forms have been proposed (e.g. Lumley 1978; Fu et al. 1987). While many closures also exist for the rapid part (e.g. Launder et al. 1975; Shih and Lumley 1985; Fu et al. 1987; Speziale et al. 1991), the commonly used 'isotropization of production' model assumes that the effect of the rapid pressure-strain is to reduce the shear production anisotropy (Naot et al. 1970). Similar closures can be derived for the buoyant part (e.g. Launder 1975; Gibson and Launder 1978). The remaining term ($R_{ij}^{(w)}$), significant only in the proximity of the boundary, represents pressure reflection and wall blocking effects. The former enhances near-wall pressure fluctuations, while the latter, which is more dominant, impedes the isotropization effects of the pressure fluctuations (Perot and Moin 1995; Launder and Sandham 2002). Several closures have been proposed for the wall contribution: Gibson and Launder (1978) model $R_{ij}^{(w)}$ using a local wall echo term which acts to dampen pressure redistribution. A more natural treatment of $R_{ij}^{(w)}$ proposed by Durbin (1991, 1993) provides the required damping through a (non-local) elliptic relaxation equation.

Closures for $R_{ij}^{(s)}$, $R_{ij}^{(r)}$, $R_{ij}^{(b)}$, and $R_{ij}^{(w)}$, though derived in the context of Reynolds-stress second-moment closure modelling, have natural extensions to transport-equation-based SGS modelling (Hatlee and Wyngaard 2007; Ramachandran 2010; Enriquez 2013), where the SGS pressure–rate-of-strain can be expressed as

$$\mathcal{R}_{ij} \equiv \left(p\frac{\partial u_i}{\partial x_j} + p\frac{\partial u_j}{\partial x_i} \right)^r - \left(p^r\frac{\partial u_i^r}{\partial x_j} + p^r\frac{\partial u_j^r}{\partial x_i} \right) = \mathcal{R}_{ij}^{(s)} + \mathcal{R}_{ij}^{(r)} + \mathcal{R}_{ij}^{(b)} + \mathcal{R}_{ij}^{(w)}, \tag{4.4}$$

with superscript r denoting a resolvable-scale variable. Recent field measurements by Nguyen et al. (2013) provide important insight into the dynamics of $\mathcal{R}_{ij}$. In the context of transport-equation-based modelling, their results show an approximate balance between the production and pressure destruction of SGS shear stress in both shear- and buoyancy-dominated ABL flows, consistent with return to isotropy models. Analyses of the conditional mean SGS budgets by Nguyen and Tong (2015) show that the rate of pressure destruction is stronger for updrafts and weaker during downdrafts, the latter attributed to the wall blocking effect (i.e. a reduction of the wall-normal velocity component) and therefore consistent with wall damping models. Similar return-to-isotropy behaviours were observed for the normal components of the SGS pressure–rate-of-strain in the near-neutral ABL. For unstable (convective) surface layers, however, $\mathcal{R}_{\alpha\alpha}$ are governed by two competing effects, return to isotropy and generation of anisotropy, the latter due to ground blockage of the large-scale convective eddies. Return to isotropy dominates for relatively small filter scales (i.e. well-resolved turbulence), whereas for large filter scales (poorly-resolved turbulence) the wall blocking effect dominates, resulting in strong SGS anisotropy. Thus, although models for the slow and rapid contributions to $\mathcal{R}_{\alpha\alpha}$ are capable of predicting return to isotropy, those for the wall contribution are likely to mis-predict generation of anisotropy, leading to under-prediction of the surface layer anisotropy. For convective boundary layers, these errors can propagate into the mixed layer and alter the flow structure there (e.g. Khanna and Brasseur 1998; Ludwig et al. 2009).

To develop improved transport-equation-based SGS parameterizations requires closures for the normal components of the SGS pressure–rate-of-strain which can properly predict the near-wall SGS dynamics. In the present work, we propose a generalised model for $\mathcal{R}_{\alpha\alpha}$ which includes both return-to-isotropy and generation-of-anisotropy contributions to the pressure-strain redistribution of SGS energy. The model is derived in §4.2 using basic scaling arguments. In §4.3, we perform *a priori* tests of the model using high-resolution LES data: mean profiles of the true and modelled

SGS pressure–rate-of-strain are presented in §4.3.1, while their conditional means are presented in §4.3.2. Discussion and conclusions are given in §4.4.

4.2 Model description

Different from previous closures, which separately model the effects of the slow, rapid, buoyant, and wall contributions to the pressure–rate-of-strain tensor, we seek to predict the normal (redistributive) components as the linear sum of two competing effects, an isotropization effect characteristic of the shear-dominated neutral surface layer and an anisotropization effect characteristic of the buoyancy-dominated convective one. Expressions for the neutral and convective contributions are obtained using scaling arguments, while their relative magnitudes are determined dynamically from the resolved scales.

For a horizontally homogeneous, quasi-stationary atmospheric surface layer driven by shear and modulated by buoyancy, the Monin-Obukhov similarity hypothesis (Obukhov 1946; Monin and Obukhov 1954; hereafter referred to as the M–O similarity) states that the pressure–strain-rate correlation (as is any other surface-layer statistic) is scaled by four parameters: z, u_*, β, and Q_0, where z is the distance from the ground, $u_* = (-\langle u_1' u_3' \rangle)^{1/2}$ is the friction velocity, $\beta = g/\Theta$ is the thermal expansion coefficient, and $Q_0 = \langle u_3' \theta' \rangle$ is the surface temperature flux. These parameters combine to form the nondimensional stability parameter z/L, where $L = -u_*^3/(\kappa \beta Q_0)$, in which κ is the von Kármán constant. According to the M–O similarity, the mean pressure–strain-rate, when scaled by the governing parameters, is a function only of z/L. Note that this functional dependence is only apt for cases where the shear and buoyant production rates of turbulence kinetic energy are comparable (Wyngaard 2010). In the free convection limit ($-z/L \to \infty$), Nguyen et al. (2014) show that the Reynolds-stress pressure–rate-of-strain instead follows mixed-layer similarity.

To model separately the effects of shear and buoyancy, we separate the normal components of the pressure–strain-rate into a neutral contribution and a convective contribution. For the Reynolds-stress pressure–strain-rate correlation, this reads

$$R_{\alpha\alpha} = R_{\alpha\alpha}^{(n)} + R_{\alpha\alpha}^{(c)}. \tag{4.5}$$

To form scales appropriate for the neutral contribution, $R_{\alpha\alpha}^{(n)}$, we examine the asymptotic behaviour

of the M–O similarity in the neutral surface layer ($-z/L \to 0$), where β and Q_0 are no longer relevant parameters. In this asymptotic state, the surface-layer statistics are characterised by a reduced set of governing parameters (Wyngaard 2010), which combine to form a single dimensionless group, which is constant and therefore independent of L. The characteristic length and velocity scales here are z and u_*, respectively; and the neutral contribution to the pressure–strain-rate correlation simply scales as $R_{\alpha\alpha}^{(n)} \sim u_*^3/z$.

To form scales appropriate for the convective contribution, we use mixed-layer similarity (Willis and Deardorff 1974), where (as $-z/L \to \infty$) the shear production rate of turbulence kinetic energy vanishes and therefore u_* is no longer a relevant scaling parameter. Here, the characteristic velocity is given by the convective velocity scale $w_* = (\beta Q_0 z_i)^{1/3}$ (Wyngaard et al. 1971), defined in terms of the boundary layer depth z_i. The convective contribution to the pressure–strain-rate thus scales as $R_{\alpha\alpha}^{(c)} \sim w_*^3/z_i = \beta Q_0$. In this local free convective state, $R_{\alpha\alpha}^{(c)}$ also depends on secondary scales that are non-local to the surface layer (Willis and Deardorff 1974; Bradshaw 1978). The most significant of these is the near-ground sweeping motion of the mixed-layer eddies, which scale with $z_i \sim \mathcal{O}(1\text{ km})$. To account for contributions of this size, we include a functional dependence on the nondimensional height z/z_i in the scaling of $R_{\alpha\alpha}^{(c)}$. Combining expressions for $R_{\alpha\alpha}^{(n)}$ and $R_{\alpha\alpha}^{(c)}$, the Reynolds-stress pressure–strain-rate thus scales as

$$R_{\alpha\alpha} = R_{\alpha\alpha}^{(n)} + R_{\alpha\alpha}^{(c)} \sim \frac{u_*^3}{z} + \beta Q_0 G_\alpha \left(\frac{z}{z_i}\right). \tag{4.6}$$

The functional form of $G_\alpha\,(z/z_i)$, needed to predict the normal components of the Reynolds-stress pressure–rate-of-strain, is discussed in §4.4.

Similar to (4.5) and (4.6), we now separate the normal components of the SGS pressure–strain-rate into a neutral contribution and a convective contribution,

$$\mathcal{R}_{\alpha\alpha} = \mathcal{R}_{\alpha\alpha}^{(n)} + \mathcal{R}_{\alpha\alpha}^{(c)}, \tag{4.7}$$

where, by the same scaling arguments, $\mathcal{R}_{\alpha\alpha}^{(n)} \sim u_*^3/z$ and $\mathcal{R}_{\alpha\alpha}^{(c)} \sim u_f^3/z = \beta Q_0$. For the SGS pressure–strain-rate correlation, however, the influence of z/z_i is secondary to z/Δ since the largest SGS eddies are bounded by the LES filter width Δ. This functional dependence now also appears in the scaling of $\mathcal{R}_{\alpha\alpha}^{(n)}$ since $z \sim \Delta$ (whereas, for the Reynolds stress, $z \ll z_i$ and therefore any functional of z/z_i

is approximately constant). The SGS pressure–rate-of-strain thus scales as

$$\mathcal{R}_{\alpha\alpha} = \mathcal{R}_{\alpha\alpha}^{(n)} + \mathcal{R}_{\alpha\alpha}^{(c)} \sim \frac{u_*^3}{z} f_\alpha\left(\frac{z}{\Delta}\right) + \beta Q_0 g_\alpha\left(\frac{z}{\Delta}\right). \tag{4.8}$$

We take (4.8) as a model for $\mathcal{R}_{\alpha\alpha}$, and note that the functions $f_\alpha(z/\Delta)$ and $g_\alpha(z/\Delta)$ are constant if their argument z/Δ, the ratio of the wall-normal distance (a measure of the integral length scale of the vertical velocity) to the filter width, is constant. The model thus assumes that the SGS pressure–rate-of-strain is scale invariant. For constant values of z/Δ, its convective contribution depends only on the thermal expansion coefficient and surface heat flux, while its neutral contribution depends on the friction velocity scaled by z. Scale invariance of (4.8), however, is an implicit result of the scaling approach, rather than the explicit assumption of scale similarity (as in e.g. Bardina et al. 1980; Meneveau and Katz 2000). We therefore term (4.8) the scaling-based similarity model.

The transport-equation-based SGS modelling approach requires solving an additional nine equations for the SGS fluxes. For the remainder of this section, we briefly outline the implementation of (4.8) within this framework. For discussions on the general implementation of the transport-equation-based SGS model, we refer the reader to Ramachandran (2010) and Ramachandran and Wyngaard (2011), who implement a truncated version of the SGS conservation equations using Rotta's model. For the scaling-based similarity model, at height z_1 (e.g. the first LES grid point) (4.8) reads

$$\mathcal{R}_{\alpha\alpha}^{\mathrm{M}}(z_1) = \frac{u_*^3}{z} f_\alpha\left(\frac{z_1}{\Delta_1}\right) + \beta Q_0 g_\alpha\left(\frac{z_1}{\Delta_1}\right), \tag{4.9}$$

where $\Delta_1 = (\Delta_x \Delta_y)^{1/2}$ is the horizontal LES grid spacing. The diagnostic variables β and Q_0 appearing in (4.9) are prescribed (Moeng 1984), while u_* is obtained in the LES using an iterative procedure (Khanna 1995; Otte and Wyngaard 2001). We determine the remaining model coefficients $f_\alpha(z_1/\Delta_1)$ and $g_\alpha(z_1/\Delta_1)$ using the dynamic procedure (Germano et al. 1991; Germano 1992) and the resolved fields at heights z_2 and z_3 as follows. At z_2 and z_3 (where $z_3 > z_2 > z_1$), (4.8) reads

$$\mathcal{R}_{\alpha\alpha}^{\mathrm{M}}(z_2) = \frac{u_*^3}{z_2} f_\alpha\left(\frac{z_2}{\Delta_2}\right) + \beta Q_0 g_\alpha\left(\frac{z_2}{\Delta_2}\right) \tag{4.10}$$

and

$$\mathcal{R}_{\alpha\alpha}^{\mathrm{M}}(z_3) = \frac{u_*^3}{z_3} f_\alpha\left(\frac{z_3}{\Delta_3}\right) + \beta Q_0 g_\alpha\left(\frac{z_3}{\Delta_3}\right), \tag{4.11}$$

respectively. We approximate $\mathcal{R}^{\mathrm{M}}_{\alpha\alpha}(z_2)$ and $\mathcal{R}^{\mathrm{M}}_{\alpha\alpha}(z_3)$ by values obtained from the resolved LES field with test filters of width Δ_2 and Δ_3, respectively, i.e.

$$\mathcal{R}^{\mathrm{M}}_{\alpha\alpha}(z_2) = \left(p^r \frac{\partial u^r_\alpha}{\partial x_\alpha} + p^r \frac{\partial u^r_\alpha}{\partial x_\alpha}\right)^{r2} - \left(p^{r,r2} \frac{\partial u^{r,r2}_\alpha}{\partial x_\alpha} + p^{r,r2} \frac{\partial u^{r,r2}_\alpha}{\partial x_\alpha}\right) \tag{4.12}$$

and

$$\mathcal{R}^{\mathrm{M}}_{\alpha\alpha}(z_3) = \left(p^r \frac{\partial u^r_\alpha}{\partial x_\alpha} + p^r \frac{\partial u^r_\alpha}{\partial x_\alpha}\right)^{r3} - \left(p^{r,r3} \frac{\partial u^{r,r3}_\alpha}{\partial x_\alpha} + p^{r,r3} \frac{\partial u^{r,r3}_\alpha}{\partial x_\alpha}\right), \tag{4.13}$$

where r_3 and r_2 denote second filtering of the resolved LES velocity and pressure, u^r_i and p^r, at scales $\Delta_3 > \Delta_2 > \Delta_1$. Very importantly, if Δ_2 and Δ_3 are chosen such that

$$\frac{z_2}{\Delta_2} = \frac{z_3}{\Delta_3} = \frac{z_1}{\Delta_1}, \tag{4.14}$$

then

$$f_\alpha\left(\frac{z_2}{\Delta_2}\right) = f_\alpha\left(\frac{z_3}{\Delta_3}\right) = f_\alpha\left(\frac{z_1}{\Delta_1}\right) = f_\alpha \tag{4.15}$$

and

$$g_\alpha\left(\frac{z_2}{\Delta_2}\right) = g_\alpha\left(\frac{z_3}{\Delta_3}\right) = g_\alpha\left(\frac{z_1}{\Delta_1}\right) = g_\alpha. \tag{4.16}$$

Since f_α and g_α are constant for constant values of z_2/Δ_2 and z_3/Δ_3, (4.10) and (4.11) are fully determined and yield unique solutions corresponding to $f_\alpha\left(z_1/\Delta_1\right)$ and $g_\alpha\left(z_1/\Delta_1\right)$, and thus closing (4.9). The scaling-based similarity model thus consists of evaluating surrogate values for $\mathcal{R}_{\alpha\alpha}$ from the resolved fields at heights z_2 and z_3, respectively at scales Δ_2 and Δ_3, in order to obtain the coefficients f_α and g_α. The next section presents *a priori* tests of the model in the neutrally stratified and convective atmospheric boundary layers.

4.3 *A priori* tests

Although there are near-ground measurements of velocity and pressure (Nguyen et al. 2013; Nguyen and Tong 2015), observations at multiple heights throughout the surface layer are needed to evaluate the model coefficients f_α and g_α. In the absence of such field measurements, we evaluate the scaling-based similarity model using high-resolution large-eddy simulation. Such an approach has been employed by Laval et al. (1999), Dubrulle et al. (2002), and Yang et al. (2013). The LES

Atmospheric Stability	U_g $(\mathrm{m\,s^{-1}})$	Q_0 $(\mathrm{K\,m\,s^{-1}})$	$-L$ (m)	z_i (m)	u_* $(\mathrm{m\,s^{-1}})$	w_* $(\mathrm{m\,s^{-1}})$
Neutral	10	0	∞	981	0.45	0
Weakly convective	15	0.08	262	1017	0.65	1.38
Moderately convective	10	0.12	84	1032	0.51	1.59
Strongly convective	1	0.24	4	1076	0.24	2.02

Table 4.1: Large-eddy simulation parameters.

framework used is presented in detail in Moeng (1984), is well-documented in the literature (Moeng and Wyngaard 1988; Sullivan et al. 1994, 1996), and includes refinements by Otte and Wyngaard (2001). The approach solves the spatially-filtered momentum equation for Boussinesq flow and a transport equation for a filtered conserved scalar, supplemented with a transport equation for the SGS turbulent kinetic energy. A pressure Poisson equation, obtained by applying a numerical divergence operator to the momentum equation, enforces incompressibility.

The numerical scheme is pseudo-spectral in the horizontal directions and finite difference in the vertical, the latter implemented on a staggered mesh to maintain tight velocity-pressure coupling. The non-linear advection terms are implemented in rotational form, and aliasing errors are eliminated using an explicit sharp Fourier cutoff of the upper 1/3 wavenumbers (Canuto et al. 1988). Time stepping is performed using a third-order Runge-Kutta scheme (Spalart et al. 1991; Sullivan et al. 1996). Consistent with the pseudo-spectral method, periodic boundary conditions are used on the domain sidewalls. At the lower boundary, wall functions based on Monin-Obukhov similarity are used to estimate the surface stress and flux (Businger et al. 1971). At the upper boundary, a radiative boundary condition allows for gravity waves to pass through without reflection (Klemp and Durran 1983). Neumann boundary conditions, derived from the vertical momentum equation, supplement the pressure Poisson equation.

We simulate four cases of atmospheric boundary layer flow: (1) a (nearly) neutrally stratified ABL driven by a constant large-scale pressure gradient corresponding to geostrophic wind components $(U_g, V_g) = (10, 0)$ m s^{-1} (due to the stably stratified inversion, the boundary layer is slightly stable even with zero surface heat flux), (2) a weakly unstable and (3) moderately unstable ABL driven by a combination of geostrophic winds and surface heating, and (4) a nearly free-convective ABL driven by strong surface heat flux ($Q_0 = 0.24$ K m s^{-1}) and weak geostrophic winds. The parameters for the four cases are summarized in table 4.1. All simulations are implemented on a

mesh of 1024^3 grid points, with a domain size of 5120^2 m^2 in the horizontal and 2048 m in the vertical. We prescribe a surface roughness of $z_0 = 0.1$ m, Coriolis parameter $f = 1 \times 10^{-4}$ m s^{-1}, and an initial capping inversion at $z_i = 1024$ m. The simulations are carried forward for 25τ, where $\tau = z_i/w_*$ (or u_* for the neutral case) defines one large-eddy turnover time and $w_* = (\beta Q_0 z_i)^{1/3}$ is the convective (mixed layer) velocity scale (calculated using initial values of the boundary layer height and surface temperature flux). Statistics are averaged from $10\tau - 25\tau$.

While LES is capable of predicting turbulence statistics in the mixed layer, near the surface, especially at the first few grid points, the influence of the SGS model and the boundary conditions can be significant. We take several steps to minimize such influences on the *a priori* tests: First, to assess the sensitivity of the surrogate SGS fields on the SGS model, we simulate the weakly convective and strongly convective ABL using two SGS models with the same boundary conditions. We employ the Smagorinsky-Lilly model (Smagorinsky 1963; Lilly 1967) and the nonlinear model (Kosović 1997), which adds a nonlinear term to the eddy-viscosity formulation to account for backscatter effects. We find the surrogate SGS pressure–rate-of-strain to be in good agreement. Their mean and conditional mean, computed at the eighth grid point ($z = 16$ m), are also consistent with those of the measured SGS pressure–rate-of-strain (Nguyen et al. 2013; Nguyen and Tong 2015). The results hereafter employ the Smagorinsky-Lilly closure. Second, the *a priori* tests employ a coarse grid of 128 grid points in the vertical. The model is evaluated starting at the first coarse grid point ($z = 16$ m) and compared to the SGS pressure–rate-of-strain computed on the fine grid at the same heights. We find the latter, starting at $z = 16$ m, to be dynamically representative of the true (measured) SGS pressure–rate-of-strain, suggesting that the (fine grid) simulations are sufficiently resolved at the eighth grid point.

The scaling-based similarity SGS model is tested *a priori* following the standard approach (e.g. Piomelli et al. 1988). The three-dimensional data are first filtered in the horizontal planes using a top-hat filter of width Δ_f, corresponding to cutoff wavenumber k_c. The resolved fields on the resulting coarse grid contain all motions with $(k_x, k_y) < k_c$, where k_x and k_y are the horizontal wavenumbers in the x and y directions, respectively, while the subgrid fields contain wavenumbers $|\boldsymbol{k}| > k_c$. For our analyses, the (fine grid) LES resolution is given by $(\Delta_x, \Delta_y, \Delta_z) = (5,5,2)$ m. We define a coarse grid with 128 grid points in the vertical direction ($\Delta_z = 16$ m), with resolved fields obtained by filtering the high-resolution data with filters of width $\Delta_f (= \Delta_{x,y}) = 10$, 20, and 40 m, in order to vary the filter (coarse grid) aspect ratio. The modelled SGS pressure–strain-rate correlation,

obtained using (4.8), on this coarse grid is then compared to the true SGS pressure–rate-of-strain computed from the fine grid. Very importantly, the model is evaluated based solely on the resolved fields sampled on the coarse grid and does not contain information below k_c.

4.3.1 Mean SGS pressure–rate-of-strain

The mean profiles of the true and modelled SGS pressure–strain-rate correlation are shown in figures 4.1-4.4. The latter is evaluated for the first five grid points on the coarse mesh dynamically from the surrogate SGS pressure–rate-of-strain at heights $2z$ and $4z$ (with test filters of width $2\Delta_f$ and $4\Delta_f$, respectively). The results for the neutral, weakly convective, and moderately convective surface layers are normalized by surface layer scales ($\kappa z/u_*^3$), while those for the nearly free-convective case are normalized by mixed layer scales (z_i/w_*^3). The coarse grid aspect ratio, $\Delta_{x,y}/\Delta_z$, corresponding to horizontal (filter) grid spacings of 10, 20, and 40 m, are given by 0.625, 1.25, and 2.5, respectively. An increase of the aspect ratio corresponds to a decrease in the horizontal grid resolution, which moves Reynolds stress from the resolved to the subgrid scales in the horizontal and results in stronger dependence of the LES on the SGS model, and in our case the predicted surface-layer anisotropy on the SGS pressure–rate-of-strain model.

Figure 4.1 shows the mean profiles of the true and modelled SGS pressure–rate-of-strain in the neutrally stratified surface layer. In the absence of surface heating, the model consists solely of its the neutral contribution. Consistent with $\langle \mathcal{R}_{\alpha\alpha} \rangle$, $\langle \mathcal{R}_{11}^{\mathrm{M}} \rangle$ is negative while $\langle \mathcal{R}_{22}^{\mathrm{M}} \rangle$ and $\langle \mathcal{R}_{33}^{\mathrm{M}} \rangle$ are both positive, indicating redistribution of SGS energy by $\langle \mathcal{R}_{\alpha\alpha}^{\mathrm{M}} \rangle$ from $\langle \tau_{11} \rangle$ to $\langle \tau_{22} \rangle$ and $\langle \tau_{33} \rangle$. For relatively well-resolved turbulence ($\Delta_{x,y}/\Delta_z = 0.625$), the predicted SGS pressure–strain-rate above the first grid point is generally close to that of the true SGS pressure-strain. At the first grid point, the model over-predicts the true pressure–rate-of-strain by a factor of 2. For larger values of the aspect ratio, the model under-predicts the pressure–rate-of-strain. This is likely due to the under-resolution of the surrogate (double-filtered) SGS fields at $2z$ and $4z$, which are used to evaluate the model coefficients at z. The behaviour of the surrogate SGS pressure–rate-of-strain, however, is consistent with return to isotropy, and therefore yields correct predictions of the direction of energy transfer (from $\langle \tau_{11} \rangle$ to $\langle \tau_{22} \rangle$ and $\langle \tau_{33} \rangle$).

The modelled SGS pressure–rate-of-strain in the weakly and moderately convective surface layers includes both neutral (shear) and convective (buoyancy) contributions. For the weakly convective surface layer, the shear contribution is dominant due to relatively weak surface temperature

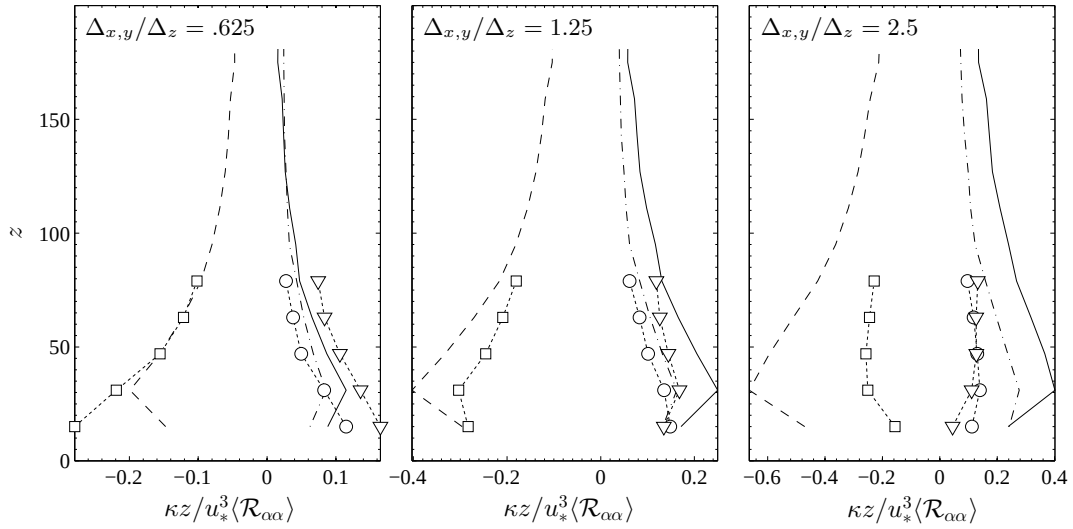

Figure 4.1: Mean profiles of the true and modelled SGS pressure–strain-rate correlation for the neutrally stratified surface layer, computed for varying values of the grid aspect ratio: The true streamwise (– –), spanwise (– · –), and vertical (——) components. The modelled streamwise (--□--), spanwise (--○--), and vertical (--▽--) components at the first five grid points.

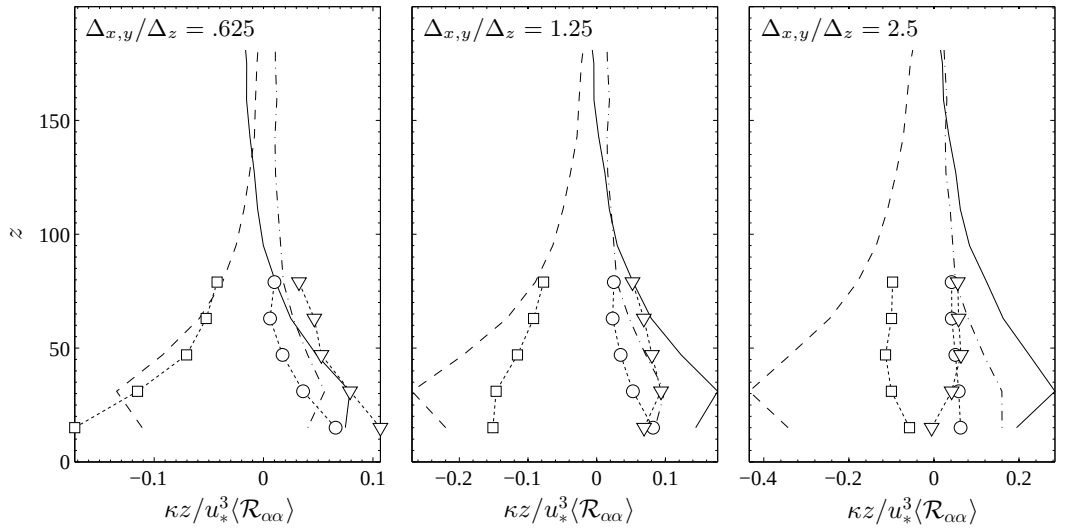

Figure 4.2: Mean profiles of the true and modelled SGS pressure–rate-of-strain for the weakly convective surface layer, computed for varying values of the grid aspect ratio. Symbols as in figure 4.1.

flux ($Q_0 = 0.08$ K m s^{-1}). The modelled SGS pressure-strain (figure 4.2) therefore is similar to that for the neutrally stratified surface layer and consistent with return to isotropy. The model generally under-predicts $\langle \mathcal{R}_{\alpha\alpha} \rangle$, again likely due to under-resolution of the surrogate SGS fields, which worsens with increasing grid aspect ratio but improves with height. For the well-resolved LES field ($\Delta_{x,y}/\Delta_z = 0.625$), the model prediction at the second grid point is generally within 20% of the true mean. For the moderately- and poorly-resolved fields ($\Delta_{x,y}/\Delta_z = 1.25$ and 2.5, respectively), the model under-predicts $\langle \mathcal{R}_{\alpha\alpha} \rangle$ by a factor of 2 and 4, respectively, at the same height. The predicted direction of energy transfer (from $\langle \tau_{11} \rangle$ to $\langle \tau_{22} \rangle$ and $\langle \tau_{33} \rangle$) however remains consistent with return to isotropy.

The results for the moderately convective surface layer (figure 4.3) indicate return to isotropy near the ground (redistribution from $\langle \tau_{11} \rangle$ to $\langle \tau_{22} \rangle$ and $\langle \tau_{33} \rangle$) and generation of anisotropy away from the surface (redistribution from $\langle \tau_{33} \rangle$ to $\langle \tau_{11} \rangle$ and $\langle \tau_{22} \rangle$). For the well-resolved LES field, this transition occurs at $z = 100$ m ($-z/L = 1.2$) for $\langle \mathcal{R}_{11} \rangle$ and $z = 50$ m ($-z/L = 0.6$) for $\langle \mathcal{R}_{33} \rangle$. The former is well-predicted by $\langle \mathcal{R}^{\mathrm{M}}_{11} \rangle$, while the latter is generally under-predicted by $\langle \mathcal{R}^{\mathrm{M}}_{33} \rangle$ (whose zero-crossing is likely to occur at larger $-z/L$). The model predictions, though generally indicating a transition from return to isotropy to generation of anisotropy, worsen with increasing grid aspect ratio. For the moderately convective surface layer, the misprediction of $\langle \mathcal{R}_{\alpha\alpha} \rangle$ near the surface is a result of the dynamic procedure (which uses $\langle \mathcal{R}_{\alpha\alpha} \rangle$ at much higher planes to evaluate the model coefficients at z). Because $\langle \mathcal{R}_{\alpha\alpha} \rangle$ is much more likely to cause generation of anisotropy at z_2 and z_3 (stronger convective instability), the model inherently under-predicts the neutral contribution and over-predicts the convective contribution. Therefore $\langle \mathcal{R}_{\alpha\alpha} \rangle$ is under-predicted near the surface, where return to isotropy dominates. These effects are less significant for the weakly convective surface layer ($-L = 262$ m) since the transition of $\langle \mathcal{R}_{\alpha\alpha} \rangle$ from return to isotropy to generation of anisotropy occurs at much higher z.

Figure 4.4 shows the mean profiles of the true and modelled SGS pressure–rate-of-strain in the nearly free-convective surface layer. Owing to weak geostrophic winds ($U_g = 1$ m s^{-1}) and strong surface heating ($Q_0 = 0.24$ K m s^{-1}), the model consists primarily of its convective contribution. Consistent with $\langle \mathcal{R}_{\alpha\alpha} \rangle$, $\langle \mathcal{R}^{\mathrm{M}}_{33} \rangle$ is negative while $\langle \mathcal{R}^{\mathrm{M}}_{11} \rangle$ and $\langle \mathcal{R}^{\mathrm{M}}_{22} \rangle$ are positive, indicating redistribution from $\langle \tau_{33} \rangle$ to $\langle \tau_{11} \rangle$ and $\langle \tau_{22} \rangle$. Because $\langle \tau_{11} \rangle > \langle \tau_{33} \rangle$ and $\langle \tau_{22} \rangle > \langle \tau_{33} \rangle$, the model predictions are therefore consistent with generation of SGS anisotropy. Note that the first grid point is well-within the convective (anisotropic) regime since $-L = 4$ ($-z/L = 4$). The model predictions for this case

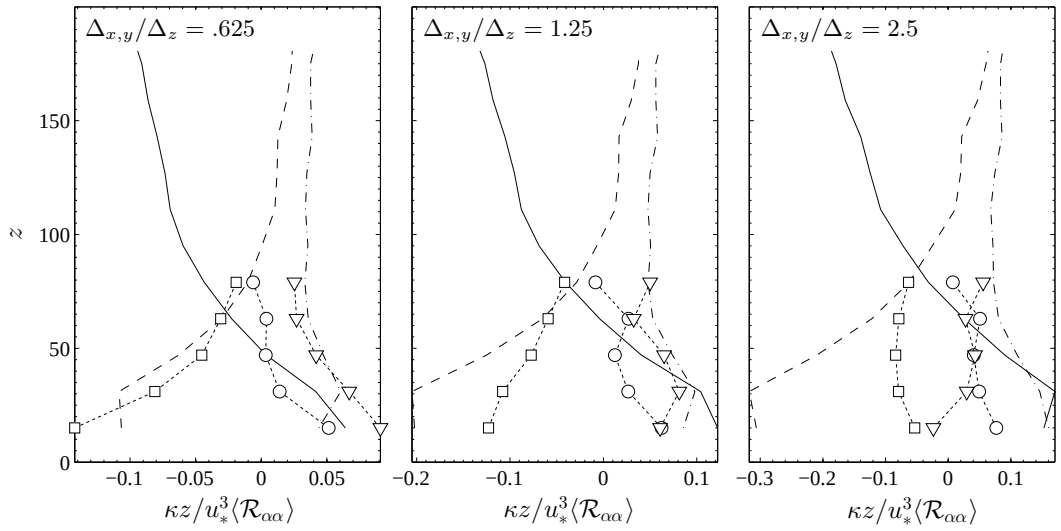

Figure 4.3: Mean profiles of the true and modelled SGS pressure–rate-of-strain for the moderately convective surface layer, computed for varying values of the grid aspect ratio. Symbols as in figure 4.1.

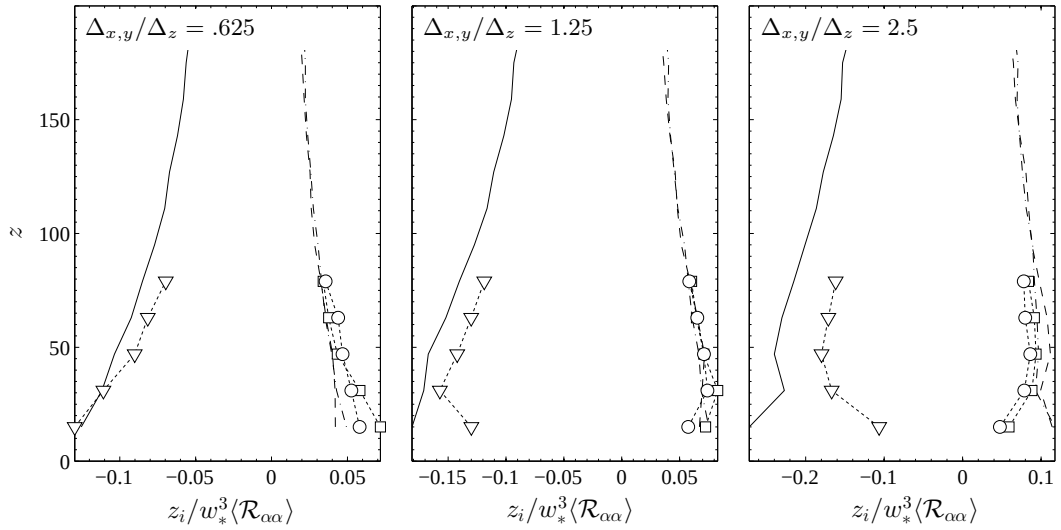

Figure 4.4: Mean profiles of the true and modelled SGS pressure–rate-of-strain for the free-convective surface layer, computed for varying values of the grid aspect ratio. Symbols as in figure 4.1.

are also generally much better than those for the weakly and moderately convective cases. For relatively well-resolved turbulence ($\Delta_{x,y}/\Delta_z = 0.625$), $\langle \mathcal{R}^{\mathrm{M}}_{\alpha\alpha} \rangle$ is generally within 10% of $\langle \mathcal{R}_{\alpha\alpha} \rangle$. For poorly-resolved turbulence ($\Delta_{x,y}/\Delta_z = 2.5$), the model under-predicts $\langle \mathcal{R}_{\alpha\alpha} \rangle$ by approximately 25% above the first grid point. Predictions of $\langle \mathcal{R}_{11} \rangle$ and $\langle \mathcal{R}_{22} \rangle$ however appear to improve with height, again likely due to more accurate estimates of the true SGS pressure–rate-of-strain at $2z$ and $4z$ by the surrogate SGS fields.

4.3.2 Conditional mean SGS pressure–rate-of-strain

In addition to their means, we also compare the conditional means of the true and modelled SGS pressure–strain-rate correlation. Conditional statistics have been shown to be optimal predictors of SGS model performance (Langford and Moser 1999) and are capable of identifying model strengths and deficiencies in both *a priori* and *a posteriori* tests (Chen and Tong 2006; Chen et al. 2009, 2010). Nguyen and Tong (2015) showed that the terms which evolve the conditional mean SGS stress transport equation, particularly the conditional mean SGS pressure–strain-rate correlation, must be correctly predicted by the SGS model in order for LES to reproduce the resolvable-scale velocity joint probability density function. Below, we show the conditional mean of the true and modelled SGS pressure–rate-of-strain, $\langle \mathcal{R}_{\alpha\alpha} | \boldsymbol{u}^r \rangle$ and $\langle \mathcal{R}^{\mathrm{M}}_{\alpha\alpha} | \boldsymbol{u}^r \rangle$, respectively, computed at the first coarse grid point ($z = 16$ m) for varying values of the grid aspect ratio. In this study, $\langle \mathcal{R}_{\alpha\alpha} | \boldsymbol{u}^r \rangle$ and $\langle \mathcal{R}^{\mathrm{M}}_{\alpha\alpha} | \boldsymbol{u}^r \rangle$ are conditioned on the fluctuating parts of the streamwise and vertical components of the resolvable-scale velocity (u^r_1 and u^r_3, respectively), both of which are normalized by their respective resolved-scale r.m.s. values. For clarity, we multiply $\langle \mathcal{R}^{\mathrm{M}}_{\alpha\alpha} | \boldsymbol{u}^r \rangle$ by $|\langle \mathcal{R}_{\alpha\alpha} \rangle / \langle \mathcal{R}^{\mathrm{M}}_{\alpha\alpha} \rangle|$ (computed at the second grid point). Doing so matches the means of the true and modelled SGS pressure-strain, but does not affect the trends of $\langle \mathcal{R}^{\mathrm{M}}_{\alpha\alpha} | \boldsymbol{u}^r \rangle$ (i.e. the dependence of $\mathcal{R}^{\mathrm{M}}_{\alpha\alpha}$ on u^r_i). Conditional mean statistics are obtained using the first-order kernel density estimation method (Wand and Jones 1995), resulting in faster convergence and lower bias. We limit the results to the central part of the sample space containing 99.9% of the velocity probability density function.

The streamwise and vertical components of the conditional mean SGS pressure–strain-rate correlation are shown in figures 4.5-4.12. The results for the neutrally stratified surface layer (figures 4.5 and 4.6) are consistent with return to isotropy and generally reflect the dependence of $\langle \mathcal{R}_{\alpha\alpha} \rangle$ on u^r_3. Consistent with $\langle \mathcal{R}_{\alpha\alpha} | \boldsymbol{u}^r \rangle$, $\langle \mathcal{R}^{\mathrm{M}}_{11} | \boldsymbol{u}^r \rangle < 0$ and $\langle \mathcal{R}^{\mathrm{M}}_{33} | \boldsymbol{u}^r \rangle > 0$ for most values of u^r_1 and u^r_3, indicating conditional energy redistribution from the streamwise to the vertical velocity component

through pressure-strain interaction. For negative u_3^r fluctuations (downdrafts), the rate of redistribution is weaker due to the wall damping effect, which results in a reduction of the wall-normal SGS velocity component and therefore a weaker rate of return to isotropy. The wall damping is well-predicted by the scaling-based similarity model, especially for large filter widths ($\Delta_{x,y}/\Delta_z = 2.5$). For $\Delta_{x,y}/\Delta_z = 1.25$, the magnitudes of $\langle \mathcal{R}_{11}^{\mathrm{M}} | \boldsymbol{u}^r \rangle$ and $\langle \mathcal{R}_{33}^{\mathrm{M}} | \boldsymbol{u}^r \rangle$ appear to increase with increasing $|u_3^r|$, somewhat inconsistent with $\langle \mathcal{R}_{\alpha\alpha} | \boldsymbol{u}^r \rangle$. For small aspect ratio ($\Delta_{x,y}/\Delta_z = 0.625$), the dependence of both $\langle \mathcal{R}_{\alpha\alpha} | \boldsymbol{u}^r \rangle$ and $\langle \mathcal{R}_{\alpha\alpha}^{\mathrm{M}} | \boldsymbol{u}^r \rangle$ on u_3^r weakens, consistent with field measurements of the SGS pressure–rate-of-strain (Nguyen and Tong 2015).

The results for the weakly convective surface layer (figures 4.7 and 4.8) are generally similar to those of the neutrally stratified ABL (i.e. return to isotropy), though for large aspect ratio, there appears to be a weak dependence of $\langle \mathcal{R}_{\alpha\alpha} | \boldsymbol{u}^r \rangle$ on u_1^r, which is not reproduced by the model. Due to the weak surface heating ($Q_0 = 0.08\ \mathrm{K\,m\,s^{-1}}$), there are some negative values of $\langle \mathcal{R}_{33} | \boldsymbol{u}^r \rangle$, which are restricted to relatively small regions of the sample space but nonetheless indicate the wall blocking effect and a transition of $\langle \mathcal{R}_{\alpha\alpha} \rangle$ from return to isotropy to generation of anisotropy.

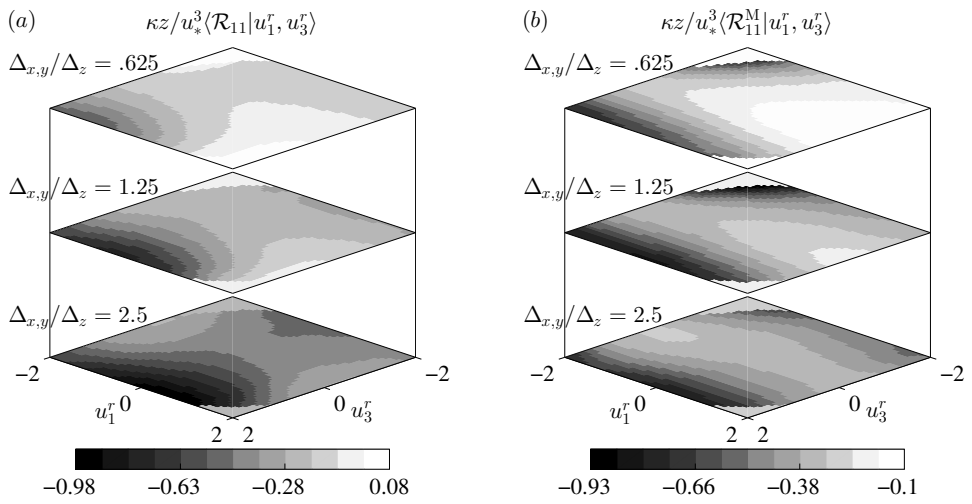

Figure 4.5: The conditional mean of the (a) true and (b) modelled streamwise SGS pressure–rate-of-strain component for the neutrally stratified surface layer, computed at the first grid point for varying values of the grid aspect ratio.

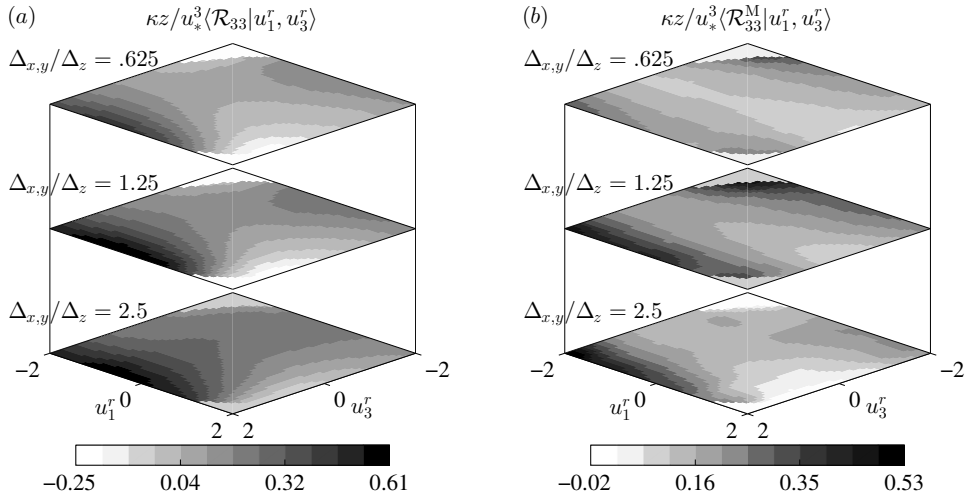

Figure 4.6: As in figure 4.5, but for the vertical component.

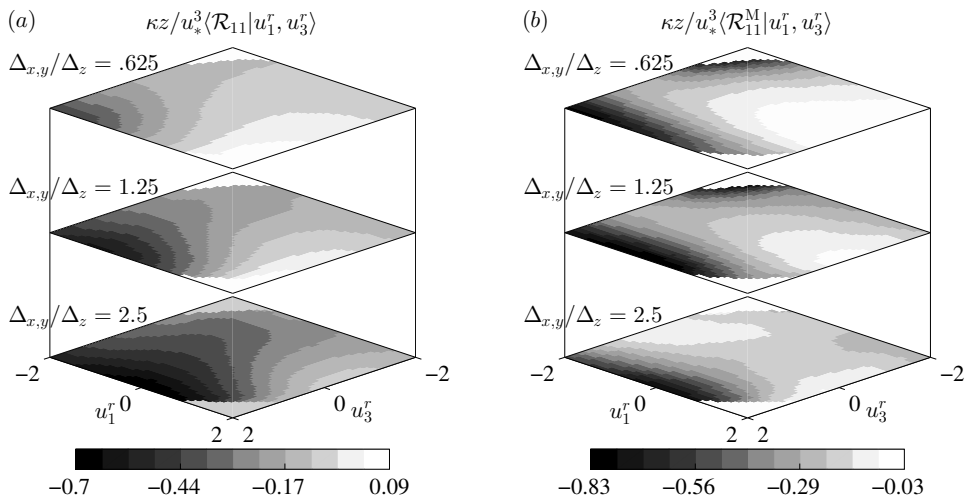

Figure 4.7: The conditional mean of the (a) true and (b) modelled streamwise SGS pressure–rate-of-strain component for the weakly convective surface layer, computed at the first grid point for varying values of the grid aspect ratio.

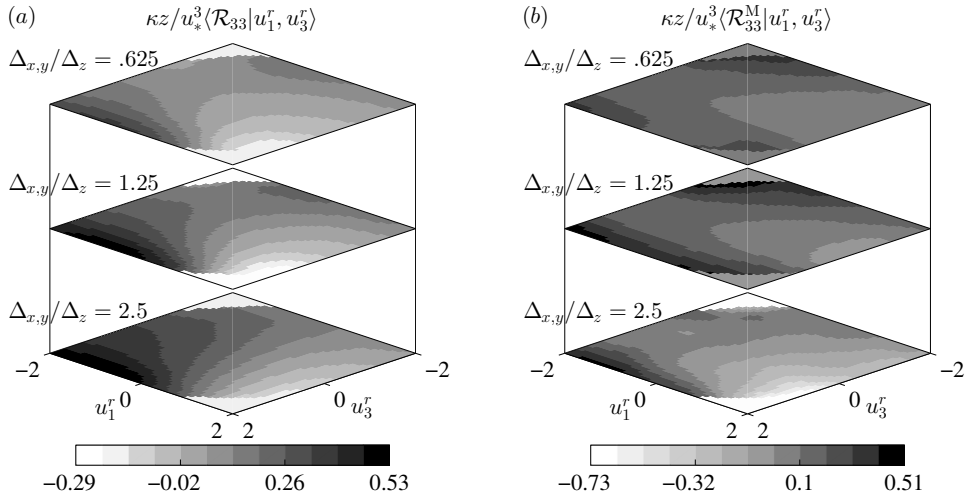

Figure 4.8: As in figure 4.7, but for the vertical component.

Because the first (coarse) grid point lies near the dynamic scaling range ($-z/L = 0.2$), the results for the moderately convective surface layer (figures 4.9 and 4.10), though modulated by stronger surface heating ($Q_0 = 0.12\ \mathrm{K\,m\,s^{-1}}$), are generally similar to those of the neutrally stratified ABL, particularly those for the streamwise component of the SGS pressure–rate-of-strain. The results for the vertical component show large portions of negative $\langle \mathcal{R}_{33}|\boldsymbol{u}^r\rangle$ for negative u_3^r fluctuations, indicating generation of anisotropy. These trends are consistent with the mean profiles of $\langle \mathcal{R}_{\alpha\alpha}\rangle$ (figure 4.3), which show that $\langle \mathcal{R}_{33}\rangle$ transitions from return to isotropy to generation of anisotropy (i.e. approaches the zero-crossing) before $\langle \mathcal{R}_{11}\rangle$. The rate of anisotropization, however, is weak compared to the rate of return to isotropy since the eddy dynamics at the first grid point are still shear-dominated ($-z/L = 0.2$). The scaling-based similarity model predicts the dependence of $\langle \mathcal{R}_{11}|\boldsymbol{u}^r\rangle$ on u_3^r markedly well, especially for large aspect ratio. For smaller aspect ratios, however, it under-predicts the weak dependence of $\langle \mathcal{R}_{11}|\boldsymbol{u}^r\rangle$ on u_1^r. In contrast, for large aspect ratio, the model over-predicts the dependence of $\langle \mathcal{R}_{33}|\boldsymbol{u}^r\rangle$ on u_1^r and under-predicts its dependence on u_3^r. The predicted local maximum of $\langle \mathcal{R}_{33}|\boldsymbol{u}^r\rangle$ for negative u_1^r (and positive u_3^r) is also generally inconsistent with field measurement results, which show stronger pressure redistribution for positive u_1^r (and positive u_3^r) (Nguyen and Tong 2015).

The results for the nearly free-convective surface layer are shown in figures 4.11 and 4.12. Because the first grid point for this case is well-within the convective (anisotropic) regime ($-z/L = 4$), both $\langle \mathcal{R}_{11}|\boldsymbol{u}^r\rangle$ and $\langle \mathcal{R}_{33}|\boldsymbol{u}^r\rangle$ are strongly influenced by wall effects. For positive u_3^r fluctuations, $\langle \mathcal{R}_{11}|\boldsymbol{u}^r\rangle < 0$ and $\langle \mathcal{R}_{33}|\boldsymbol{u}^r\rangle > 0$, consistent with return to isotropy. For negative u_3^r, $\langle \mathcal{R}_{11}|\boldsymbol{u}^r\rangle > 0$ and $\langle \mathcal{R}_{33}|\boldsymbol{u}^r\rangle < 0$, indicating conditional energy redistribution from the vertical to the streamwise (and spanwise) velocity components and therefore generation of isotropy. The scaling-based similarity model predicts the dependence of $\langle \mathcal{R}_{\alpha\alpha}|\boldsymbol{u}^r\rangle$ on u_3^r markedly well, but over-predicts their dependence on u_1^r, particularly for large aspect ratio. For negative u_3^r fluctuations, it correctly predicts generation of anisotropy. For positive u_3^r, it correctly predicts return to isotropy for negative u_1^r and relatively weaker rates of pressure redistribution for positive u_1^r, the latter inconsistent with $\langle \mathcal{R}_{\alpha\alpha}|\boldsymbol{u}^r\rangle$. For smaller aspect ratios, the model correctly predicts the weakening dependence of $\langle \mathcal{R}_{\alpha\alpha}|\boldsymbol{u}^r\rangle$ on the resolvable-scale velocity. Consistent with $\langle \mathcal{R}_{\alpha\alpha}|\boldsymbol{u}^r\rangle$, $\langle \mathcal{R}^{\mathrm{M}}_{11}|\boldsymbol{u}^r\rangle$ and $\langle \mathcal{R}^{\mathrm{M}}_{33}|\boldsymbol{u}^r\rangle$ also indicate weaker rates of anisotropization. Nguyen and Tong (2015) show that there is an eventual reversal of the direction of energy exchange (from $\langle \tau_{11}|\boldsymbol{u}^r\rangle$ to $\langle \tau_{33}|\boldsymbol{u}^r\rangle$, regardless of the value of u_3^r) for very small aspect ratios, consistent with $\langle \mathcal{R}^{\mathrm{M}}_{\alpha\alpha}|\boldsymbol{u}^r\rangle$.

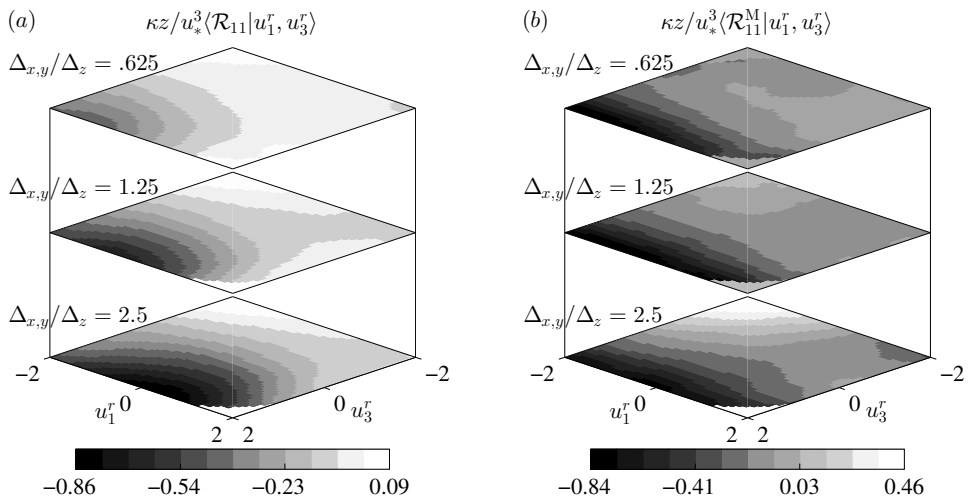

Figure 4.9: The conditional mean of the (a) true and (b) modelled streamwise SGS pressure–rate-of-strain component for the moderately convective surface layer, computed at the first grid point for varying values of the grid aspect ratio.

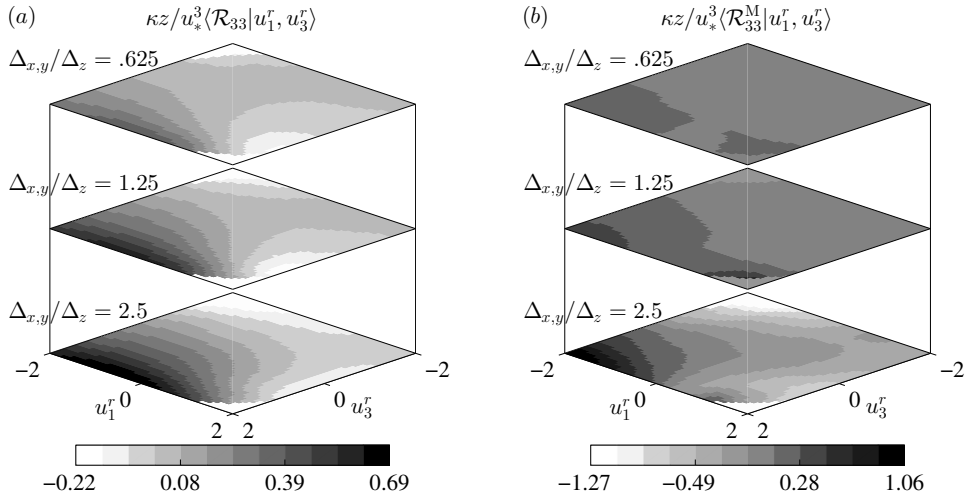

Figure 4.10: As in figure 4.9, but for the vertical component.

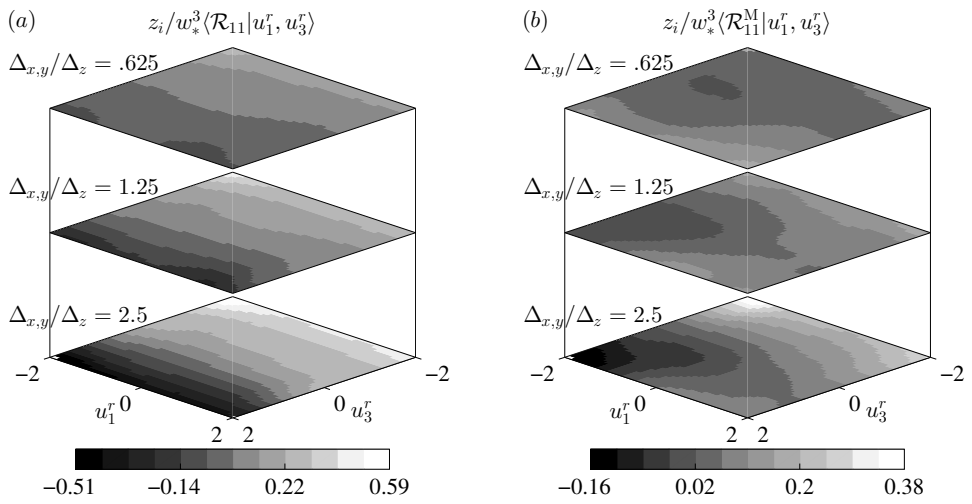

Figure 4.11: The conditional mean of the (a) true and (b) modelled streamwise SGS pressure–rate-of-strain component for the free-convective surface layer, computed at the first grid point for varying values of the grid aspect ratio.

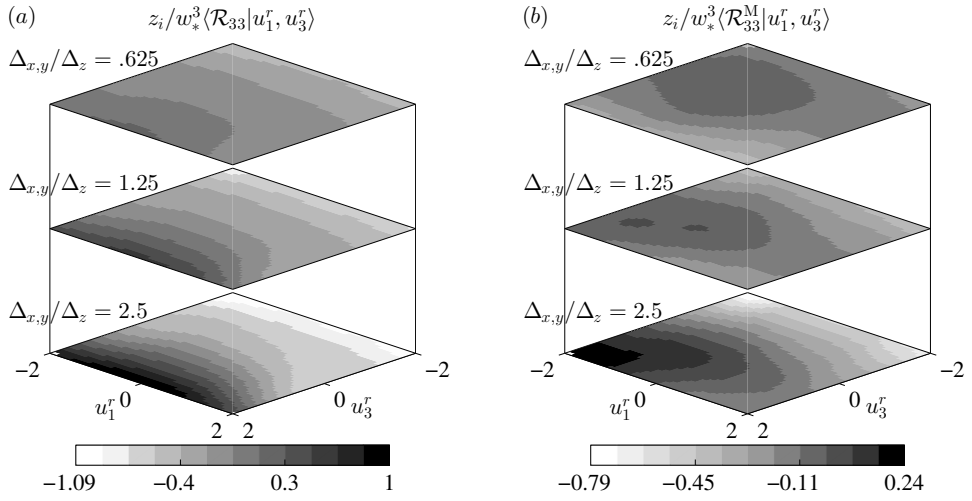

Figure 4.12: As in figure 4.11, but for the vertical component.

4.4 Discussion and conclusions

A generalised model for the normal (redistributive) components of the SGS pressure–rate-of-strain in the ABL is proposed and evaluated *a priori*. The model is derived using basic scaling arguments and predicts $\mathcal{R}_{\alpha\alpha}$ as the linear sum of two competing effects, an isotropization effect characteristic of the shear-dominated neutral surface layer and an anisotropization effect characteristic of the buoyancy-dominated convective one. The model coefficients are determined dynamically from the resolved fields, at heights where we expect LES to be relatively well-resolved. Preliminary *a priori* tests using high-resolution simulations of the neutrally stratified and nearly free-convective ABL show that the model is capable of predicting both return to isotropy (for the former) and generation of anisotropy (for the latter). In cases where both shear and buoyancy are important, the model predicts a transition from return to isotropy (for $z < -L$) to generation of anisotropy (for $z > -L$). For large grid aspect ratio, the magnitudes of $\langle \mathcal{R}_{\alpha\alpha} \rangle$ are generally under-predicted due to under-resolution of the surrogate SGS fields. Additionally, when the heights of these fields are comparable to $-L$, the model inherently under-predicts the neutral contribution and over-predicts the convective contribution since its coefficients are skewed towards the latter.

The conditional means of the modelled terms, a more robust measure of SGS model performance, are generally consistent with those of the true pressure–rate-of-strain. For the neutrally stratified and weakly convective surface layers, the model predicts weaker rates of pressure redistribution (from $\langle \tau_{11} \rangle$ to $\langle \tau_{33} \rangle$) during downdrafts, consistent with wall damping effects and return to isotropy; while for the moderately and strongly convective surface layers, it predicts conditional energy redistribution from $\langle \tau_{33} \rangle$ to $\langle \tau_{11} \rangle$ during downdrafts, consistent with wall blocking effects and generation of anisotropy. Though the dependence of $\langle \mathcal{R}_{\alpha\alpha} | \boldsymbol{u}^r \rangle$ on u_1^r is somewhat over-predicted by the model, the results are generally in agreement with previous field measurement studies (Nguyen et al. 2013; Nguyen and Tong 2015).

The *a priori* analyses indicate that the scaling-based similarity modelling approach may yield better predictions of the surface-layer anisotropy in buoyancy-driven atmospheric boundary layer flows. In such flows, the SGS dynamics are governed by large-scale convective eddies, which produce much stronger pressure fluctuations than those in the neutral surface layer. Wall models which under-predict the scale of these dominant eddies therefore are likely to mispredict generation of anisotropy, since wall blocking of these large-scale eddies is not included in the closure. We note

that the general closure of Gibson and Launder (1978) accounts for buoyancy effects by modelling $R_{ij}^{(b)}$ using the buoyancy production tensor anisotropy; wall effects are modelled using an empirical damping function that is roughly constant in the log-law region and vanishes away from the wall. Such a model is likely to predict generation of anisotropy; however, when applied in the context of transport-equation-based SGS modelling, requires correct prediction of the SGS vertical temperature flux (and therefore correct prediction of the SGS scalar variance).

Although the present study focuses on the SGS pressure–rate-of-strain, a general form of the scaling-based model is derived for the Reynolds-stress pressure–strain-rate correlation (equation 4.6), in which the model coefficient $G_\alpha\left(z/z_i\right)$, corresponding to the convective contribution to $R_{\alpha\alpha}$ ($R_{\alpha\alpha}^{(c)}$), requires closure. The dependence of $R_{\alpha\alpha}^{(n)}$ (the neutral contribution) on z/z_i is expected to be negligible since the dominant eddies in the neutrally stratified surface layer scale with z ($\ll z_i$). The dependence of $R_{\alpha\alpha}^{(c)}$ on $G_\alpha\left(z/z_i\right)$, however, is expected to be significant because the energy-containing eddies in the convective ABL are much larger. Nguyen et al. (2014) propose a general form for $G_\alpha\left(z/z_i\right)$ using the attached eddy hypothesis (Townsend 1976). The hypothesis supposes that eddies which are directly influenced by the presence of a wall are in a sense 'attached' to it, and therefore predicts that the energy-containing motions are governed by the superposition of such eddies, which have different sizes but similar velocity distributions. The dependence of the Reynolds stress pressure–strain-rate correlation on the large-scale convective eddies, which interact with the ground, suggests a possible extension of this approach to the modelling of $R_{\alpha\alpha}^{(c)}$.

Chapter 5

Summary and concluding remarks

The aim of this work was to provide an understanding of the subgrid-scale physics in the near-wall region of the convective atmospheric boundary layer. In this 'terra incognita' (Wyngaard 2004), the LES filter scale is comparable to that of the energy- and flux-containing eddies, resulting in inherent under-resolution of the turbulence field and increased dependence of the LES on the SGS model. The role of the SGS parameterization within this region therefore is crucial since it must represent the dynamics of the SGS stress and scalar flux. To develop improved SGS parameterizations requires incorporating additional physics, including history and local effects, into the SGS closure. The transport-equation-based modelling approach (Deardorff 1972, 1973), which involves solving the full conservation equations for the SGS stress and scalar flux, is best suited for this purpose and has the potential to predict LES statistics with more accuracy. Although their closure is based on Reynolds-stress second-moment closure modelling, relatively little is known of the terms which evolve the SGS transport equations, especially those containing fluctuating pressure, and their dependence on the surface layer stability and filter width. In this work, we used field measurements and high-resolution numerical simulations to investigate these terms and their dependence on the surface-layer dynamics.

In chapter 2, field measurements from the Advection Horizontal Array Turbulence Study (AHATS) were used to analyse the complete budgets of the SGS turbulence kinetic energy, SGS stress, and SGS potential temperature flux. AHATS notably includes high-fidelity measurements of the fluctuating pressure field, enabling separation of the resolvable- and subgrid-scale pressure, and therefore allowing for the first-time-ever observations of all of the terms which evolve the SGS

transport equations. The results show that the SGS TKE budget is similar to that of the Reynolds stress TKE for large filter widths. For near-neutral surface layers, there is a balance between the mechanical production and viscous dissipation of TKE. For unstable surface layers, the mechanical production, buoyant production, and pressure transport are balanced by the turbulent transport and viscous dissipation. As the filter width decreases, buoyancy and transport diminish, and the TKE budget is reduced to a balance between the mechanical production and viscous dissipation. The budgets of the SGS shear stress and SGS temperature flux, on the other hand, are qualitatively similar for both neutral and convective surface layers. In both, there is an approximate balance between production and pressure destruction.

The behaviours of the normal components of the SGS stress, meanwhile, are much more complex in the unstable surface layer than in the neutral ABL due largely to the interactions among shear, buoyancy, pressure, and the presence of the ground. For neutral surface layers and large filter widths, energy from the mean flow is fed to the streamwise velocity component and redistributed to the spanwise and vertical components through the pressure–rate-of-strain. For very small filter widths, there is an equal partitioning of SGS energy, causing the pressure redistribution to vanish. For unstable surface layers, energy is also fed to the (relatively smaller) vertical velocity component through buoyant production and pressure transport. For very large filter widths, this energy is redistributed to the (larger) streamwise and spanwise components through the pressure–strain-rate correlation. Thus, in contrast to the neutral ABL, where the SGS pressure–rate-of-strain acts to reduce the SGS anisotropy, in the convective surface layer it is the main cause of anisotropy for large filter widths. We attribute this effect to the ground blockage of the downward motions of the large-scale convective eddies, which is more dominant at large filter widths than the tendency to return to isotropy. For smaller filter widths, the ground blocking effect is reduced and the pressure–rate-of-strain reverts to the role of return to isotropy. For very small filter widths, there is again an equal partitioning of energy among the normal SGS components.

In chapter 3, we derived the transport equations for the conditional mean SGS stress and SGS potential temperature flux, and showed that the terms contained therein must be correctly predicted by the SGS model in order for LES to reproduce the resolvable-scale velocity joint probability density function and the resolvable-scale temperature probability density function. When conditioned on the resolvable-scale velocity, the conditional budget terms show a strong dependence on the updrafts generated by buoyancy, downdrafts associated with the returning flow, and wall

blocking effects. The results for the conditional mean SGS velocity–pressure-gradient correlation in the budget of the conditional mean SGS shear stress and that of the conditional mean SGS temperature–pressure-gradient correlation in the budget of the conditional mean SGS temperature flux are qualitatively similar for both weakly and strongly convective surface layers; that is, they act to counter the conditional mean production. We observe weaker rates of pressure destruction during downdrafts, reflecting wall damping effects.

The budgets of the normal components of the conditional mean SGS stress are markedly more complex, particularly under conditions of strong convective instability, where, for large filter widths, the conditional mean production, advection in physical space, pressure transport, pressure–strain-rate interaction, and dissipation play an active role. During updrafts, conditional mean production and pressure transport are the dominant sources of SGS energy (the former for the streamwise and the latter for vertical component), while conditional mean advection and dissipation are the dominant sinks. The results for the pressure transport suggest that the import of turbulent kinetic energy into the surface layer by pressure work is likely due to the negative local pressure minima which follow large-scale updrafts. During downdrafts, on the other hand, the conditional mean advection, which feeds back to the conditional mean SGS stress much of the energy taken from it during updrafts, is the dominant source for the vertical velocity component. Much of this energy is subsequently transferred to the streamwise component by the conditional mean pressure–strain-rate correlation; meanwhile, dissipation is a sink.

The dynamics of the SGS pressure–strain-rate correlation in the strongly convective surface layer are notable, particularly in contrast to its behaviour in the weakly convective ABL. Under conditions of near-neutral stratification, the role played by the conditional mean SGS pressure–rate-of-strain is qualitatively similar to that of the (unconditional) mean pressure-strain, both causing return to isotropy. For large filter widths, the results show that wall blocking of the vertical-velocity fluctuations during downdrafts dampens the rate of conditional energy redistribution from the streamwise to the spanwise and vertical components (i.e. the rate of return to isotropy), but does not reverse it. As the filter width decreases, conditional mean production for the latter components becomes significant and the conditional mean SGS stress is likely to be more isotropic. For these filter scales, the role of the conditional mean SGS pressure–strain-rate correlation diminishes, much like that of the mean SGS pressure–rate-of-strain.

For moderately and strongly convective surface layers, the results for the conditional mean

SGS pressure–strain-rate correlation show conditional energy redistribution from the (larger) horizontal to the (smaller) vertical velocity component during updrafts, likely due to stronger vertical stretching of the energy-containing eddies. During downdrafts, however, they show conditional energy redistribution in the reverse direction (i.e. from the smaller vertical to the larger horizontal components) and therefore generation of SGS anisotropy. The results also show that the conditional mean SGS pressure is generally positive for negative vertical velocity fluctuations and vice versa. Because of the asymmetry between the SGS pressure within updrafts and downdrafts, however, generation of anisotropy is due to the positive SGS pressure fluctuations associated with the returning downflow of the convective eddies. The role played by the wall blocking effect and wall pressure reflection within this mechanism is to enhance the anisotropy, but the latter is unlikely to be the main cause of anisotropy. The results substantiate the importance of wall effects on the evolution of the (unconditional) mean SGS stress, for which the pressure–strain-rate correlation is the primary cause of anisotropy.

Based on these results, in chapter 4 we construct a new model to parameterize the normal (redistributive) components of the SGS pressure–strain-rate correlation. Different from previous closures, which separately model the effects of the slow, rapid, buoyant, and wall contributions to the pressure–rate-of-strain tensor, the new model predicts pressure redistribution as the linear sum of two competing effects, an isotropization effect characteristic of the shear-dominated neutral surface layer and an anisotropization effect characteristic of the buoyancy-dominated convective one. We form an expression for the neutral contribution using surface-layer similarity (Obukhov 1946; Monin and Obukhov 1954) in the limit as $-z/L \to 0$, and an expression for the convective contribution using mixed-layer similarity (Willis and Deardorff 1974) in the limit as $-z/L \to \infty$. As a result of the scaling approach, the model is scale-similar, allowing for its coefficients to be obtained using the dynamic procedure.

A priori tests using high-resolution large-eddy simulations of the neutrally stratified and free convective ABL show that the model is capable of predicting both return to isotropy (for the former) and generation of anisotropy (for the latter). In cases where both shear and buoyancy are important, the model predicts a transition from return to isotropy to generation of anisotropy. Under conditions of poorly-resolved turbulence (i.e. for large grid aspect ratios), the means of the normal components of the SGS pressure–rate-of-strain are generally under-predicted due to the under-resolution of the surrogate SGS fields used to evaluate the model coefficients. Moreover, when the heights of these

fields are comparable to the Monin–Obukhov length scale, the model inherently under-predicts the neutral contribution and over-predicts the convective contribution since its coefficients are skewed toward the latter. The results for the conditional means of the modelled terms, a more optimal measure of model performance, are generally consistent with field measurements from the AHATS campaign. For the neutrally stratified and weakly convective surface layers, the model predicts weaker rates of pressure redistribution (from the streamwise to the spanwise and vertical velocity components) during downdrafts, consistent with return to isotropy and wall damping effects; while for the moderately and strongly convective surface layers, it predicts conditional energy redistribution from the vertical to the horizontal components during downdrafts, consistent with generation of anisotropy and wall blocking effects. The analyses suggest that the scaling-based similarity model may yield better predictions of the surface-layer anisotropy, especially under conditions of strong convective instability.

The results obtained in this research have important implications for SGS modelling. They show that the dynamics of the SGS stress and scalar flux depend strongly on the surface-layer stability and the LES filter scale, and can have characteristics significantly different from those of the Reynolds stress and flux. In conditions of under-resolved turbulence, first-order SGS models can fare poorly in their representation of the unresolved scales, understandably due to their lack of physical detail in favor of computational expediency (Lilly 1967). Though the seminal work of Deardorff (1973) successfully demonstrated the use of transport equation modelling to address the shortcomings of the Smagorinsky (1963) closure, computational constraints forced an eventual return to the eddy-diffusivity approach (Deardorff 1980). Today, tremendous strides in high performance computing mitigate partially the expense incurred in using the transport-equation approach (Wyngaard 2004) and in principle allow for the SGS fluxes to be described by their governing equations. The approach however presents new challenges for parameterizing the unclosed terms which evolve the model conservation equations. An understanding of the near-wall SGS dynamics which span across both atmospheric stability and filter scale, as revealed in the present study, is therefore crucial.

Appendices

Appendix A Derivation of the conditional mean SGS transport equations

The transport equation governing the evolution of the conditional mean is derived below using the delta-function technique (e.g., Pope 2000, 2010) for given quantity $\boldsymbol{Q}(\boldsymbol{x},t)$ and conditioning variables $\boldsymbol{C}(\boldsymbol{x},t)$. Denoting the JPDF of $\boldsymbol{C}(\boldsymbol{x},t)$ by

$$f_c(\boldsymbol{c};t) = \langle \delta(\boldsymbol{C}(\boldsymbol{x},t) - \boldsymbol{c}) \rangle, \tag{1}$$

the conditional mean of $\boldsymbol{Q}(\boldsymbol{x},t)$, $\langle \boldsymbol{Q} | \boldsymbol{C} = \boldsymbol{c} \rangle$, is given by

$$f_c(\boldsymbol{c};t) \langle \boldsymbol{Q}(\boldsymbol{x},t) | \boldsymbol{C}(\boldsymbol{x},t) = \boldsymbol{c} \rangle = \langle \boldsymbol{Q}(\boldsymbol{x},t) \delta(\boldsymbol{C}(\boldsymbol{x},t) - \boldsymbol{c}) \rangle, \tag{2}$$

where $\langle \boldsymbol{Q} | \boldsymbol{C} = \boldsymbol{c} \rangle$ denotes the mean value of $\boldsymbol{Q}$ given that $\boldsymbol{C}$ takes the value $\boldsymbol{c}$. Differentiating both sides of (2) with respect to x_i yields

$$\begin{aligned} f_c \frac{\partial \langle \boldsymbol{Q} | \boldsymbol{c} \rangle}{\partial x_i} + \frac{\partial f_c}{\partial x_i} \langle \boldsymbol{Q} | \boldsymbol{c} \rangle &= \left\langle \frac{\partial \boldsymbol{Q}}{\partial x_i} \delta(\boldsymbol{C} - \boldsymbol{c}) \right\rangle + \left\langle \boldsymbol{Q} \frac{\partial \delta(\boldsymbol{C} - \boldsymbol{c})}{\partial x_i} \right\rangle \\ &= f_c \left\langle \frac{\partial \boldsymbol{Q}}{\partial x_i} \middle| \boldsymbol{c} \right\rangle + \left\langle \boldsymbol{Q} \frac{\partial \delta(\boldsymbol{C} - \boldsymbol{c})}{\partial \boldsymbol{C}} \frac{\partial \boldsymbol{C}}{\partial x_i} \right\rangle \\ &= f_c \left\langle \frac{\partial \boldsymbol{Q}}{\partial x_i} \middle| \boldsymbol{c} \right\rangle - \frac{\partial}{\partial \boldsymbol{c}} \left\langle \boldsymbol{Q} \delta(\boldsymbol{C} - \boldsymbol{c}) \frac{\partial \boldsymbol{C}}{\partial x_i} \right\rangle, \end{aligned} \tag{3}$$

and therefore

$$\left\langle \frac{\partial \boldsymbol{Q}}{\partial x_i} \middle| \boldsymbol{c} \right\rangle = \frac{\partial \langle \boldsymbol{Q} | \boldsymbol{c} \rangle}{\partial x_i} + \frac{1}{f_c} \frac{\partial f_c}{\partial x_i} \langle \boldsymbol{Q} | \boldsymbol{c} \rangle + \frac{1}{f_c} \frac{\partial}{\partial \boldsymbol{c}} \left[\left\langle \boldsymbol{Q} \frac{\partial \boldsymbol{C}}{\partial x_i} \middle| \boldsymbol{c} \right\rangle f_c \right]. \tag{4}$$

For $\boldsymbol{Q} = 1$, (4) reduces to

$$\frac{\partial f_c}{\partial x_i} = -\frac{\partial}{\partial \boldsymbol{c}} \left[\left\langle \frac{\partial \boldsymbol{C}}{\partial x_i} \middle| \boldsymbol{c} \right\rangle f_c \right]. \tag{5}$$

From (4) and (5), we obtain

$$\begin{aligned} \left\langle \frac{\partial \boldsymbol{Q}}{\partial x_i} \middle| \boldsymbol{c} \right\rangle &= \frac{\partial \langle \boldsymbol{Q} | \boldsymbol{c} \rangle}{\partial x_i} - \frac{1}{f_c} \frac{\partial}{\partial \boldsymbol{c}} \left[\left\langle \frac{\partial \boldsymbol{C}}{\partial x_i} \middle| \boldsymbol{c} \right\rangle f_c \right] \langle \boldsymbol{Q} | \boldsymbol{c} \rangle + \frac{1}{f_c} \frac{\partial}{\partial \boldsymbol{c}} \left[\left\langle \boldsymbol{Q} \frac{\partial \boldsymbol{C}}{\partial x_i} \middle| \boldsymbol{c} \right\rangle f_c \right] \\ &= \frac{\partial \langle \boldsymbol{Q} | \boldsymbol{c} \rangle}{\partial x_i} + \left\langle \frac{\partial \boldsymbol{C}}{\partial x_i} \middle| \boldsymbol{c} \right\rangle \frac{\partial \langle \boldsymbol{Q} | \boldsymbol{c} \rangle}{\partial \boldsymbol{c}} + \frac{1}{f_c} \frac{\partial}{\partial \boldsymbol{c}} \left[\mathrm{cov} \left(\boldsymbol{Q}, \frac{\partial \boldsymbol{C}}{\partial x_i} \middle| \boldsymbol{c} \right) f_c \right], \end{aligned} \tag{6}$$

where

$$\mathrm{cov}\left(\boldsymbol{Q}\ ,\frac{\partial \boldsymbol{C}}{\partial x_i}\middle|\boldsymbol{c}\right)=\left\langle \boldsymbol{Q}\frac{\partial \boldsymbol{C}}{\partial x_i}\middle|\boldsymbol{c}\right\rangle-\langle \boldsymbol{Q}|\boldsymbol{c}\rangle\left\langle\frac{\partial \boldsymbol{C}}{\partial x_i}\middle|\boldsymbol{c}\right\rangle \tag{7}$$

is the conditional covariance between $\boldsymbol{Q}$ and $\partial \boldsymbol{C}/\partial x_i$.

Similarly, differentiating both sides of (2) with respect to t yields

$$f_c\frac{\partial\langle \boldsymbol{Q}|\boldsymbol{c}\rangle}{\partial t}+\frac{\partial f_c}{\partial t}\langle \boldsymbol{Q}|\boldsymbol{c}\rangle=f_c\left\langle\frac{\partial \boldsymbol{Q}}{\partial t}\middle|\boldsymbol{c}\right\rangle-\frac{\partial}{\partial \boldsymbol{c}}\left\langle \boldsymbol{Q}\delta(\boldsymbol{C}-\boldsymbol{c})\frac{\partial \boldsymbol{C}}{\partial t}\right\rangle \tag{8}$$

and, after manipulations similar to (4)-(6), we obtain

$$\frac{\partial\langle \boldsymbol{Q}|\boldsymbol{c}\rangle}{\partial t}=\left\langle\frac{\partial \boldsymbol{Q}}{\partial t}\middle|\boldsymbol{c}\right\rangle-\left\langle\frac{\partial \boldsymbol{C}}{\partial t}\middle|\boldsymbol{c}\right\rangle\frac{\partial\langle \boldsymbol{Q}|\boldsymbol{c}\rangle}{\partial \boldsymbol{c}}-\frac{1}{f_c}\frac{\partial}{\partial \boldsymbol{c}}\left[\mathrm{cov}\left(\boldsymbol{Q}\ ,\frac{\partial \boldsymbol{C}}{\partial t}\middle|\boldsymbol{c}\right)f_c\right]. \tag{9}$$

A.1 Transport equation for the conditional mean SGS stress

Using (9) with $\boldsymbol{Q}=\tau_{ij}$, $\boldsymbol{C}=\boldsymbol{u}^r$ (with the sample-space variable $\boldsymbol{c}=\boldsymbol{v}$), and $\partial\tau_{ij}/\partial t$ given by (e.g., Lilly 1967)

$$\frac{\partial\tau_{ij}}{\partial t}=-u_k^r\frac{\partial\tau_{ij}}{\partial x_k}+\frac{\partial}{\partial x_k}T_{ijk}^{(t)}+P_{ij}+P_{Bij}+\Pi_{ij}-\epsilon_{ij}, \tag{10}$$

we obtain

$$\begin{aligned}\frac{\partial\langle\tau_{ij}|\boldsymbol{u}^r\rangle}{\partial t}&=\left\langle\frac{\partial\tau_{ij}}{\partial t}\middle|\boldsymbol{u}^r\right\rangle-\left\langle\frac{\partial u_k^r}{\partial t}\middle|\boldsymbol{u}^r\right\rangle\frac{\partial\langle\tau_{ij}|\boldsymbol{u}^r\rangle}{\partial v_k}-\frac{1}{f_u}\frac{\partial}{\partial v_l}\left[\mathrm{cov}\left(\tau_{ij}\ ,\frac{\partial u_l^r}{\partial t}\middle|\boldsymbol{u}^r\right)f_u\right]\\&=\left\langle-u_k^r\frac{\partial\tau_{ij}}{\partial x_k}\middle|\boldsymbol{u}^r\right\rangle+\left\langle\frac{\partial}{\partial x_k}T_{ijk}^{(t)}+P_{ij}+P_{Bij}+\Pi_{ij}-\epsilon_{ij}\middle|\boldsymbol{u}^r\right\rangle\\&\quad-\left\langle\frac{\partial u_k^r}{\partial t}\middle|\boldsymbol{u}^r\right\rangle\frac{\partial\langle\tau_{ij}|\boldsymbol{u}^r\rangle}{\partial v_k}-\frac{1}{f_u}\frac{\partial}{\partial v_l}\left[\mathrm{cov}\left(\tau_{ij}\ ,\frac{\partial u_l^r}{\partial t}\middle|\boldsymbol{u}^r\right)f_u\right],\end{aligned} \tag{11}$$

where, for convenience, the sample-space variable in the conditional means has been omitted. Re-writing the conditional mean spatial derivative (first term on the right-hand side of (11)) using (6)

yields

$$\begin{aligned}\frac{\partial\langle\tau_{ij}|\boldsymbol{u}^r\rangle}{\partial t} = & -v_k\left\{\frac{\partial\langle\tau_{ij}|\boldsymbol{u}^r\rangle}{\partial x_k}+\left\langle\frac{\partial u_l^r}{\partial x_k}\middle|\boldsymbol{u}^r\right\rangle\frac{\partial\langle\tau_{ij}|\boldsymbol{u}^r\rangle}{\partial v_l}+\frac{1}{f_u}\frac{\partial}{\partial v_l}\left[\mathrm{cov}\left(\tau_{ij}\ ,\frac{\partial u_l^r}{\partial x_k}\middle|\boldsymbol{u}^r\right)f_u\right]\right\}\\ & +\left\langle\frac{\partial}{\partial x_k}T_{ijk}^{(t)}+P_{ij}+P_{Bij}+\Pi_{ij}-\epsilon_{ij}\middle|\boldsymbol{u}^r\right\rangle\\ & -\left\langle\frac{\partial u_k^r}{\partial t}\middle|\boldsymbol{u}^r\right\rangle\frac{\partial\langle\tau_{ij}|\boldsymbol{u}^r\rangle}{\partial v_k}-\frac{1}{f_u}\frac{\partial}{\partial v_l}\left[\mathrm{cov}\left(\tau_{ij}\ ,\frac{\partial u_l^r}{\partial t}\middle|\boldsymbol{u}^r\right)f_u\right].\end{aligned}\tag{12}$$

Here, u_k^r takes the value v_k and is taken out of the conditional mean. Re-arrangement of (12) yields the transport equation for $\langle\tau_{ij}|\boldsymbol{u}^r\rangle$,

$$\begin{aligned}\frac{\partial\langle\tau_{ij}|\boldsymbol{u}^r\rangle}{\partial t} = & -v_k\frac{\partial\langle\tau_{ij}|\boldsymbol{u}^r\rangle}{\partial x_k}-\left\langle\left(\frac{\partial u_l^r}{\partial t}+u_k^r\frac{\partial u_l^r}{\partial x_k}\right)\middle|\boldsymbol{u}^r\right\rangle\frac{\partial\langle\tau_{ij}|\boldsymbol{u}^r\rangle}{\partial v_l}\\ & +\left\langle\frac{\partial}{\partial x_k}T_{ijk}^{(t)}\middle|\boldsymbol{u}^r\right\rangle+\langle P_{ij}|\boldsymbol{u}^r\rangle+\langle P_{Bij}|\boldsymbol{u}^r\rangle+\langle\Pi_{ij}|\boldsymbol{u}^r\rangle-\langle\epsilon_{ij}|\boldsymbol{u}^r\rangle\\ & -\frac{1}{f_u}\frac{\partial}{\partial v_l}\left[\mathrm{cov}\left(\tau_{ij}\ ,\frac{\partial u_l^r}{\partial t}+u_k^r\frac{\partial u_l^r}{\partial x_k}\middle|\boldsymbol{u}^r\right)f_u\right].\end{aligned}\tag{13}$$

A.2 Transport equation for the conditional mean SGS temperature flux

Similarly, using (9) with $\boldsymbol{Q}=F_i$, $\boldsymbol{C}=\theta^r$ (with the sample-space variable $\boldsymbol{c}=\psi$), and $\partial F_i/\partial t$ given by

$$\frac{\partial F_i}{\partial t}=-u_k^r\frac{\partial F_i}{\partial x_k}+\frac{\partial}{\partial x_k}T_{Fik}^{(t)}+P_{Fi}+P_{BFi}+\Pi_{Fi},\tag{14}$$

we obtain

$$\begin{aligned}\frac{\partial\langle F_i|\theta^r\rangle}{\partial t} &= \left\langle\frac{\partial F_i}{\partial t}\middle|\theta^r\right\rangle-\left\langle\frac{\partial\theta^r}{\partial t}\middle|\theta^r\right\rangle\frac{\partial\langle F_i|\theta^r\rangle}{\partial\psi}-\frac{1}{f_\theta}\frac{\partial}{\partial\psi}\left[\mathrm{cov}\left(F_i\ ,\frac{\partial\theta^r}{\partial t}\middle|\theta^r\right)f_\theta\right]\\ &= \left\langle-u_k^r\frac{\partial F_i}{\partial x_k}\middle|\theta^r\right\rangle+\left\langle\frac{\partial}{\partial x_k}T_{Fik}^{(t)}+P_{Fi}+P_{BFi}+\Pi_{Fi}\middle|\theta^r\right\rangle\\ &\quad -\left\langle\frac{\partial\theta^r}{\partial t}\middle|\theta^r\right\rangle\frac{\partial\langle F_i|\theta^r\rangle}{\partial\psi}-\frac{1}{f_\theta}\frac{\partial}{\partial\psi}\left[\mathrm{cov}\left(F_i\ ,\frac{\partial\theta^r}{\partial t}\middle|\theta^r\right)f_\theta\right],\end{aligned}\tag{15}$$

where, again, the sample-space variable in the conditional means has been omitted for convenience. The first term on the right-hand side of (15) can be expressed as

$$\left\langle-u_k^r\frac{\partial F_i}{\partial x_k}\middle|\theta^r\right\rangle=-\langle u_k^r|\theta^r\rangle\left\langle\frac{\partial F_i}{\partial x_k}\middle|\theta^r\right\rangle-\mathrm{cov}\left(u_k^r\ ,\frac{\partial F_i}{\partial x_k}\middle|\theta^r\right).\tag{16}$$

Re-writing the conditional mean spatial derivative using (6) yields

$$\begin{aligned}\frac{\partial\langle F_i|\theta^r\rangle}{\partial t} =& -\langle u_k^r|\theta^r\rangle\left\{\frac{\partial\langle F_i|\theta^r\rangle}{\partial x_k}+\left\langle\frac{\partial\theta^r}{\partial x_k}\middle|\theta^r\right\rangle\frac{\partial\langle F_i|\theta^r\rangle}{\partial\psi}+\frac{1}{f_\theta}\frac{\partial}{\partial\psi}\left[\mathrm{cov}\left(F_i\ ,\frac{\partial\theta^r}{\partial x_k}\middle|\theta^r\right)f_\theta\right]\right\}\\ &-\mathrm{cov}\left(u_k^r\ ,\frac{\partial F_i}{\partial x_k}\middle|\theta^r\right)+\left\langle\frac{\partial}{\partial x_k}T_{Fik}^{(t)}+P_{Fi}+P_{BFi}+\Pi_{Fi}\middle|\theta^r\right\rangle\\ &-\left\langle\frac{\partial\theta^r}{\partial t}\middle|\theta^r\right\rangle\frac{\partial\langle F_i|\theta^r\rangle}{\partial\psi}-\frac{1}{f_\theta}\frac{\partial}{\partial\psi}\left[\mathrm{cov}\left(F_i\ ,\frac{\partial\theta^r}{\partial t}\middle|\theta^r\right)f_\theta\right].\end{aligned}\tag{17}$$

Re-arranging (17) yields the transport equation for $\langle F_i|\theta^r\rangle$,

$$\begin{aligned}\frac{\partial\langle F_i|\theta^r\rangle}{\partial t} =& -\left\{\langle u_k^r|\theta^r\rangle\frac{\partial\langle F_i|\theta^r\rangle}{\partial x_k}+\mathrm{cov}\left(u_k^r\ ,\frac{\partial F_i}{\partial x_k}\middle|\theta^r\right)\right\}\\ &-\left\langle\left(\frac{\partial\theta^r}{\partial t}+\langle u_k^r|\theta^r\rangle\frac{\partial\theta^r}{\partial x_k}\right)\middle|\theta^r\right\rangle\frac{\partial\langle F_i|\theta^r\rangle}{\partial\psi}\\ &+\left\langle\frac{\partial}{\partial x_k}T_{Fik}^{(t)}\middle|\theta^r\right\rangle+\langle P_{Fi}|\theta^r\rangle+\langle P_{BFi}|\theta^r\rangle+\langle\Pi_{Fi}|\theta^r\rangle\\ &-\frac{1}{f_\theta}\frac{\partial}{\partial\psi}\left[\mathrm{cov}\left(F_i\ ,\frac{\partial\theta^r}{\partial t}+\langle u_k^r|\theta^r\rangle\frac{\partial\theta^r}{\partial x_k}\middle|\theta^r\right)f_\theta\right].\end{aligned}\tag{18}$$

Bibliography

A. Andrén, A. R. Brown, J. Graf, P. J. Mason, C.-H. Moeng, F. T. M. Nieuwstadt, and U. Schumann. Large-eddy simulation of a neutrally stratified boundary layer: A comparison of four computer codes. *Q.J.R. Met. Soc.*, 120:1457–1484, 1994.

J. Bardina, J. H. Ferziger, and W. C. Reynolds. Improved subgrid-scale models for large-eddy simulation. *AIAA Paper 80-1357*, 1980.

R. J. Beare, M. K. MacVean, A. A. M. Holtslag, J. Cuxart, I. Esau, J.-C. Golaz, M. A. Jimenez, M. Khairoutdinov, B. Kosovic, D. Lewellen, T. S. Lund, J. K. Lundquist, A. McCabe, A. F. Moene, Y. Noh, S. Raasch, and P. P. Sullivan. An intercomparison of large-eddy simulations of the stable boundary layer. *Boundary-Layer Meteorol.*, 118:247–272, 2006.

V. Borue and S. Orszag. Local energy flux and subgrid-scale statistics in three-dimensional turbulence. *J. Fluid Mech.*, 366:1–31, 1998.

E. Bou-Zeid, C. Higgins, H. Huwald, C. Meneveau, and M. B. Parlange. Field study of the dynamics and modelling of subgrid-scale turbulence in a stable atmospheric surface layer over a glacier. *J. Fluid Mech.*, 665:480–515, 2010.

E. F. Bradley, R. A. Antonia, and A. J. Chambers. Turbulence Reynolds number and the turbulent kinetic energy balance in the atmospheric surface layer. *Boundary-Layer Meteorol.*, 21:183–197, 1981.

P. Bradshaw. Comments on "Horizontal velocity spectra in an unstable surface layer". *J. Atmos. Sci.*, 35:1768–1769, 1978.

J. A. Businger, J. C. Wyngaard, Y. Izumi, and E. F. Bradley. Flux-profile relationships in the atmospheric surface layer. *J. Atmos. Sci.*, 28:181–189, 1971.

C. Canuto, M. Y. Hussaini, A. Quarteroni, and T. A. Zang. *Spectral Methods in Fluid Dynamics*. Springer-Verlag, 1988.

S. J. Caughey and J. C. Wyngaard. The turbulence kinetic energy budget in convective conditions. *Q.J.R. Met. Soc.*, 105:231–239, 1979.

S. Cerutti, C. Meneveau, and O. M. Knio. Spectral and hyper eddy viscosity in high-Reynolds-number turbulence. *J. Fluid Mech.*, 421:307–338, 2000.

Q. Chen and C. Tong. Investigation of the subgrid-scale stress and its production rate in a convective atmospheric boundary layer using measurement data. *J. Fluid Mech.*, 547:65–104, 2006.

Q. Chen, H. Zhang, D. Wang, and C. Tong. Subgrid-scale stress and its production rate: Conditions for the resolvable-scale velocity probability density function. *J. Turbulence*, 4:027, 2003.

Q. Chen, M. Otte, P. P. Sullivan, and C. Tong. *A posteriori* subgrid-scale model tests based on the conditional means of subgrid-scale stress and its production rate. *J. Fluid Mech.*, 626:149–181, 2009.

Q. Chen, S. Liu, and C. Tong. Investigation of the subgrid-scale fluxes and their production rates in a convective atmospheric surface layer using measurement data. *J. Fluid Mech.*, 660:282–315, 2010.

P. Y. Chou. On velocity correlations and the solution of the equations of turbulent fluctuation. *Quart. Appl. Math.*, 3:38–54, 1945.

R. A. Clark, J. H. Ferziger, and W. C. Reynolds. Evaluation of subgrid-scale models using an accurately simulated turbulent flow. *J. Fluid Mech.*, 91:1–16, 1979.

J. W. Deardorff. A numerical study of three-dimensional turbulent channel flow at large Reynolds numbers. *J. Fluid Mech.*, 41:453–480, 1970.

J. W. Deardorff. Numerical investigation of neutral and unstable planetary boundary layers. *J. Atmos. Sci.*, 29:91–115, 1972.

J. W. Deardorff. The use of subgrid transport equations in a three-dimensional model of atmospheric turbulence. *J. Fluids Eng.*, 95:429–438, 1973.

J. W. Deardorff. Stratocumulus-capped mixed layers derived from a three-dimensional model. *Boundary-Layer Meteorol.*, 18:495–527, 1980.

J. A. Domaradzki, W. Liu, and M. E. Brachet. An analysis of subgrid-scale interactions in numerically simulated isotropic turbulence. *Phys. Fluids A*, 5:1747–1759, 1993.

B. Dubrulle, J.-P. Laval, P. P. Sullivan, and J. Werne. A new dynamical subgrid model for the planetary surface layer. Part i: The model and *A Priori Tests*. *J. Atmos. Sci.*, 59:861–876, 2002.

P. A. Durbin. Near-wall turbulence closure modeling without damping functions. *Theoret. Comput. Fluid Dynamics*, 3:1–13, 1991.

P. A. Durbin. A Reynolds stress model for near-wall turbulence. *J. Fluid Mech.*, 249:465–498, 1993.

J. A. Elliott. Microscale pressure fluctuations measured within the lower atmospheric boundary layer. *J. Fluid Mech.*, 53:351–383, 1972.

R. M. Enriquez. *Subgrid-scale turbulence modeling for improved large-eddy simulation of the atmospheric boundary layer*. PhD Dissertation, Stanford University, Department of Civil and Environmental Engineering, April 2013.

S. Fu, B. E. Launder, and D. P. Tselepidakis. Accommodating the effects of high strain rates in modeling the pressure-strain correlation. Technical report, Mechanical Engineering Department Report TFD/87/5, UMIST, 1987.

M. Germano. Turbulence: The filtering approach. *J. Fluid Mech.*, 238:325–336, 1992.

M. Germano, U. Piomelli, P. Moin, and W. H. Cabot. A dynamic subgrid-scale eddy viscosity model. *Phys. Fluids A*, 3:1760–1765, 1991.

M. M. Gibson and B. E. Launder. Ground effects on pressure fluctuations in the atmospheric boundary layer. *J. Fluid Mech.*, 86:491–511, 1978.

K. Hanjalić and S. Jakirlić. Second-moment turbulence closure modelling. In B. E. Launder and N. D. Sandham, editors, *Closure Strategies for Turbulent and Transitional Flows*, pages 47–101. Cambridge University Press, Cambridge, UK, 2002.

S. C. Hatlee and J. C. Wyngaard. Improved subfilter-scale models from the HATS field data. *J. Atmos. Sci.*, 64:1694–1705, 2007.

C. W. Higgins, M. B. Parlange, and C. Meneveau. The effect of filter dimension on the subgrid-scale stress, heat flux, and tensor alignments in the atmospheric surface layer. *J. Atmos. Ocean. Tech.*, 24, 2007.

C. W. Higgins, M. Froidevaux, V. Simeonov, N. Vercauteren, C. Barry, and M. B. Parlange. The effect of scale on the applicability of Taylor's frozen turbulence hypothesis in the atmospheric boundary layer. *Boundary-Layer Meteorol.*, 143:379–391, 2012.

U. Högström. Analysis of turbulence structure in the surface layer with a modified similarity formulation for near neutral conditions. *J. Atmos. Sci.*, 47:1949–1972, 1990.

T. W. Horst, J. Kleissl, D. H. Lenschow, C. Meneveau, C.-H. Moeng, M. B. Parlange, P. P. Sullivan, and J. C. Weil. HATS: Field observations to obtain spatially-filtered turbulence fields from transverse arrays of sonic anemometers in the atmosperic surface flux layer. *J. Atmos. Sci.*, 61: 1566–1581, 2004.

J. C. Kaimal and J. J. Finnigan. *Atmospheric Boundary Layer Flows.* Oxford University Press, 1994.

J. C. Kaimal, J. C. Wyngaard, Y. Izumi, and O. R. Coté. Spectral characteristic of surface-layer turbulence. *Q.J.R. Met. Soc.*, 98:563–589, 1972.

J. C. Kaimal, J. C. Wyngaard, D. A. Haugen, O. R. Coté, Y. Izumi, S. J. Caughey, and C. J. Readings. Turbulence structure in the convective boundary layer. *J. Atmos. Sci.*, 33:2152–2169, 1976.

S. Khanna. *Structure of the atmospheric boundary layer from large eddy simulation.* PhD dissertation, The Pennsylvania State University, Department of Mechanical Engineering, December 1995.

S. Khanna and J. G. Brasseur. Analysis of Monin-Obukhov similarity from large-eddy simulation. *J. Fluid Mech.*, 345:251–286, 1997.

S. Khanna and J. G. Brasseur. Three-dimensional buoyancy- and shear-induced local structure of the atmospheric boundary layer. *J. Atmos. Sci.*, 55:710–743, 1998.

J. Kleissl, C. Meneveau, and M. Parlange. On the magnitude and variability of subgrid-scale eddy-diffusion coefficients in the atmospheric surface layer. *J. Atmos. Sci.*, 60:2372–2388, 2003.

J. B. Klemp and D. R. Durran. An upper boundary-condition permitting internal gravity-wave radiation in numerical mesoscale models. *Mon. Wea. Rev.*, 111:430–444, 1983.

B. Kosović. Subgrid-scale modelling for the large-eddy simulation of high-Reynolds-number boundary layer. *J. Fluid Mech.*, 336:151–182, 1997.

L. Kristensen, J. Mann, S. P. Oncley, and J. C. Wyngaard. How close is close enough when measuring scalar fluxes with displaced sensors? *J. Atmos. Ocean. Tech.*, 14:814–821, 1997.

J. A. Langford and R. D. Moser. Optimal LES formulations for isotropic turbulence. *J. Fluid Mech.*, 398:321–346, 1999.

B. E. Launder. On the effects of a gravitational field on the turbulent transport of heat and momentum. *J. Fluid Mech.*, 67:569–581, 1975.

B. E. Launder and N. D. Sandham. *Closure Strategies for Turbulent and Transitional Flows*. Cambridge University Press, Cambridge, UK, 2002.

B. E. Launder, G. J. Reece, and W. Rodi. Progress in the development of a Reynolds-stress turbulence closure. *J. Fluid Mech.*, 68(3):537–566, 1975.

J.-P. Laval, B. Dubrulle, and S. Nazarenko. Nonlocality of interaction of scales in the dynamics of 2D incompressible fluids. *Phys. Rev. Lett.*, 83:4061–4064, 1999.

D. H. Lenschow and M. R. Raupach. The attenuation of fluctuations in scalar concentrations through sampling tubes. *J. Geophys. Res.*, 96:15259–15268, 1991.

D. H. Lenschow and P. L. Stephens. The role of thermals in the convective boundary layer. *Boundary-Layer Meteorol.*, 19:509–532, 1980.

D. H. Lenschow, J. Mann, and L. Kristensen. How long is long enough when measuring fluxes and other turbulence statistics? Technical Report NCAR/TN-389 + STR, 1993.

A. Leonard. Energy cascade in large-eddy simulations of turbulent fluid flows. *Adv. in Geophys.*, 18:237–248, 1974.

D. K. Lilly. The representation of small-scale turbulence in numerical simulation experiments. In H. H. Goldstine, editor, *Proc. IBM Scientific Computing Symp. on Environ. Sci.*, pages 195–210. 1967.

F. L. Ludwig, F. K. Chow, and R. L. Street. Effect of turbulence models and spatial resolution on resolved velocity structure and momentum fluxes in large-eddy simulations of neutral boundary layer flow. *J. Appl. Meteor. Climatol.*, 48:1161–1180, 2009.

J. L. Lumley. Interpretation of time spectra measured in high-intensity shear flows. *Phys. Fluids*, 6:1056–1062, 1965.

J. L. Lumley. Computational modeling of turbulent flows. *Adv. Appl. Mech.*, 18:123–176, 1978.

J. L. Lumley. Turbulence modeling. *J. Appl. Mech.*, 50:1097–1103, 1983.

P. J. Mason. Large-eddy simulation: A critical review of the technique. *Q.J.R. Met. Soc.*, 120:1–26, 1994.

P. J. Mason and D. J. Thomson. Stochastic backscatter in large-eddy simulations of boundary layers. *J. Fluid Mech.*, 242:51–78, 1992.

G. A. McBean and J. A. Elliott. The vertical transports of kinetic energy by turbulence and pressure in the boundary layer. *J. Atmos. Sci.*, 32:753–766, 1975.

C. Meneveau and J. Katz. Scale-invariance and turbulence models for large-eddy simulation. *Annu. Rev. Fluid Mech.*, 32:1–32, 2000.

C. Meneveau, T. S. Lund, and W. H. Cabot. A Lagrangian dynamic subgrid-scale model of turbulence. *J. Fluid Mech.*, 319:353–385, 1996.

O. Métais and M. Lesieur. Spectral large eddy simulation of isotropic and stably stratified turbulence. *J. Fluid Mech.*, 239:157–194, 1992.

D. O. Miller, C. Tong, and J. C. Wyngaard. The effects of probe-induced flow distortion on velocity covariances: Field observations. *Boundary-Layer Meteorol.*, 91:483–493, 1999.

C.-H. Moeng. A large-eddy simulation model for the study of planetary boundary-layer turbulence. *J. Atmos. Sci.*, 41:2052–62, 1984.

C.-H. Moeng and J. C. Wyngaard. Spectral analysis of large-eddy simulations of the convective boundary layer. *J. Atmos. Sci.*, 45:3573–3587, 1988.

A. S. Monin and A. M. Obukhov. Basic laws of turbulent mixing in the ground layer of the atmosphere. *Trans. Inst. Teoret. Geofiz. Akad. Nauk SSSR*, 151:163–187, 1954.

D. Naot, A. Shavit, and M. Wolfshtein. Interactions between components of the turbulent velocity correlation tensor due to pressure fluctuations. *Israel J. Tech.*, 8:259–269, 1970.

K. X. Nguyen and C. Tong. Investigation of subgrid-scale physics in the convective atmospheric surface layer using the budgets of the conditional mean subgrid-scale stress and temperature flux. *J. Fluid Mech.*, 772:295–329, 2015.

K. X. Nguyen, T. W. Horst, S. P. Oncley, and C. Tong. Measurements of the budgets of the subgrid-scale stress and temperature flux in a convective atmospheric surface layer. *J. Fluid Mech.*, 729: 388–422, 2013.

K. X. Nguyen, M. J. Otte, E. G. Patton, P. P. Sullivan, and C. Tong. Investigation of the pressure–strain-rate correlation using high-resolution LES of the atmospheric boundary layer. In *Proceedings of the* 67^{th} *Annual Meeting of the American Physical Society Division of Fluid Dynamics*, volume 59, San Francisco, CA, 2014.

F. T. M. Nieuwstadt and J. P. J. M. M. de Valk. A large eddy simulation of buoyant and non-buoyant plume dispersion in the atmospheric boundary layer. *Atmos. Environ.*, 21:2573–2587, 1987.

F. T. M. Nieuwstadt, P. J. Mason, C.-H. Moeng, and U. Schumann. Large-eddy simulation of the convective boundary layer: A comparison of four computer codes. In F. et al. Durst, editor, *Turbulent Shear Flows 8*, pages 343–367. Springer-Verlag, 1991.

R. T. Nishiyama and A. J. Bedard. A quad-disk static pressure probe for measurement in adverse atmospheres – With a comparative review of static pressure probe designs. *Rev. Sci. Instrum.*, 62:2193–2204, 1991.

A. M. Obukhov. Turbulence in the atmosphere with inhomogeneous temperature. *Trans. Inst. Teoret. Geofiz. Akad. Nauk SSSR*, 1:95–115, 1946.

A. V. Oppenheim and R. W. Schafer. *Discrete-Time Signal Processing*. Prentice-Hall, Englewood Cliffs, NJ, 1989.

M. J. Otte and J. C. Wyngaard. Stably stratified interfacial-layer turbulence from large-eddy simulation. *J. Atmos. Sci.*, 58:3424–3442, 2001.

E. G. Patton, T. W. Horst, P. P. Sullivan, D. H. Lenschow, S. P. Oncley, W. O. J. Brown, S. P. Burns, A. B. Guenther, A. Held, T. Karl, S. D. Mayor, L. V. Rizzo, S. M. Spuler, J. Sun, A. A. Turnipseed, E. J. Allwine, S. L. Edburg, B. K. Lamb, R. Avissar, R. J. Calhoun, J. Kleissl, W. J. Massman, K. T. Paw-U, and J. C. Weil. The canopy horizontal array turbulence study. *Bull. Amer. Meteor. Soc.*, 92:593–611, 2011.

L. J. Peltier, J. C. Wyngaard, S. Khanna, and J. Brasseur. Spectra in the unstable surface layer. *J. Atmos. Sci.*, 53:49–61, 1996.

B. Perot and P. Moin. Shear-free turbulent boundary layers. Part 1: Physical insights into near-wall turbulence. *J. Fluid Mech.*, 295:199–227, 1995.

U. Piomelli, P. Moin, and J. H. Ferziger. Model consistency in large eddy simulation of turbulent channel flows. *Phys. Fluid*, 31:1884–1891, 1988.

U. Piomelli, Y. Yu, and R. J. Adrian. Subgrid-scale energy transfer and near-wall turbulence structure. *Phys. Fluids*, 8:215–224, 1996.

S. B. Pope. *Turbulent Flows*. Cambridge University Press, Cambridge, UK, 2000.

S. B. Pope. Ten questions concerning the large-eddy simulation of turbulent flows. *New J. Phys.*, 6:1–24, 2004.

S. B. Pope. Self-conditioned fields for large-eddy simulations of turbulent flows. *J. Fluid Mech.*, 652: 139–169, 2010.

F. Porté-Agel, C. Meneveau, and M. Parlange. A scale-dependent dynamics model for large-eddy simulation: Application to a neutral atmospheric buoyancy layer. *J. Fluid Mech.*, 415:261–284, 2000a.

F. Porté-Agel, M. B. Parlange, C. Meneveau, W. E. Eichinger, and M. Pahlow. Subgrid-scale dissipation in the atmospheric surface layer: Effects of stability and filter dimension. *J. Atmos. Sci.*, 1:75–87, 2000b.

F. Porté-Agel, M. B. Parlange, C. Meneveau, and W. E. Eichinger. *A priori* field study of the subgrid-scale heat fluxes and dissipation in the atmospheric surface layer. *J. Atmos. Sci.*, 58: 2673–2698, 2001.

A. G. Rajagopalan and C. Tong. Experimental investigation of scalar-scalar-dissipation filtered joint density function and its transport equation. *Phys. Fluids*, 15:227–244, 2003.

S. Ramachandran. *Subgrid modeling using transport equations: Large-eddy simulation of the atmospheric boundary layer*. PhD Dissertation, The Pennsylvania State University, Department of Meteorology, August 2010.

S. Ramachandran and J. C. Wyngaard. Subfilter-scale modelling using transport equations: Large-eddy simulation of the moderately convective atmospheric boundary layer. *Boundary-Layer Meteorol.*, 139:1–35, 2011.

S. K. Robinson. Coherent motions in the turbulent boundary layer. *Annu. Rev. Fluid Mech.*, 23: 601–639, 1991.

J. C. Rotta. Statistische theorie nichthomogener turbulenz. *Z. Phys.*, 129:547–572, 1951.

U. Schumann. Subgrid scale model for finite difference simulations of turbulent flows in plane channels and annuli. *J. Comp. Physics*, 18:376–404, 1975.

T-H Shih and J. L. Lumley. Modeling of pressure correlation terms in Reynolds stress and scalar flux equations. Technical Report FDA 85-5, Cornell University, 1985.

J. Smagorinsky. General circulation experiments with the primitive equations: I. The basic equations. *Mon. Weather Rev.*, 91:99–164, 1963.

P. R. Spalart, R. D. Moser, and M. M. Rogers. Spectral methods for the Navier-Stokes equations with one infinite and 2 periodic directions. *J. Comp. Phys.*, 96:297–324, 1991.

C. G. Speziale, S. Sarkar, and T. B. Gatski. Modeling the pressure-strain correlation of turbulence: An invariant dynamical system approach. *J. Fluid Mech.*, 227:245–272, 1991.

C. J. Speziale. Analytical methods for the development of Reynolds-stress closures in turbulence. *Annu. Rev. Fluid Mech.*, 23:107–157, 1991.

P. P. Sullivan, J. C. McWilliams, and C.-H. Moeng. A subgrid-scale model for large-eddy simulation of planetary boundary-layer flows. *Boundary-Layer Meteorol.*, 71:247–276, 1994.

P. P. Sullivan, J. C. McWilliams, and C.-H. Moeng. A grid nesting method for large-eddy simulation of planetary boundary-layer flows. *Boundary-Layer Meteorol.*, 80:167–202, 1996.

P. P. Sullivan, T. W. Horst, D. H. Lenschow, C.-H. Moeng, and J. C. Weil. Structure of subfilter-scale fluxes in the atmospheric surface layer with application to large-eddy simulation modeling. *J. Fluid Mech.*, 482:101–139, 2003.

P. P. Sullivan, J. B. Edson, T. W. Horst, J. C. Wyngaard, and M. Kelly. Subfilter scale fluxes in the marine surface layer: Results from the ocean horizontal array turbulence study (OHATS). In *17th Symposium on Boundary Layers and Turbulence*. Amer. Meteor. Soc., San Diego, CA, 2006.

C. Tong. Measurements of conserved scalar filtered density function in a turbulent jet. *Phys. Fluids*, 13:2923–2937, 2001.

C. Tong, J. C. Wyngaard, S. Khanna, and J. G. Brasseur. Resolvable- and subgrid-scale measurement in the atmospheric surface layer. In *12th Symp. on Boundary Layers and Turbulence*, pages 221–222. Amer. Meteor. Soc., Vancouver, BC, Canada, 1997.

C. Tong, J. C. Wyngaard, S. Khanna, and J. G. Brasseur. Resolvable- and subgrid-scale measurement in the atmospheric surface layer: Technique and issues. *J. Atmos. Sci.*, 55:3114–3126, 1998.

C. Tong, J. C. Wyngaard, and J. G. Brasseur. Experimental study of subgrid-scale stress in the atmospheric surface layer. *J. Atmos. Sci.*, 56:2277–2292, 1999.

A. A. Townsend. *The Structure of Turbulent Shear Flows*. Cambridge University Press, New York, 1976.

B. Vreman, B. Geurts, and H. Kuerten. On the formulation of the dynamic mixed subgrid-scale model. *Phys. Fluids*, 6:4057–4059, 1994.

M. P. Wand and M. C. Jones. *Kernel Smoothing*. Chapman & Hall/CRC, 1995.

D. Wang and C. Tong. Conditionally filtered scalar dissipation, scalar diffusion, and velocity in a turbulent jet. *Phys. Fluids*, 14:2170–2185, 2002.

D. Wang, C. Tong, and S. B. Pope. Experimental study of velocity filtered joint density function and its transport equation. *Phys. Fluids*, 16:3599–3613, 2004.

J. M. Wilczak and A. J. Bedard. A new turbulence microbarometer and its evaluation using the budget of horizontal heat flux. *J. Atmos. Ocean. Tech.*, 21:1170–1181, 2004.

J. M. Wilczak and J. A. Businger. Large-scale eddies in the unstably stratified atmospheric surface layers. Part II: Turbulent pressure fluctuations and the budgets of heat flux, stress and turbulent kinetic energy. *J. Atmos. Sci.*, 41:3551–3567, 1984.

J. M. Wilczak and J. E. Tillman. The three-dimensional structure of convection in the atmospheric surface layer. *J. Atmos. Sci.*, 37:2424–2443, 1980.

J. M. Wilczak, S. P. Oncley, and S. A. Stage. Sonic anemometer tilt correction algorithms. *Boundary-Layer Meteorol.*, 99:127–150, 2001.

G. E. Willis and J. W. Deardorff. A laboratory model of the unstable planetary boundary layer. *J. Atmos. Sci.*, 31:1297–1307, 1974.

J. C. Wyngaard. Spatial resolution of a resistance wire temperature sensor. *Phys. Fluids*, 14: 2052–2054, 1971.

J. C. Wyngaard. The effects of probe-induced flow distortion on atmospheric turbulence measurements. *J. Appl. Meteor.*, 20:784–794, 1981.

J. C. Wyngaard. Atmosperic turbulence. *Annu. Rev. Fluid Mech.*, 24:205–233, 1992.

J. C. Wyngaard. Toward numerical modeling in the "terra incognita". *J. Atmos. Sci.*, 61:1861–1826, 2004.

J. C. Wyngaard. *Turbulence in the Atmosphere*. Cambridge University Press, New York, 2010.

J. C. Wyngaard and O. R. Coté. The budgets of turbulent kinetic energy and temperature variance in the atmospheric surface layer. *J. Atmos. Sci.*, 28:190–201, 1971.

J. C. Wyngaard, O. R. Coté, and Y. Izumi. Local free convection, similarity, and the budgets of shear stress and heat flux. *J. Atmos. Sci.*, 28:1171–1182, 1971.

J. C. Wyngaard, A. Siegel, and J. M. Wilczak. On the response of a turbulent-pressure probe and the measurement of pressure transport. *Boundary-Layer Meteorol.*, 69:379–396, 1994.

D. Yang, C. Meneveau, and L. Shen. Dynamic modelling of sea-surface roughness for large-eddy simulation of wind over ocean wavefield. *J. Fluid Mech.*, 726:62–99, 2013.